

Influence of turbulence on the internal conductivity and total electrical resistance of a carbon black suspension inside a Semi-Solid Flow Battery

Master Thesis

Daniel van Bemmelen

Influence of turbulence on the internal conductivity and total electrical resistance of a carbon black suspension inside a Semi-Solid Flow Battery

Master Thesis

by

Daniel van Bemmelen

to obtain the degree of Master of Science
at the Delft University of Technology,
to be defended publicly on Monday June 28, 2023 at 10:30 AM.

Student number: 4705203
Project duration: September 6, 2022 - May 31, 2023
Thesis committee: Dr.Ir. M. Rohde, TU Delft, supervisor
Dr.Ir. D. Lathouwers, TU Delft
Dr. E.M. Kelder TU Delft

An electronic version of this thesis is available at <http://repository.tudelft.nl/>.

Abstract

Semi-solid flow batteries (SSFB) have emerged as a promising electrical energy storage technology. The performance of a SSFB is influenced by the presence of conducting carbon black (CB) particles in its electrolyte. In particular, the pumping and electrical resistance of an SSFB are significantly affected by the CB suspension, as its conductivity and rheology depend on the flow profile. This thesis aims to quantify the effects of a turbulent flow profile on the conductivity and electrical resistance, given the rheological properties of the CB suspension. As a result, it seeks to enhance our understanding of the impact of turbulence on the electrical and pumping resistance of the electrolyte inside an SSFB. To this end a Filter Matrix Lattice Boltzmann Method (FM-LBM) is employed as fluid dynamics model to accurately simulate non-Newtonian turbulent channel flow. Additionally, a model for describing the electric potential within a variable conductor is implemented to determine the total electrical resistance.

The implementation of the FM-LBM on a GPU allowed for efficient simulation of non-Newtonian turbulent fluid flow. The FM-LBM demonstrates good results compared to analytical data and known Newtonian turbulent simulations. Using the power-law viscosity model to approximate the CB rheology, the flow and shear rate characteristics of turbulent non-Newtonian channel flow is simulated. Data was obtained for different turbulent regimes represented by a general wall shear stress Reynolds number Re_τ^G and different shear-thinning rheologies represented by power index n . The simulation results reinforced the credibility of the study by demonstrating a damped turbulent effect in line with previous pipe flow research on turbulent shear thinning flow.

Turbulent conductivity fields are obtained by utilizing the shear rate profile and a conductivity shear rate relation obtained from previous experimental research. For large constant channel heights the increase in Re_τ^G results in an increase in conductivity. Subsequently, by using the potential model to determine the resistance, a decrease in total resistance is found. However, a large increase in pumping power needed to reach the turbulent state, results in a drastic decrease of overall efficiency. This efficiency is defined by the proposed non-dimensional power number, which relates the electrical power over pumping power to Re_τ^G .

Additionally, the increase in conductivity for larger Re_τ is found to show different scaling in the laminar and turbulent regime. As a result, the laminar conductivity fields, showed higher conductivity and lower resistance than the transitional turbulent conductivity fields when a smaller channel height is considered. It can therefore be concluded, that the characteristic shape of the laminar conductivity profile is preferable to its turbulent counterpart.

Additional research is needed to determine the exact channel dimensions for which turbulence in the shear thinning CB suspension can be expected. Developing a coupled electrochemical-transport model is also recommended to get a more complete description of the effect of turbulence on the electrochemical performance of a SSFB.

Contents

Abstract	i
Nomenclature	iv
1 Introduction	1
1.1 Semi-Solid Flow Batteries	2
1.2 Previous Research on Carbon Black Suspensions	2
1.3 Previous Research on non-Newtonian Turbulence	4
1.4 Research Goal	5
1.4.1 Research Structure	5
1.4.2 Research Questions	5
1.4.3 Outline	6
2 Theory	7
2.1 Electrochemical Performance of a Semi-Solid Flow Battery	7
2.1.1 Operational Fundamentals of a Semi-Solid Flow Battery	7
2.1.2 SSFB Performance Metrics	8
2.1.3 Electronic and Ionic Resistance	9
2.1.4 Modeling Electrochemical Performance	10
2.1.5 Carbon Black Resistance	11
2.2 Fluid Dynamics Models	13
2.2.1 Navier-Stokes Equation	13
2.2.2 Kinetic Theory	14
2.3 Lattice Boltzmann Method	14
2.3.1 Discretization of the Boltzmann Equation	15
2.3.2 Chapman Enskog Expansion	15
2.3.3 Stream and Collision Step	16
2.4 Non-Newtonian Fluids	16
2.4.1 Different Classes of non-Newtonian Fluids	17
2.4.2 Power-law Viscosity Model	17
2.5 Turbulence	18
2.5.1 What is Turbulence	18
2.5.2 Direct Numerical Simulation	19
2.5.3 Turbulent Statistics	19
2.5.4 Reynolds Number	20
2.6 Parallel Programming on a Graphics Processing Unit	21
2.6.1 Parallel Programming	22
2.6.2 CPU vs GPU	22
2.6.3 GPU Hierarchies	23
3 Fluid Dynamics Model	25
3.1 Filter Matrix Lattice Boltzmann Method Implementation	25
3.2 Boundary Conditions	26
3.3 Initialisation	27
3.4 Turbulent Statistics Implementation	29
3.5 GPU Implementation	30
3.6 FM-LBM GPU Algorithm	31
4 Electric Potential Model	34
4.1 Finite Volume Discretization	34
4.2 Geometry and Boundary Conditions	35

4.3	Solution Method	36
4.4	Electric Field and Resistance	37
5	Validation and Turbulent Flow Results	38
5.1	Parallel Performance GPU	38
5.2	Laminar Flow	39
5.3	Turbulent Newtonian Flow	42
5.3.1	Low turbulent statistics results	42
5.3.2	Transitional and high turbulent flow simulations	44
5.3.3	Newtonian Turbulence Benchmark Conclusion	46
5.4	Turbulent non-Newtonian Simulations	47
5.4.1	Non-Newtonian Input Parameters	47
5.4.2	Non-Newtonian Turbulence Results	48
5.4.3	Damped Turbulent Effect	51
5.5	Turbulent shear profiles	52
6	Carbon Black Turbulent Conductivity and Resistance Results	55
6.1	Finite Volume Method Validation	55
6.2	Non-Dimensional Scaling Analysis	56
6.3	Turbulent Carbon Black Conductivity and Resistance in Newtonian limit	57
6.3.1	Newtonian Conversion to Physical Units	57
6.3.2	Newtonian Conductivity Results	59
6.3.3	Newtonian Resistance and Effective Conductivity Results	60
6.3.4	Newtonian Conductivity and Resistance Results Summary	61
6.4	Turbulent Carbon Black Conductivity and Resistance considering the Non-Newtonian Rheology	61
6.4.1	Non-Newtonian Conversion to Physical Units	62
6.4.2	Non-Newtonian Conductivity Results	63
6.4.3	Non-Newtonian Resistance and Effective Conductivity Results	63
6.4.4	Non-Newtonian Laminar vs Turbulence Resistance and Effective Conductivity Results	65
6.4.5	Non-Newtonian Conductivity and Resistance Results Summary	65
6.5	Discussion	66
6.5.1	Reliability and Generality of Results	66
6.5.2	Effects of turbulence on SSFB Design	67
7	Conclusion and Recommendation	69
7.1	Conclusion	69
7.2	Recommendations	70
	References	73

Nomenclature

Symbols

Symbol	Definition	Unit
A	electrode area	$[m^2]$
c	discrete lattice speed	
c_s	lattice speed of sound	
\mathcal{D}	computational domain	
E_{ik}, E_{ki}	filter matrices	
F	body force	$[N]$
f	distribution function	
g	acceleration	$[m s^{-2}]$
H	channel half height	$[m]$
I	total current	$[A]$
j	current density	$[A m^{-2}]$
K	consistency index	$[kg s^{n-2} m^{-1}]$
L	channel length	$[m]$
\mathcal{L}	Turbulent length scale	$[m]$
n	power-law index	
N_p	number of probes	
p	pressure	$[N m^{-2}]$
P	power	$[W]$
R	electrical resistance	$[\Omega]$
t	time	$[s]$
Δt	simulation time between probes	$[lt]$
U	characteristics velocity scale	$[m s^{-1}]$
u	velocity	$[m s^{-1}]$
u_τ	shear velocity	$[m s^{-1}]$
$\Delta V, V$	potential difference	$[V]$
W	channel width	$[m]$
w	lattice weight coefficient	
α	momentum space	
$\dot{\gamma}$	shear rate	$[s^{-1}]$
θ	non-dimensional scaling parameter	
κ	ion conductivity	$[A^2 s^3 kg^{-1} m^{-3}]$
μ	dynamic viscosity	$[kg m^{-1} s^{-1}]$
ν	kinematic viscosity	$[m^2 s^{-1}]$
ρ	density	$[kg m^{-3}]$
σ	local electron conductivity	$[A^2 s^3 kg^{-1} m^{-3}]$
σ_{eff}	effective electron conductivity	$[A^2 s^3 kg^{-1} m^{-3}]$
τ	shear stress	$[kg m^{-1} s^{-2}]$
Φ	electric potential	V
ϕ	ion potential	V
ψ	non-dimensional scaling parameter	

Abbreviations

Abbreviation	Definition
CB	Carbon Black
CFD	Computational Fluid Dynamics
DNS	Direct Numerical Simulation
FM-LBM	Filter Matrix Lattice Boltzmann Method
FV	Finite Volume
GPU	Graphics Processing Unit
MLUPS	Million Lattice Updates per Second
NN	non-Newtonian
RMS	Root Mean Square
SM	Streaming Multiprocessor
SSFB	Semi-Solid Flow Battery

Non-Dimensional Numbers

Abbreviation	Definition	Formula
B	bulk over dynamic viscosity	$B = \frac{\zeta}{\nu}$
Kn	molecular over physical length scale	$Kn = \frac{\lambda}{H}$
Re	inertial over viscous forces	$Re = \frac{UH}{\nu}$
Re_{τ}	wall shear stress Reynolds number	
Re^G	General Reynolds number for power-law viscosity	
$Re^{\text{Transitional}}$	Transitional Reynolds number defining the transition from laminar to turbulent flow	
Po	electric over pumping power	$Po = \frac{P_e}{P_p}$

1

Introduction

The utilization of renewable energy sources such as solar and wind has exhibited a consistent upward trend, driven by intensified efforts by governments and industries [26][25]. In particular, solar and wind energy production has experienced substantial growth, with a staggering thirty-fold increase in solar power between 2010 and 2019 [74]. To meet the net zero targets set out by the IPCC, an additional seven-fold increase in solar and wind energy production is required to supply the world with enough carbon neutral energy sources in 2030 [68].

However, this surge in intermittent penetration of renewable energy presents a challenge from an energy security point of view. As solar and wind power generation is dependent on weather and seasonal factors, there is a need for large-scale, carbon-free energy storage to effectively balance energy demand and the grid. The ideal energy storage system should be affordable, safe, and has a long cycle life, while also considering factors such as power and energy density, material availability, and recyclability. Several large-scale carbon-free energy storage technologies are currently available, including pumped hydro storage, compressed air energy storage, hydrogen storage, and various types of batteries. The selection of the most suitable storage method depends on factors such as the required capacity, power output, storage duration, and geography.

Among the range of available battery options, flow batteries offer significant advantages over presently utilized lithium-ion solutions for large-scale energy storage. In particular, ongoing advancements in redox flow batteries have shown improved life cycle performance, cost effectiveness, simplified recyclability and, notably, superior scalability compared to other battery technologies [46][65]. Consequently, redox flow batteries, specifically vanadium redox flow batteries, have received substantial attention in recent decades, with approximately 30 active installations worldwide [73].

However, the relatively high costs associated with vanadium redox flow batteries, attributed primarily to their low energy density and expensive materials, as well as the use of potentially toxic substances, have forced research into alternative materials for flow batteries [47]. One such alternative concept is the semi-solid flow battery. This particular battery utilizes a solid particle suspension, resulting in a higher energy density and the possibility of reduced storage costs. However, this concept is still in its early stages, and the impact of internal electrical resistance and mechanical friction within the fluid is not yet fully understood. Particularly, the potential effects of turbulence on the electrochemical performance of such a Semi-Solid Flow Battery remain unknown.

The objective of this research is to enhance our understanding of the influence of turbulence on the electrical and mechanical energy losses within a Semi-Solid Flow Battery. By investigating this aspect, we aim to gain insights that will contribute to the development and optimization of Semi-Solid Flow Battery technology.

This chapter will give an introduction to the design of the semi-solid flow battery (SSFB) and how it compares to other battery options in section 1.1. A short overview of recent studies on the carbon black suspension inside the SSFB as well as on the numerical simulation of turbulent non-Newtonian fluids will be discussed in Sections 1.2 and 1.3. The research questions and the thesis outline are discussed in section 1.4.

1.1. Semi-Solid Flow Batteries

Flow batteries (FB) share similarities with conventional batteries, such as those commonly found in smartphones, because they convert and store electrical energy into chemical energy and vice versa. In flow batteries, electrical energy is stored through a redox reaction. This reaction takes place in the electrolytes, which are divided by a membrane, effectively separating the two half-reactions. During discharge, one of the halves reactions release an electron which flows from the respective half cell through an external device to reach the other half cell. In the opposite half cell, the second half reaction accepts the electron. During this process, an ion passes through the membrane, completing the charge loop and enabling the flow battery to supply electrical energy to an external device.

The difference in FBs from conventional batteries is their ability to constantly supply new chemical half-reactions to the battery by pumping fresh liquid electrolytes through it. Consequently, chemical energy can be stored in tanks situated outside the electrochemical stack, which includes the membrane and current collectors. The capacity of the battery increases with the size of these tanks, whereas its power is determined by the characteristics of the electrochemical stack, such as the distance between the current collector and the membrane. This decoupling of power and capacity is a significant advantage of flow batteries over conventional batteries when considering large-scale energy storage [2]. The main advantages of FB compared to conventional batteries can be further summarized as follows [49]:

- **Cost-effectiveness:** Less battery components, such as membranes and current collectors, are needed for equal capacity, reducing the total cost of implementation.
- **Extended life span:** Flow batteries typically have a longer lifespan compared to lithium-ion batteries. Continuous flow of fresh electrolytes in flow batteries helps mitigate degradation issues, enabling them to withstand a high number of charge-discharge cycles without significant capacity loss.
- **Safety:** Flow batteries have inherent safety advantages over conventional lithium ion batteries. Because the reactants in flow batteries are stored in separate tanks, the risk of thermal runaway or catastrophic failure is significantly reduced.

However, the main downsides of an FB are its low energy and power density compared to conventional batteries [22]. Specifically, the low energy density of the electrolytes requires more fluid, and therefore a larger battery. The lower power density restricts the power output and, therefore, the charge and discharge rates of a single cell.

A Semi-Solid Flow Battery (SSFB) aims to improve these two shortcomings of a FB by replacing the active particle solution by an active particle suspension. Utilizing an electrolyte that incorporates solid particles dispersed within it improves both the energy and power density of an SSFB by alleviating the solubility limitations associated with using a solution-based electrolyte [22]. Consequently, a greater number of active particles can be dissolved within the same fluid volume, leading to an increased energy density. Additionally, the SSFB can exploit higher potential redox couples, such as lithium, which are insoluble in water. This characteristic further enhances the power density of the SSFB.

The downside of a SSFB is the enhanced viscosity associated with the use of suspended active particles in the electrolyte. To this end, the porous media used in a FB to increase the reaction rate over the full half cells is replaced by a suspension of carbon black (CB) particles to conduct the electrons [22]. The addition of this CB suspension further changes the rheological properties of the fluid, affecting the pumping power needed during operation. The operation performance also depends significantly on the ability of the CB suspension to conduct electrical current [86]. The main focus of this research will be on the way the rheological and conductivity characteristics of the CB suspension affect the performance of an SSFB.

1.2. Previous Research on Carbon Black Suspensions

In order to facilitate reactions across the entire half-cells of an SSFB, carbon black particles are introduced into the electrolyte to create an electron-conducting suspension. CB particles have the ability to conduct electrons by aggregating into clusters. When the concentration of CB particles exceeds the so called percolation threshold, these clusters form a network that spans the entire half cell, leading to a significant enhancement in electronic conductivity [85][86].

The rheological and conductivity characteristics, such as the percolation threshold, maximum viscosity, and electron conductivity, are found to differ between the choices of the CB particle, the con-

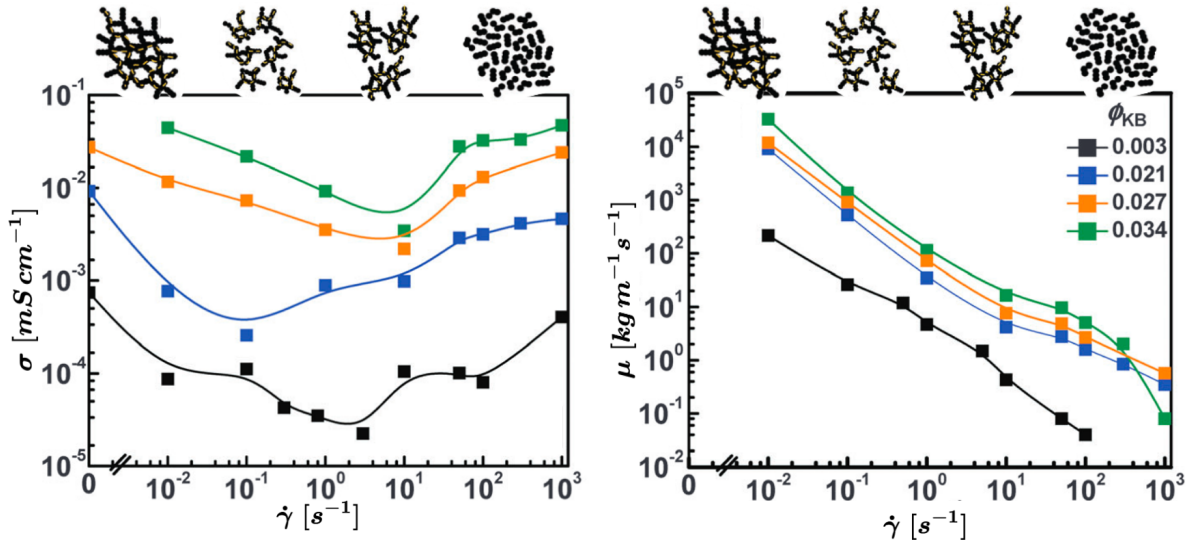


Figure 1.1: Figures show the experimentally obtained conductivity (σ) and viscosity (μ) correlations to shear rate ($\dot{\gamma}$) of a non-aqueous CB suspension [86]. The variation in conductivity and viscosity is a result of the shear rate causing the breakdown of CB clusters, as schematically depicted above both plots.

centration of CB and the type of liquid in which the CB particles are suspended. What all CB suspensions have in common is a strong shear dependence of the rheological and conductivity characteristics [85][86][56]. This can be explained by fluid shear breaking up the CB aggregates, which changes the viscosity and conductivity.

For both CB suspensions it was found that this breaking down of the CB clusters results in a thixotropic rheological property. This means that the fluid becomes thinner when shear is applied over a period of time [56]. For the non-aqueous CB suspension, a time-independent shear thinning viscosity characteristic was also experimentally defined, linking shear rate $\dot{\gamma}$ to viscosity μ as can be seen in Figure 1.1. The same study also experimentally obtained the relation between conductivity σ and $\dot{\gamma}$, as shown in figure 1.1. Both figures also represent the dispersion of the CB clusters due to shear rate that gives rise to the varying viscosity and conductivity.

The fact that both viscosity and conductivity depend on the shear rate results in these properties being dependent on the flow profile of the electrolyte in a SSFB. As a result, this has sparked research interest in investigating the impact of various flow profiles on the electrical resistance of the CB suspension and the pumping power required to push the electrolyte through the SSFB. The important findings can be summaries as follows:

- For aqueous CB suspensions, the effects of a laminar flow profile on CB resistance were experimentally studied [63]. Depending on the type of CB particle, the conductivity increased or decreased with an increase in flow rate.
- For non-aqueous CB suspensions the experimentally obtained shear rate relations found by Youssry *et al.* [86] where used to study the effects of different laminar flow profiles on CB resistance and pumping power numerically [64]. The conductivity was found to be several orders of magnitude lower than that of the aqueous CB suspension. This was mainly attributed to the low overall conductivity of non-aqueous CB. However, the discrepancy was enlarged by low conductivity bands in the middle of the channel which result from the laminar flow profile.

Both the above mentioned studies did not consider a turbulent flow profile. A turbulent flow, due to its drastically different shear rate profile, is assumed to change the conductivity characteristics of a CB suspension significantly. Therefore, the main focus of this research will be to study this effect. The next section will discuss the simulating of such non-Newtonian turbulent flow profiles.

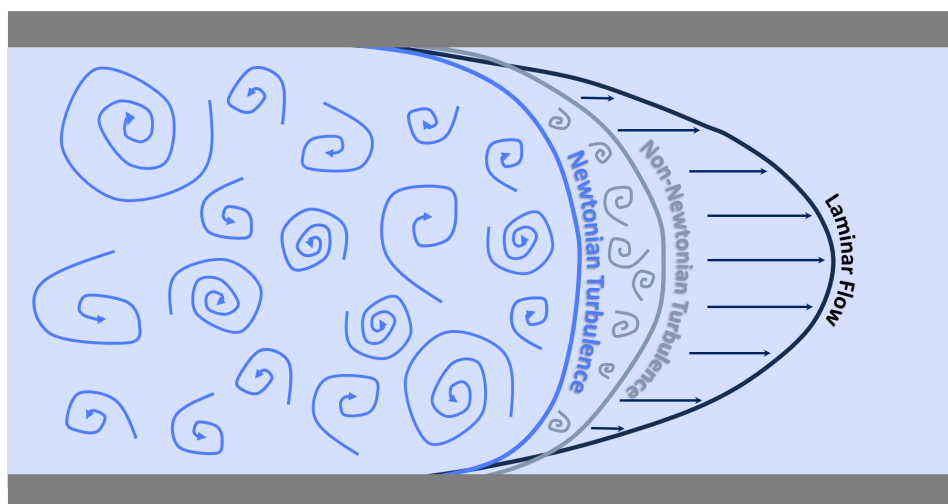


Figure 1.2: The figure illustrates a schematic representation of different flow regimes within a channel, including laminar flow, non-Newtonian turbulent flow, and Newtonian turbulent flow.

1.3. Previous Research on non-Newtonian Turbulence

When a flow profile transitions from the orderly laminar state to the disordered turbulent state the flow and subsequent shear rate profile changes drastically. Furthermore, modifying the rheological characteristics directly affects the turbulent flow profile, as is schematically depicted in Figure 1.2. The changes in flow profile consequently modify the shear rate profile, resulting in a corresponding change in the conductivity of the CB suspension within a SSFB.

Non-Newtonian turbulence is of significant interest in various industrial applications, aside from in SSFB. In recent decades, there has been a growing focus on simulating these non-Newtonian turbulent flows, driven by the increased computational power necessary for numerical analysis of turbulence. This section provides a concise overview of the latest advancements in the field of non-Newtonian turbulence simulation. Additionally, it highlights the developments related to the utilization of the Lattice Boltzmann Method, which is the chosen numerical method for this research.

Research on Numerical Simulation of Turbulent non-Newtonian Flow

Most of the numerical work done on non-Newtonian turbulence modeling has used the Direct Numerical Simulation method. Using either the Finite Volume Method [87][30] or the Spectral Element Method [70][71] the turbulent flow profile was simulated using the power-law viscosity model to implement the shear-thinning rheological characteristics. The most important findings can be summarised as follows

- The shear-thinning rheology makes the turbulence weaker as compared to Newtonian flow.
- The increased apparent viscosity away from the wall leads to the damping of the wall-normal velocity fluctuations, therefore decreasing the wall normal turbulent energy transfer. This effect also results in a stronger anisotropy of the turbulent structures.
- Shear-thinning turbulence also exhibits drag reduction when compared to Newtonian turbulence resulting in lower wall friction and higher fluid velocity.

All the above mentioned studies were conducted using a pipe geometry ¹. Given the squared geometry of most SSFB designs this research will aim to improve the understanding of non-Newtonian flow in a parallel plate geometry. Also the shear-rate profiles, needed to determine the effects of turbulence on the CB conductivity remain unreported requiring further research.

Research on the Lattice Boltzmann Method

The Lattice Boltzmann Method (LBM) is a novel numerical simulation technique that employs Kinetic Theory to solve macroscopic fluid properties, such as turbulent flow profiles. Rather than directly solving

¹As of the finalisation of this thesis a paper was published that studies the non-Newtonian flow characteristics in a closed channel [36].

the governing equations, the LBM simulates fluid density on a lattice using streaming and collision processes. This method enhances parallel capabilities and facilitates ease of implementation. Hence, the LBM will be employed as the numerical simulation technique in this research. To accelerate the numerical simulation process, the parallel capabilities of the LBM will be harnessed by implementing it on a Graphics Processing Unit (GPU).

The relevant research on (GPU) implementations of the LBM used for turbulent simulations can be summed up as follows:

- GPU Implementations using the Bhatnagar-Gross-Krook (BGK)-LBM have shown a rapid growth in simulation speed [21]. Using this method, turbulence has been simulated in a channel flow geometry within the time span of hours [28]. However, the BGK-LBM has shown limited numerical stability, especially for low viscosity [89]
- To improve the numerical stability the Filter-Matrix (FM)-LBM was introduced [75]. This method has also shown success in the simulation of Newtonian turbulent channel flows [88][69].
- Previous research on non-Newtonian laminar flow has shown good stability of the FM-LBM [64].

This research will aim to combine the separate knowledge on the FM-LBM for simulating turbulence, the utilization of a GPU for fast numerical processing and the implementation of non-Newtonian fluid rheology in the FM-LBM. By combining these areas of knowledge, a model will be developed with the capability to simulate turbulent non-Newtonian flow.

1.4. Research Goal

This research aims to better understand the non-Newtonian turbulent characteristics of a carbon black suspension and through that the effects of turbulence on the internal electrical conductivity and total resistance of a Semi-Solid Flow Battery. This section will provide an overview of the research structure and research questions that constitute the foundation of this study.

1.4.1. Research Structure

The research can be structured in the following steps.

1. Implementation of the FM-LBM on a GPU to effectively simulate turbulent non-Newtonian channel flow
2. Characterization and analysis of the shear rate profile arising from the turbulent flow profile within the channel.
3. Extraction of the CB conductivity profile from the turbulent shear rate profile.
4. Calculate the potential field inside the CB conductivity profile to determine the total CB resistance.
5. Derive scaling laws for the effects of turbulence on the electrical CB conductivity and resistance as well as the pumping power needed for operation.

1.4.2. Research Questions

The goals of this research can be expressed in the following research questions.

- How can existing LBM techniques be implemented on a GPU to simulate turbulent non-Newtonian channel flow that resembles carbon black rheology characteristics in a reasonable time frame?
 - What are the numerical design choices needed to simulate non-Newtonian turbulence using the Direct Numerical Simulation method?
 - How much can the GPU implementation enhance computational efficiency without compromising on accurate results?
- What is the Reynolds number effect of shear thinning non-Newtonian viscosity on the turbulent characteristics and specifically the shear rate profile inside a channel?
 - What are the effects of the shear thinning rheology on the turbulent statistics and shear rate profile?
 - How do the non-Newtonian turbulent statistics and shear rate profiles change for different Reynolds number turbulence regimes?

- What is the effect of turbulence on the internal conductivity and subsequent electrical resistance of a carbon black suspension as well as the pumping power needed to pump the suspension through the SSFB?
 - How does the shear thinning rheology influence the electrical conductivity and Resistance of a CB suspension in different Reynolds number turbulence regimes?
 - What are the characteristic differences in conductivity and Resistance between laminar and turbulent CB suspension flow fields?
 - How do the resistance and pumping power scale with respect to different laminar and turbulent flow regimes.

1.4.3. Outline

The structure of this thesis can be outlined as follows: Chapter 2 provides a theoretical background on electrochemical modeling, non-Newtonian turbulence simulation, and GPU programming. Chapter 3 describes the numerical implementation of the FM-LBM for simulating turbulent non-Newtonian flow. Chapter 4 explains the implementation of the electrical potential model for calculating electrical resistance. The results are presented in two chapters. Chapter 5 discusses the fluid flow results with a focus on numerical benchmarking, non-Newtonian flow simulation and the resulting shear-rate profiles. Chapter 6 explores the results of CB conductivity derived from turbulent shear rate profiles and subsequent electrical resistance characteristics. Lastly, Chapter 7 presents the conclusions and recommendations for further research.

2

Theory

The research question exploring the impact of turbulence on the electrical resistance of a CB suspension within a SSFB through numerical simulation, spans across multiple fields of physics. Specifically, this research is built upon three distinct theoretical fields: electrochemical modeling, fluid modeling, and high-performance computing. This chapter will lay out the relevant theories within these fields such to obtain the knowledge behind the modeling of the turbulent non-Newtonian fluid flow and the electrical potential field inside the SSFB.

Firstly, Section 2.1 will delve into the comprehensive explanation of the theory behind electrochemical performance modeling. Subsequently, the focus will shift towards the theories concerning fluid flow simulation. In particular, Sections 2.2 and 2.3 will provide an overview of fluid modeling and the lattice Boltzmann method (LBM) respectively. Following that, Sections 2.4 and 2.5 will delve into the theories underlying non-Newtonian fluids and turbulence respectively. Finally, the chapter will conclude with an overview of the relevant concepts within the field of high-performance computing and programming on a GPU.

2.1. Electrochemical Performance of a Semi-Solid Flow Battery

This chapter will discuss the relevant theory behind the modeling of the electrochemical performance of a SSFB. Specifically the effects of the internal conductivity of the CB suspension on the total electrical performance will be considered.

First, the operational fundamentals of a SSFB are further explained in Section 2.1.1. Subsequently the performance metrics important to SSFB design are discussed in section 2.1.2. Then, Section 2.1.3 will consider the different forms of internal resistance associated with a SSFB. The theory and methods behind the electrochemical modeling will be discussed in Section 2.1.4. Finally, the theory behind the quantification of the total electrical resistance of the CB suspension will be discussed in section 2.1.5.

2.1.1. Operational Fundamentals of a Semi-Solid Flow Battery

A Flow Battery (FB) and the more specific Semi-Solid Flow Battery both are Galvanic cells which produce electrical energy via electrochemical reactions. Figure 2.1 depicts such a (Semi-Solid) Flow Battery. In this section the working principals and differences behind both energy storing devices is discussed.

A Flow Battery (FB) is a type of battery that uses liquid active electrochemical energy carriers that are stored outside the battery. These energy carriers are two parts of a redox couple where the reducer (Red) and oxidant (Ox) together with the electrolyte make up the anodic and cathodic material respectively. In a flow battery these materials are separately pumped through an ion-exchange/electron extraction power stack. In this cell the anode and cathode fluids are separated by a membrane. This membrane is a electrical insulator while being permeable for ions. When the cell is connected to an external circuit the oxidation and reduction reactions take place in the anode and cathode respectively. The electron is transported via the electrode of the anode through an external circuit to the electrode of the cathode. To avoid positive and negative charge accumulation in the anode and cathode respectively, the membrane acts as a salt bridge transferring positive cations (Ca^+) and negative anions (An^-)

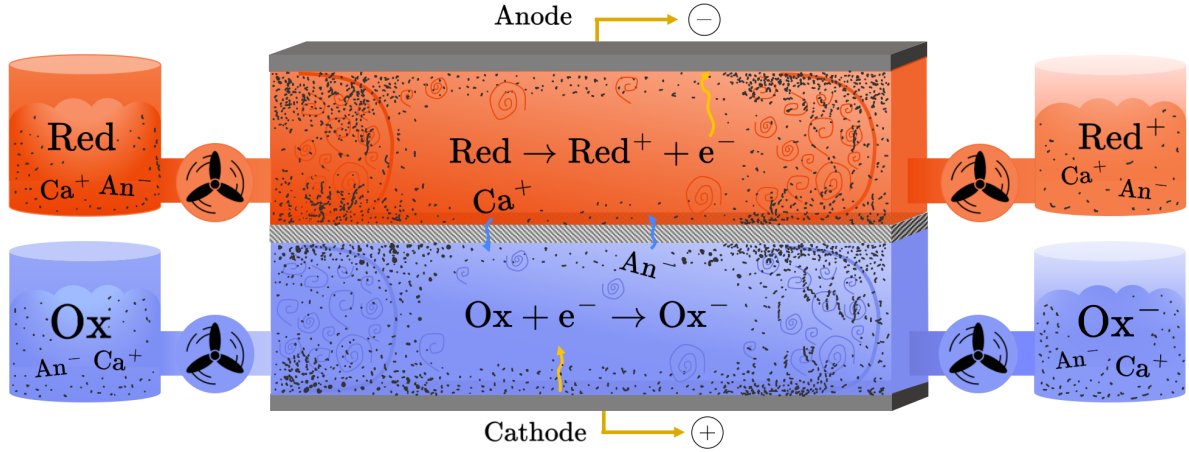


Figure 2.1: Schematic illustration of a (Semi-Solid) Flow Battery. The anodic and cathodic liquids are pumped through the battery where the redox half reactions take place and electrical energy is produced.

from one side to the other. This closes the charge loop and makes it possible for the FB to generate electrical power as long as new active anodic and cathodic material is pumped into the system.

The Semi-Solid Flow Batterie (SSFB) is an improvement of the above mentioned FB concept first proposed by Duduta *et al.* [22]. It differs from the FB concept in two ways:

- Firstly, in a SSFB the active reducer and oxidant are solid particles suspended in a liquid electrolyte. This in contrast to a FB where the active materials are dissolved in the electrolyte. The reason for this change is the increase in energy density of the total electrochemical fluid [22]. This increase in energy density has two reasons. The first one is the freedom to use redox couples that have a higher energy density but can not be dissolved in an electrolyte. The second reason is the liberation of the solubility constraint of the active materials making it possible to increase the amount of active material with respect to the electrolyte.
- The second change the SSFB design makes with respect to the the FB, has to do with the electrical conductance of the electrode fluid. The FB makes use of a porous medium to increase the conductivity and with that the reaction rate over the full flow channels/electrodes. Due to the increased viscosity of the SSFB electrolyte solutions, the use of such a porous medium requires much more pumping power. Therefore, in a SSFB a liquid electrical conducting medium is added to the electrolyte. Different kinds of Carbon Black (CB) suspensions are used to generate this conducting medium [22][86].

2.1.2. SSFB Performance Metrics

As mentioned, the SSFB has at its main advantage the decoupling of battery power and capacity. To achieve this it does however come with a possible decrease in energy efficiency due to the introduction of a mechanical pump requiring energy. The main SSFB performance metrics, considered in this research, are therefore:

- Battery capacity is defined as the amount of electric charge that a battery can store and deliver, typically measured in ampere-hours [Ah]. In a SSFB this is the amount of active electrolyte material that is capable of participating in the redox reaction.
- Battery energy efficiency, describes the percentage of electrical energy [J] put into storage that is later retrieved. In a SSFB the loss of efficiency is made up of mechanical losses due to pumping as well as the internal energy losses associated with the electrochemical process.
- Battery power, represents the rate at which electrical energy is generated or consumed by a battery system. In a SSFB the battery power is determined by the rate of the electrochemical reactions as well as the potential losses due to internal resistance.

The current density j [A/m^2] and cell voltage E_{cell} lie at the base of the performance metrics defined above. The cell voltage is defined as

$$E_{cell} = E_{cell}^{eq} - \Delta E_{reactions} - \Delta E_{electric} - \Delta E_{ionic} \quad (2.1)$$

with E_{cell}^{eq} the equilibrium potential of the redox couple without any current induced losses. The losses that follow from the current flowing are: $\Delta E_{reactions}$ the voltage losses due to chemical reactions, $\Delta E_{electric}$ the Ohmic losses due to electron resistivity and ΔE_{ionic} the losses due to ion resistivity.

Reducing these losses subsequently improves the performance metrics such as battery power. The effects of turbulence on the conductivity of the CB suspension will have a direct influence on the electrical Ohmic losses $\Delta E_{electric}$ and therefore on the performance metrics of a SSFB.

2.1.3. Electronic and Ionic Resistance

This section will discuss the internal electric and ionic Ohmic losses due to the electric and ionic resistance.

Electronic Resistance

During the charge and discharge cycles an electronic current flows from the reduction half reaction to the oxidation half reaction. During this path the electronic current experiences resistance resulting in the Ohmic potential. In a SSFB this potential drop can be broken down in three parts namely the charge transfer resistance, carbon black resistance and external circuit resistance. The internal resistance is only made up of the first two.

The resistance linked to the electron transfer between the cation and the carbon black network is known as the charge transfer resistance. Whilst important for overall SSFB performance, there is no available research on how this resistance changes for flow profile characteristics [53]. Modeling this resistance will therefore lie outside of the scope of this research.

The carbon black (CB) resistance is the resistance the electrical current experiences when flowing through the carbon black network. The CB conductivity is the reciprocal of electrical resistivity, and is defined by σ and has units of $[mS/cm]$. Using Ohm's law, σ quantifies the local electric current density j induced by the electric field via

$$j = \sigma E \quad (2.2)$$

where the electric field is defined as

$$E = -\nabla\Phi \quad (2.3)$$

with Φ being the electric potential inside the CB.

A conductive CB network is obtained when the CB suspension reaches a certain critical concentration. This concentration is called the percolation concentration and describes the moment for which the CB suspension forms a electrical conducting network with $\sigma > 0$, that spans the full cell. As discussed in section 1.2, this CB conductivity depends on a wide range of factors like the CB concentration, the sort of CB particles used and the composition of the surrounding medium. This research will focus on the non-aqueous Ketjen black EC-300 CB suspension with a volume fraction of $\phi_{CB} = 0.021$. This choice is made due to the optimal conductivity verses viscosity characteristics [64].

Figure 2.2 shows the CB conductivity dependence on shear rate for the CB concentrations chosen in this study. The fit to this measurement data obtained by Youssry *et al.* [86] can be expressed as a fourth order polynomial described by equation (2.4)

$$\sigma(\dot{\gamma}) = exp(p_0\dot{\gamma}^3 + p_1\dot{\gamma}^2 + p_2\dot{\gamma} + p_3) \quad (2.4)$$

with coefficients $p_0 = -8.07e - 3$, $p_1 = 5.22e - 2$, $p_2 = 0.334$ and $p_3 = -7.55$ [64]. Since it is hard to predict what happens outside the given curve the conductivity is assumed to remain constant for $\dot{\gamma} \leq 1e - 3 [s^{-1}]$ and $\dot{\gamma} \geq 634 s^{-1} [s^{-1}]$.

Due to the turbulent flow fields considered in this study, the shear rate field $\dot{\gamma}(x, t)$ will fluctuate over space and time. In turn this will lead to an internal conductivity field $\sigma(x, t)$. What the turbulent characteristics are of this conductivity field and what effect this will have on the total Ohmic losses will be the focus of this research.

Ionic Resistance

In order to maintain a balance of charge during the charge and discharge cycles of a flow battery, ions need to transfer from one cell to the other. The ionic resistance resulting in the ionic Ohmic drop ΔE_{ionic} can be contributed to the electrolyte and the ion exchange membrane ion resistance. The ease at which ion's transfer through this media is expressed by a electrolytic conductivity κ which, just as

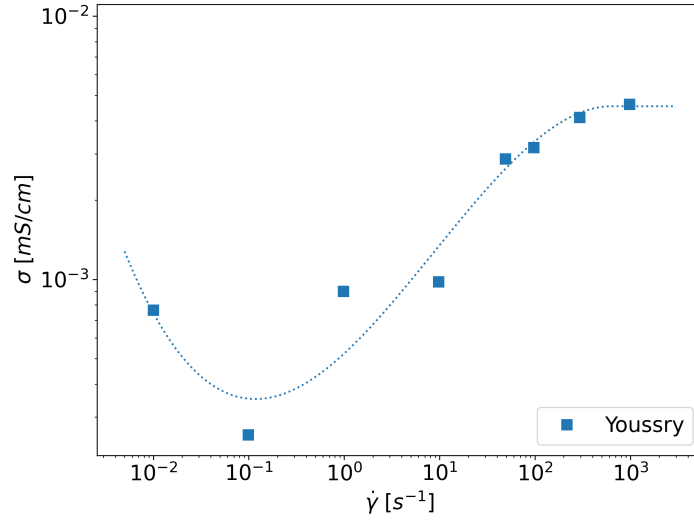


Figure 2.2: Non-aqueous CB suspension conductivity dependence on shear rate for different CB concentrations [86]

with the electric conductivity, relates the ionic current i to the ionic potential gradient $\nabla\phi$ via Ohm's law. Depending on the type of aqueous and non-aqueous electrolytes the κ for the membrane and electrolyte differ significantly. As an example, for the non-aqueous electrolyte, the ion conductivity inside the electrolytes itself ranges from 5 to 10 [mS/cm] corresponding to several order of magnitude higher κ than σ [84].

The ionic conductivity is multiple orders of magnitude higher than the electronic conductivity. The electron conductivity will therefore be a limiting factor and quantifying $\Delta E_{electric}$ will therefore be the key to finding the electrochemical performance of a SSFB. This will be the focus for the rest of this research where equation (2.4) will be used to describe the effect of turbulence and subsequent shear rate $\dot{\gamma}$ on the electrical conductivity and subsequent Ohmic losses.

2.1.4. Modeling Electrochemical Performance

To determine the variable electrical Ohmic losses exactly, the path of the electron needs to be known. Therefore the location of the reaction needs to be determined. To this end the electrochemical kinetics inside a SSFB need to be modeled.

Electrochemical Kinetics

Modeling the current-voltage relation in a SSFB starts with Faraday's law of electrolysis

$$\frac{\partial \rho_c}{\partial t} = n_e F a_R j_{\perp} \quad (2.5)$$

linking the redox reaction rate per unit area j_{\perp} [mol m⁻² s⁻¹] to the change in local current density ρ_c [C m⁻³]. This is done via the number of electrons per reaction n_e the active specific surface area a_R [m⁻¹] and Faraday's constant F [C mol⁻¹] [83]. In a SSFB the a_R is determined by the physical properties of the CB suspension chosen.

The reaction rate per unit area j_{\perp} depends on the following factors:

- Oxidant and Reductant (Ox/Red) activation potential E_{Ox}^a/E_{Red}^a
- Oxidant and reductant reactant concentrations C_{Ox}/C_{Red}
- Temperature T
- Effect of activation overpotential

$$\eta = (\Phi - \phi) - (\Phi^{eq} - \phi^{eq}) \quad (2.6)$$

where Φ^{eq} and ϕ^{eq} represent the electronic and ionic equilibrium potentials.

When the reaction kinetics are assumed to be of first order and there is assumed to be one (dominant) electron transfer involved, the Butler Volmer (BV) equation describes j_{\perp} . This equation is expressed as

$$j_{\perp} = \frac{j^*}{F} \left(\frac{C_{\text{Red}}}{C_{\text{Red}}^{eq}} e^{\frac{\alpha_{\text{Ox}} F \eta}{R_G T}} - \frac{C_{\text{Ox}}}{C_{\text{Ox}}^{eq}} e^{-\frac{\alpha_{\text{Red}} F \eta}{R_G T}} \right) \quad (2.7)$$

with α the charge transfer coefficient, R_G the universal gas constant, T the temperature and j^* the exchange current density [$A m^{-2}$] [4].

The BV equation links the reaction rate to the electric and ionic potentials as well the concentrations of the reactant species. The reaction rate goes to zero when the over potential is zero and when the concentration reactant species $C_{\text{Red/Ox}}$ at the electrode surface is depleted. However, both the over potential and concentration depend on the reaction rate themselves. Combining the BV equation with the conservation and transport equations to model the linked effects between current, potential and concentration results a model for the full electrochemical performance of a SSFB. This will be discussed next.

Tertiary Current Distribution

To model the full electrochemical performance of a SSFB, the effects of reaction kinetic, Ohmic resistance and concentration gradients are linked in a so called tertiary current distribution [37][58]. A short overview of this will be given here.

The reaction kinetics defined by the BV equation (2.7) can be linked to the concentration gradients via the source term of the convection diffusion equation

$$\frac{\partial C_r}{\partial t} + \nabla \cdot (\mathbf{u} C_r) = \nabla \cdot (D_{r,eff} \nabla C_r) + \frac{F z_r}{RT} \nabla (D_{r,eff} C_r \nabla \phi) - a_R j_{\perp} \quad (2.8)$$

with the reactant concentration $C_r(\mathbf{x}, t)$ [$mol m^{-3}$], $D_{r,eff}$ the effective diffusion coefficient [$m^2 s^{-1}$] [44] and z_r the charge of reactant r . In a flow battery the convection will dominate the mass transfer and the limiting factor for the reactant concentration going to zero can easily be resolved by pumping more reactant into the electrochemical stack [22].

The effect of reaction kinetics on electric potential Φ can be derived via the charge conservation equation

$$\nabla \cdot \mathbf{j} = \frac{\partial \rho_c}{\partial t} \quad (2.9)$$

together with ohms law (2.2), Faraday's law (2.5) and the definition of the electric field (2.3). These equations combine to the non-linear differential equation

$$-\nabla \cdot \sigma(\nabla \Phi) = n_e F a_R j_{\perp}(\Phi) \quad (2.10)$$

where the electric potential $\Phi(\mathbf{x}, t)$ depends on space and time. When considering turbulent flow in a SSFB the electronic conductivity $\sigma(\mathbf{x}, t)$ will also depend on space and time due to its dependence on shear rate, as was mentioned in section 2.1.3.

Solving the tertiary current distribution is usually done using the COMSOLTM metaphysics engine and results in the ionic and electronic potential fields and current distribution [55]. Using this the effective CB Ohmic resistance $\Delta E_{electric}(\mathbf{x})$ can be determined.

However, due to the combined complexities of the shear thinning rheology, variable CB conductivity and turbulent flow profile this can not be easily implemented. This research therefore uses a simplified method to characterise the CB Ohmic resistance. This method will be discussed next.

2.1.5. Carbon Black Resistance

To characterise the effect turbulence has on the electrical conductivity and resistance of a Carbon Black suspension inside a SSFB, the following assumption will be made. Instead of incorporating varying electrical current paths, all the reactions are assumed to take place at the membrane. The channel will be considered as a variable cuboidal conductor, with a voltage difference applied from the membrane to the current collector side, as illustrated in the figure 2.3. This hypothetical situation does not represent the expected behaviour of a SSFB, where the reactions are expected to take place near the current collector since the ion conductivity is way larger than the electron conductivity [64]. However, it does provide a good measure for overall CB resistance and the effects turbulence has on it.

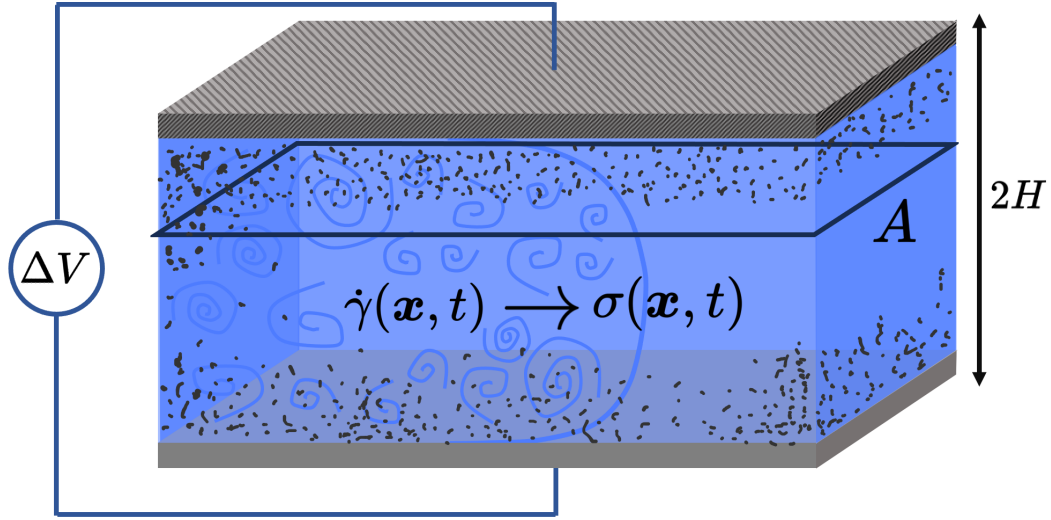


Figure 2.3: Figure shows a single flow channel represented as a cuboidal conductor with variable conductance $\sigma(x, t)$ due to the variable shear rate $\dot{\gamma}(x, t)$. The area A represents the area of the current collector and ΔV the externally applied potential difference.

If all the reactions take place near the membrane, the current will need to pass the full channel or electrode height to the current collector and the reaction rate will remain zero over the full channel. The charge conservation equation (2.9) can therefore be rewritten in the same way as (2.10) with $j_{\perp} = 0$

$$-\nabla \cdot \sigma(\nabla\Phi) = 0 \quad (2.11)$$

resulting in a potential conservation equation.

The channel with varying turbulent flow field and subsequent varying shear rate $\dot{\gamma}(x, t)$ and resulting varying conductivity $\sigma(x, t)$ is therefore seen as a varying cuboidal conductor. The CB electronic resistance R is computed by applying a voltage difference ΔV over the channel and using ohms law

$$R = \frac{\Delta V}{I} \quad (2.12)$$

with I representing the total current. The total current can be derived by solving equation 2.11 over this cuboidal conductor and using it to determine the current density j using equation (2.2). Finally the total current is obtained by integrating across all the current densities via

$$I = \iint_A \sigma(\mathbf{x}) \nabla\Phi(\mathbf{x}) dA \quad (2.13)$$

with A the area of the electrode.

To further characterise the conductivity an effective conductivity σ_{eff} is defined. Using Pouillet's law and the CB electronic resistance R this effective conductivity becomes

$$\sigma_{eff} = \frac{2H}{RA} \quad (2.14)$$

with H the channel half height and A the area of the electrode.

Using this total channel resistance R and effective conductivity σ_{eff} the effects of the varying turbulent CB conductivity fields $\sigma(x, t)$ will be further characterised. How equation (2.11) is solved, using the FVM, will be discussed in chapter 4

2.2. Fluid Dynamics Models

To study the effect of turbulence on the conductivity characteristics of the CB suspension in a SSFB, the turbulent non-Newtonian shear rate characteristics need to be modeled inside the flow channel. Fluid flow modeling is a vast field in physics and in this section an overview of the basic fundamental methods used for fluid modeling are touched upon. Specifically the different approaches used are categorised into three physical scales, namely the microscopic, mesoscopic and macroscopic scales. At the microscopic scale, the behavior of individual atoms and molecules is studied. In contrast, the macroscopic scale, is concerned with the behavior of systems that are large enough to be visible to the naked eye. The mesoscopic scale lies in between the microscopic and macroscopic scales and studies the statistical behaviour of clusters of atoms and molecules [42].

For the macroscopic scales the continuum theory is used which leads to the well know Navier-Stokes equations describing fluid motion. This fluid model will be discussed in Section 2.2.1. Furthermore, describing fluids in the microscopic scale is done using molecular dynamics theory whilst for the mesoscopic scale the kinetic theory is used. The kinetic theory is discussed in Section 2.2.2.

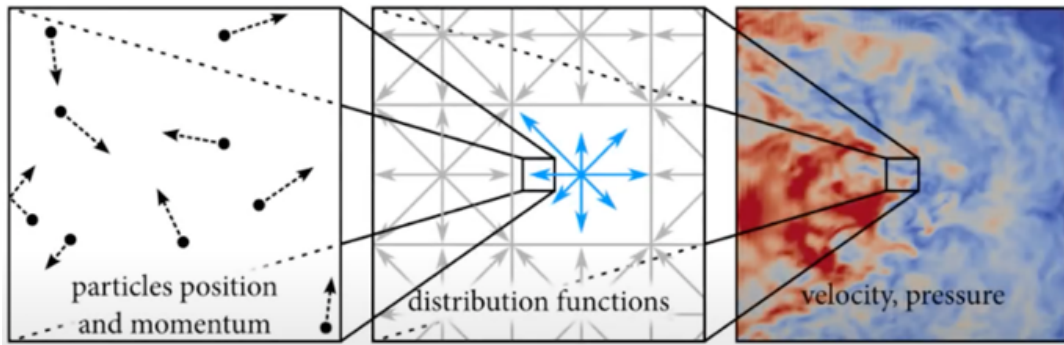


Figure 2.4: At the microscopic scale, the behavior of individual atoms and molecules is studied. In contrast, the mesoscopic scale focuses on the behavior of systems that are larger than individual atoms and molecules, but still small enough to be considered as a whole. The macroscopic scale, on the other hand, concerns with the behavior of systems that are large enough to be visible to the naked eye [42].

2.2.1. Navier-Stokes Equation

The continuum approach provides a mathematical framework for describing fluid dynamics in the scale where the behavior of individual fluid particles can be considered negligible. This scale is characterised by time and length scales for which the Knudsen number is smaller than $Kn < 0.01$ and within this scale the fluid flow can be described using classical mechanics [43]. In the continuum description the motion of the fluids are governed by the conservation of mass, the conservation of momentum and the conservation of energy. These conservation assumptions result in a set of partial differential equations known as the Navier-Stokes equations.

The Navier-Stokes equations are in fact a generalisation of Newton's first and second law of physics. When the mass in the system is conserved the change in density ρ is given by

$$\frac{\partial \rho}{\partial t} + \nabla \cdot (\rho \mathbf{u}) = 0 \quad (2.15)$$

with the second term describing the in and outflow of mass in a control volume. Using the conservation of mass, the generalisation of Newton's second law for fluids becomes

$$\rho \left(\frac{\partial \mathbf{u}}{\partial t} + (\mathbf{u} \cdot \nabla) \mathbf{u} \right) = -\nabla p + \nabla \cdot \left\{ \mu \left[\nabla \mathbf{u} + (\nabla \mathbf{u})^T - \frac{2}{3} (\nabla \cdot \mathbf{u}) \mathbf{I} \right] + \zeta (\nabla \cdot \mathbf{u}) \mathbf{I} \right\} + \rho \mathbf{g} \quad (2.16)$$

with \mathbf{u} the velocity and p the pressure of the fluid [5]. The molecular diffusion in the momentum equation is due to two different viscous forces represented by the dynamic viscosity μ and bulk viscosity ζ . These viscosities are the proportionality factors linking the fluid resistance or shear rate to the shear stress and compression stress respectively. In this research the viscosity wont be constant. How this so called non-Newtonian viscosity will be represented is discussed in Section 2.4.

Solving equation (2.16) results in the time and space dependent flow and pressure fields from which the shear rate and subsequent CB conductivity can be determined. Different methods like the Eulerian Finite Volume, Finite Element and Finite Difference methods and the Lagrangian Smoothed Particle Hydrodynamics method are all able to solve (2.16) directly [34].

2.2.2. Kinetic Theory

This study employs the Lattice Boltzmann Method, derived from kinetic theory, as an indirect approach to solving the Navier-Stokes equation. The upcoming section will discuss the theory behind the Kinetic Theory and the next section will dive deeper into the Lattice Boltzmann Method.

Kinetic theory is a mesoscale representation, that utilizes a particle distribution function to describe the behavior of collections of atoms or molecules in gasses and liquids. This particle distribution function is represented by $f(\mathbf{x}, \boldsymbol{\xi}, t)$ varying over space, time and velocity direction. It is defined in such a way that $f(\mathbf{x}, \boldsymbol{\xi}, t)d\boldsymbol{\xi}d\mathbf{x}$ represents the number of particles at time t in volume element $d\mathbf{x}$ around position \mathbf{x} , which have particle velocities in a range $d\boldsymbol{\xi}$ around velocity direction $\boldsymbol{\xi}$ [8]. Whilst the distribution function describes the fluid at a mesoscale, macroscopic fluid properties can be recovered from it via equations

$$\rho(\mathbf{x}, t) = \iiint f(\mathbf{x}, \boldsymbol{\xi}, t)d^3\boldsymbol{\xi} \quad (2.17)$$

and

$$\rho(\mathbf{x}, t)\mathbf{u}(\mathbf{x}, t) = \iiint \boldsymbol{\xi} f(\mathbf{x}, \boldsymbol{\xi}, t)d^3\boldsymbol{\xi}. \quad (2.18)$$

with $\mathbf{u}(\mathbf{x}, t)$ the macroscopic velocity vector [42].

To find the evolution of the distribution function the Boltzmann equation is used. It expresses the rate of change of the distribution function as the result of collisions between particles and the external forces acting on them. The full Boltzmann equation is given by

$$\underbrace{\frac{\partial f}{\partial t} + \boldsymbol{\xi} \cdot \nabla f}_A + \underbrace{\frac{F_\beta}{\rho} \nabla_\xi f}_B = \underbrace{\Omega(f)}_C \quad (2.19)$$

where A describes the advection of f , B the body forces affecting velocity and C the source term of f also called the collision operator [72]. This collision operator in its most general form is described by a double integral over velocity space considering all possible outcomes of a two-particle collision. It conserves mass, momentum and translational energy whilst making sure that the distribution function f locally evolves towards its equilibrium f^{eq} . This Maxwell-Boltzmann equilibrium function originates from gas theory and takes the form of

$$f^{eq}(\mathbf{x}, \boldsymbol{\xi}, t) = \rho \left(\frac{1}{2\pi RT} \right)^{3/2} e^{-|\boldsymbol{\xi}|^2/(2R_G T)} \quad (2.20)$$

with R_G the gas constant and T the temperature [51].

Using a technique called the Chapman-Enskog analysis, it can be proven that the Boltzmann equations recovers to the macroscopic fluid characteristics governed by the Navier-Stokes equations (2.16). This will be further discussed in section 2.3.2. To solve the Boltzmann equation numerically and with that the macroscopic fluid properties defined by the Navier Stokes equations, the Lattice Boltzmann Method is used. In the next section this method will be elaborated on further.

2.3. Lattice Boltzmann Method

In this research the Lattice Boltzmann Method (LBM) will be used to model the turbulent non-Newtonian flow field inside a SSFB. The LBM will be used over the more conventional CFD methods due to its computational efficiency, inherent parallelisation potential [42] and relative ease of implementation. The LBM does however require large amounts of data restricting the upscaling ability of the implementation. When this restriction is overcome using a GPU, the LBM will enable the completion of the high resolution turbulent non-Newtonian simulations needed in this research, within a reasonable time frame [38].

In this section an overview is given on how the LBM arises from kinetic theory (section 2.3.1) and how it links to the Navier-Stokes equation using the Chapman Enskog analysis (section 2.3.2). Finally

the iterative process solving the Lattice Boltzmann equation is described in section 2.3.3. In the next chapter the full implementation of the specific Filter Matrix-LBM model used in this research to solve the LBM, will be elaborated on.

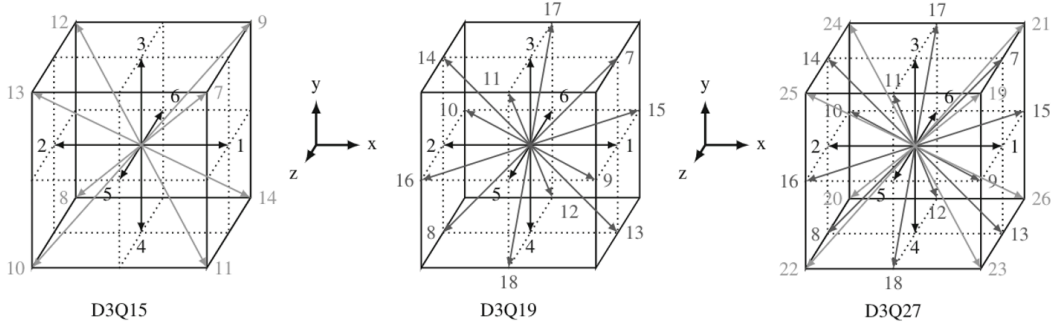


Figure 2.5: Different 3D velocity discretization schemes used to discretize the Boltzmann equation over velocity [42].

2.3.1. Discretization of the Boltzmann Equation

To find the macroscopic fluid characteristics using kinetic theory, the Boltzmann equation (2.19) needs to be solved numerically. To do so the distribution function f is discretised over space \mathbf{x} , time t and microscopic velocity ξ reducing the number of degrees of freedom [42]. To discretise ξ different 3D velocity schemes can be used such as D3Q15, D3Q19 and D3Q27 where the velocity resolution increases accordingly, as can be seen in figure 2.5. The discretised Lattice Boltzmann equation describes the evolution of particle density corresponding to every discretised velocity $f_i(\mathbf{x}, t)$. It takes the form of

$$f_i(\mathbf{x} + \mathbf{c}_i \delta t, t + \delta t) - f_i(\mathbf{x}, t) = \Omega_i(\mathbf{x}, t) \quad (2.21)$$

with \mathbf{c}_i the discretised velocity direction, δt the discretised time step and Ω the before mentioned collision operator [42]. Ω depends in a non-linear matter on f_i such that mass and momentum are conserved, expressed by

$$\sum_i \Omega_i(f_i) = 0 \quad \sum_i \mathbf{c}_i \Omega_i(f_i) = \rho \mathbf{g} \quad (2.22)$$

with $\rho \mathbf{g}$ representing the body force [23]. The discretised Maxwellian equilibrium distribution function (2.20) becomes [42]

$$f_i^{eq} = w_i \rho \left(1 + \frac{\mathbf{c}_i \cdot \mathbf{u}}{c_s^2} + \frac{(\mathbf{c}_i \cdot \mathbf{u})^2}{2c_s^4} - \frac{\mathbf{u} \cdot \mathbf{u}}{2c_s^2} \right) \quad (2.23)$$

where c_s represents the lattice speed of sound and w_i the lattice weights. Both c_s and w_i differ per velocity discretisation scheme.

2.3.2. Chapman Enskog Expansion

It can be shown that for Eulerian non-viscous flows the particle distribution f_i takes the form of the equilibrium distribution f_i^{eq} [42]. To find the non-equilibrium contribution to f_i that incorporates the viscous dissipation found in the NS equation the Chapman-Enskog method is used [14].

The primary concept behind determining this $f_i^{neq} = f_i - f_i^{eq}$ contribution involves representing f_i as a perturbation expansion around f_i^{eq} :

$$f_i = f_i^{eq} + \epsilon f^{(1)} + \epsilon^2 f^{(2)} + \dots \quad (2.24)$$

The ϵ represents a smallness parameter and acts as a label to later remove higher order terms from the equation. This perturbed f_i is substituted in the first order expansion of the LBM equation (2.21) which takes the form of:

$$\partial_t f_i = \Omega_i(f) - \mathbf{c}_i \cdot \nabla f_i \quad (2.25)$$

If the time scale ∂_t and spatial scales ∇ are also expanded and only the first two orders of f_i are considered, the solution for f_i^{neq} can be found [42]. The distribution function incorporating viscous

dissipation then becomes

$$f_i = \rho w_i \left(1 + \frac{\mathbf{c}_i \cdot \mathbf{u}}{c_s^2} + \frac{(\mathbf{c}_i \cdot \mathbf{u})^2}{2c_s^4} - \frac{\mathbf{u} \cdot \mathbf{u}}{2c_s^2} - \nu \left[\frac{(\mathbf{c}_i \cdot \nabla)(\mathbf{c}_i \cdot \mathbf{u})}{c_s^4} - \left(1 + \frac{2}{D} - B\right) \frac{\nabla \cdot \mathbf{u}}{c_s^2} \right] \right) \quad (2.26)$$

where the viscous term represents f_i^{neq} [88]. In (2.26) the $B = \zeta/\nu$ represents the lattice bulk viscosity over the local lattice kinematic viscosity. D represents the spatial dimension of the scheme. This B is usually chosen to be equal to 1 but as discussed in chapter 3 it can be seen as a free parameter aiding in numerical stability [88].

Using the conservation criteria for the collision operator (2.22) it can be shown that f_i recovers the full Navier-Stokes equation (2.16) up to second order accuracy [29]. Solving the LBM using an appropriate collision operator leads to the macroscopic quantities in the continuum domain

$$\rho(\mathbf{x}, t) = \sum_i f_i(\mathbf{x}, t) \quad \rho(\mathbf{x}, t)\mathbf{u}(\mathbf{x}, t) = \sum_i c_i f_i(\mathbf{x}, t) \quad p = \rho c_s^2 \quad (2.27)$$

2.3.3. Stream and Collision Step

To solve the Lattice Boltzmann equation (2.21), and therefore finding how f changes over time and space, two iterative steps need to be taken. These two steps are the stream and collision step as seen in figure 2.6. In the stream step the distribution functions are propagated to the neighboring nodes along their velocity directions. In the collision step the particle densities are redistributed over the velocities such that mass, momentum and energy are conserved. Therefore, to close the system a collision operator, incorporating the macroscopic fluid properties, needs to be found.

Different kinds of collision operators have been developed with the most common ones being the Bhatnagar Gross Crook (BGK) -, Multiple Relaxation Time (MRT) - and the Filter Matrix (FM) - Lattice Boltzmann Method [42]. In this study, the FM-LBM will be used. In section 3.1 the derivation and implementation of this model will be discussed.

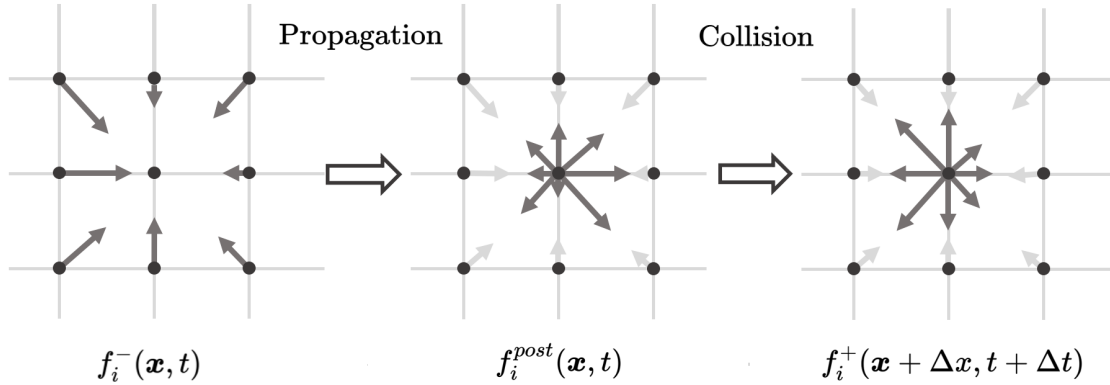


Figure 2.6: Stream and Collision step

2.4. Non-Newtonian Fluids

As mentioned in section 2.1.3 the aqueous Carbon Black suspension inside the proposed Semi-Solid Flow Battery design exhibits strong non-Newtonian behaviour. Non-Newtonian fluids distinguish themselves from Newtonian fluids by their variable molecular viscosity. This is due to the apparent viscosity ν of such non-Newtonian (NN) fluids being dependent on the velocity gradients in the fluid and in some cases also elastic effects [9]. In section 2.4.1, a short overview is given on the distinction between Newtonian and non-Newtonian and the different types of NN-fluids will be discussed. After this introduction into NN-fluids, the power-law viscosity model approximating the Carbon Black viscosity characteristics will be introduced in section 2.4.2.

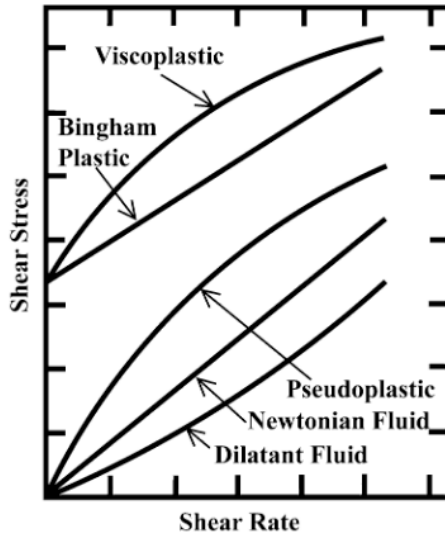


Figure 2.7

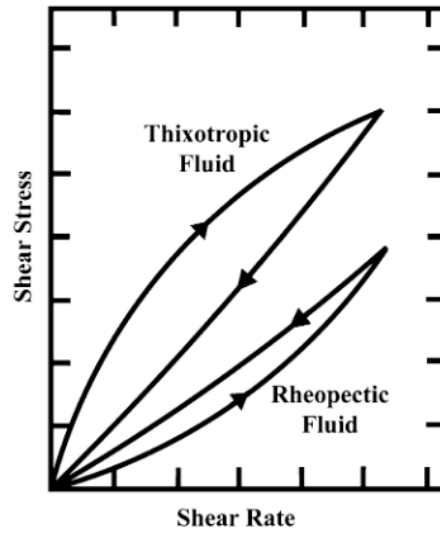


Figure 2.8

Figure 2.7 represent the characteristics of different time in-dependent non-Newtonian fluids where figure 2.8 does so for time dependent fluids [16].

2.4.1. Different Classes of non-Newtonian Fluids

Most fluids that consist of particles with low molecular weight like for example water, molten metals, alcohol and dissolved salts, exhibit Newtonian flow behaviour [9]. This means that the shear stress τ linearly scales with the shear rate $\dot{\gamma}$

$$\tau = \mu \dot{\gamma} \quad (2.28)$$

with μ representing the viscosity [16]. However, with non-Newtonian flows like suspensions (e.g. quicksand), emulsions (e.g. butter) and polymeric solutions (e.g. molten plastics) this shear stress and shear rate relation is strictly non-linear. These varying viscosity characteristics, or so called rheologies, generate non-linear stress responses in the fluid.

Depending on the type of non-Newtonian fluid, the apparent viscosity increases or decreases for intensifying shear rates. For a specific class of fluid this shear-thickening and shear-thinning behaviour can on top of that also change over time. The time independent non-Newtonian fluids are called purely viscous or generalised Newtonian flows whereas the time dependent or partially time dependent non-Newtonian fluids are called viscoelastic or elastico-viscous fluids [16].

The flow curves of the different kinds of time independent fluids can be found in figure 2.7. In this figure it can be seen that for pseudo-plastics (also called polymeric fluids) the viscosity decreases with increased shear rate constituting shear-thinning behaviour. For dilatant fluids the viscosity increases with shear rate, constituting shear-thickening behaviour. In figure 2.8 the two kinds of time-dependent fluid types are displayed. The distinction between the two is that the viscosity of thixotropic fluids decreases over time whilst it increases over time for rheopectic fluids.

2.4.2. Power-law Viscosity Model

Non-aqueous Carbon Black suspensions exhibit strong shear-thinning and time dependent rheological characteristics [86][56]. To study the turbulent characteristics of this fluid, only the shear-thinning behaviour will be considered in this research. The fluid rheology is therefore assumed to be independent of its shear rate history. To further generalise the rheological properties a model will be used to approximate the experimentally obtained viscosity dependence on shear rate. This approximation, using the power-law viscosity model is done to study the turbulence characteristics of shear thinning fluids in a more general way.

The power-law viscosity model is a time independent or generalised Newtonian fluid model. It uses a stress tensor τ in a simplified way w.r.t the full Navier-Stokes equation (2.16) by leaving out the compression terms. Here $\tau = 2\mu(\dot{\gamma})S$ only depends on a variable viscosity $\mu(\dot{\gamma})$ and the pure shear rate-of-strain tensor $S = \frac{1}{2}(\nabla u + (\nabla u)^T)$ [70][71][30]. The shear rate $\dot{\gamma}$ is defined as the second

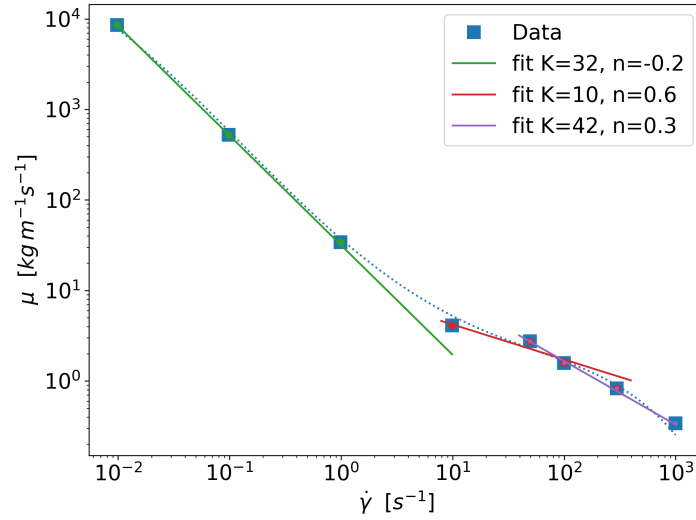


Figure 2.9: Non-aqueous CB suspension viscosity dependence on shear rate as found by Youssry *et al.* [86]. To different shear rate ranges in the experimental data the power-law viscosity is fitted.

invariant of the rate-of-strain tensor

$$\dot{\gamma} = (2\mathbf{S} : \mathbf{S})^{\frac{1}{2}} = \sqrt{2 \left(\frac{1}{2} \left(\frac{\partial u_i}{\partial x_j} + \frac{\partial u_j}{\partial x_i} \right) \right)^2} \quad (2.29)$$

The power-law (Ostwald–de Waele) model is then used to express the apparent molecular viscosity in terms of shear rate via

$$\mu(\dot{\gamma}) = \rho\nu(\dot{\gamma}) = K\dot{\gamma}^{n-1} \quad (2.30)$$

with K representing the consistency index in units of $[kg/m, m^{-1}s^{2-n}]$ and n the power-law index [16].

Figure 2.9 shows how different parts of the experimentally obtained viscosity curve of the CB suspension can be fitted to different power-law indices n . In the current research the non-Newtonian shear thinning behaviour of the CB suspension will be approximated with the power-law viscosity model. The next section will discuss how the fluid flow of the simplified CB rheology in a turbulent state will be characterised.

2.5. Turbulence

This research aims to quantify the turbulent channel flow profile characteristics of the shear thinning CB suspension via numerical simulation such to determine its effect on the internal resistance of a SSFB. To quantify the influence of turbulence on the internal resistance it is important to take a look at what turbulence is, how it can be simulated numerically and how it can be characterised statistically. This section will give an overview of the important concepts answering these three questions. Among other things the DNS simulation technique will be discussed in section 2.5.2. The turbulent statistics and Reynolds number, characterising turbulent flow, will be discussed in section 2.5.3 and 2.5.4.

2.5.1. What is Turbulence

Turbulence is a complex and chaotic flow of fluid that is characterized by disordered, unpredictable and fluctuating motion. It is a common phenomenon that can be observed in a wide range of fluid flows, including in the atmosphere, oceans, rivers, and in the pipes and ducts that transport fluids in industrial settings such as in a Semi-Solid Flow Battery.

In essence, turbulent flow adheres to the exact same Navier-Stokes equations (2.16) as laminar flow. These equations seem deterministic, meaning that if the initial conditions and boundary conditions are known, the future behavior of the fluid can be predicted and described by a unique solution. However, as the mathematician Hardamard pointed out in his 19 century paper, there is one extra condition that determines if a set of partial differential equations define a fully deterministic problem [35]. The third

condition states that for a so called well posed problem small disturbances in the initial or boundary conditions only lead to small variations in the final solution.

Turbulence is an example of an ill-posed problem since this third condition is not satisfied. Small perturbations in the initial and boundary condition make for small fluctuations in the flow profiles. For turbulent flows these small-scale, fluctuations in the fluid velocity, grow and interact in a way that has a large influence on the total flow profile. Since the boundary and initial conditions can in reality never be described infinitely precise, the final solution for turbulent flow can therefore not be fully predicted. Modeling turbulence therefore presents a significant challenge for scientists and engineers because it is difficult to predict and control. Despite this, much progress has been made in understanding turbulence and developing methods for simulating flows in the past 70 years [12]. The following sections will cover the essential concepts in turbulence simulation and statistical characterization to facilitate the quantification of the effects of turbulence on the flow profile of a CB suspension.

2.5.2. Direct Numerical Simulation

There are several different methods for simulating turbulent flows, including Direct Numerical Simulation (DNS), Large Eddy Simulation (LES) and Reynolds-Averaged Navier-Stokes (RANS) simulation. DNS is a high-precision method that solves the Navier-Stokes equations directly for all scales of motion. LES is a hybrid method that captures the large-scale motion using a filtered version of the Navier-Stokes equations, while the small-scale motion is modeled using subgrid-scale models. RANS is a statistical approach that involves averaging the Navier-Stokes equations over numerous time and spatial increments. This process yields a set of equations that characterize the mean flow and turbulence [34].

DNS is considered the most accurate method of simulating turbulent flows since it requires no modeling. However, this method requires the computational domain to be large enough to contain the large scale motions of size \mathcal{L} , while also having a high enough spatial resolution δx to describe the small scale eddies. Furthermore the simulation time step δt should be small enough to incorporate all the time varying fluctuations. The spatial and time resolution is described by the Kolmogorov length η_K and time τ_K scales given by

$$\eta_K = \left(\frac{\nu^3}{\epsilon} \right)^{\frac{1}{3}} \quad \tau_K = \left(\frac{\nu}{\epsilon} \right)^{\frac{1}{2}} \quad (2.31)$$

with ϵ representing the the average rate of dissipation of turbulence kinetic energy per unit mass, and ν the kinematic viscosity of the fluid [40]. Since ϵ is correlated with the intensity of the turbulence, a higher turbulent intensity requires a higher resolution. This scaling is found to be equal to

$$\mathcal{N} = \left(\frac{\mathcal{L}}{\eta_K} \right)^3 \propto \mathcal{O}(Re^{\frac{9}{4}}) \quad (2.32)$$

with \mathcal{N} the number of grid points and Re the Reynolds number which will be further discussed in section 2.5.4.

The main reason for selecting the DNS model in this research, rather than the RANS and LES models, is as follows. Both the RANS and LES models require a turbulence model, and the incorporation of complex rheologies in these models is not yet fully matured, particularly for the LBM. Given the complex rheology of the carbon black suspension, the decision was made to therefore opt for the full DNS approach.

2.5.3. Turbulent Statistics

As mentioned, turbulence is inherently unstable, chaotic and ill-posed meaning that every simulation with the same boundary conditions (BC) and initial conditions (IC) generates different flow profiles. To still be able to characterise the flow, turbulent statistics are used. With these statistical characteristics, simulations can be compared and statements about the reliability of the results can be made. In this research three different statistical concepts are used to compare the simulation results with literature values namely: averages, fluctuating components and two point correlations. This section discusses all of them.

Firstly, for the turbulent flow field quantities such as the velocity components u_i , vorticity components ω_i and shear rate $\dot{\gamma}$, the instantaneous quantity can be split into an average plus a fluctuation component.

This so called Reynolds decomposition is given by

$$\mathbf{u} = \bar{\mathbf{u}} + \mathbf{u}' \quad (2.33)$$

with the bar denoting the average and the fluctuation term indicated by a prime [59]. Using this decomposition the following statistical measures are used:

- The average inside a turbulent flow field is defined as the assembly average. When the flow field is statistically converged this assembly average can be obtained by averaging over space and time [59]. The time average \bar{u}_i can be obtained by measuring the observable over a period of time and taking the average of the readings. For the spatial average $\langle u_i \rangle$ the observable is averaged over a cross sectional area for which the same behaviour is expected. In the numerical research that follows the assembly average, combining both spatial and temporal averages, will be denoted with an overline.
- To quantify the fluctuations the Reynolds stress tensor is used. This component of the stress tensor in the Reynolds Averaged Navier Stokes equation accounts for the turbulent fluctuations in fluid momentum [59]. For constant density, the Reynolds stress is written as

$$\tau''_{ij} = \overline{u'_i u'_j}, \quad (2.34)$$

or the average fluctuating velocity components. Closely related to the Reynolds stress components are the root mean square velocity fluctuation which are defined as

$$u'_{i,RMS} = \sqrt{\overline{u'_i u'_i}}, \quad (2.35)$$

and the turbulent kinetic energy defined as

$$k = \frac{1}{2} (\overline{u'u'} + \overline{v'v'} + \overline{w'w'}), \quad (2.36)$$

where (u, v, w) correspond to the x, y, z velocity's respectively.

- The last statistical quantity considered in this research is the two-point spectral correlation function. Where the above two statistical quantities only describe the single point turbulent statistics, constituting first order statistics, the correlation function describes the spatial structure of turbulence which is called second order turbulence [59]. The two point correlation $\overline{u'_i(\mathbf{x}_1)u'_j(\mathbf{x}_2)}$ is a function the separation vector $\mathbf{r} = \mathbf{x}_1 - \mathbf{x}_2$. The correlation tensor can therefore be written as

$$R_{ij}(\mathbf{r}) = \overline{u'_i(\mathbf{x}_1)u'_j(\mathbf{x}_2)}, \quad (2.37)$$

and describes the longitudinal, transversal and cross-correlations in six independent components [59]. In this research the longitudinal point correlation is used to estimate the characteristics longitudinal length scale \mathcal{L}_L via

$$\mathcal{L}_L = \frac{1}{u'^2} \int_0^\infty R_{xx}(r_x, 0, 0) dr_x = \frac{1}{u'^2} \int_0^\infty \overline{u'(x)u'(x+r)} dr, \quad (2.38)$$

which is a good measure for the large scale turbulent motion in channel flow [59][30].

2.5.4. Reynolds Number

The Reynolds number is a dimensionless parameter that is used to characterize the relative importance of inertial forces to viscous forces in a fluid flow. It is defined as the ratio of the fluid's inertia to the viscosity forces, and is given by the equation

$$Re = \frac{UH}{\nu}, \quad (2.39)$$

with U the characteristic velocity and H the characteristic length scale.

In fluid dynamics, the distinction between laminar and turbulent flow is often made based on the value of the Reynolds number. For duct flows with Reynolds numbers below $Re < 3000$, the viscous

forces dominate and the flow is typically laminar. In contrast, for larger Reynolds numbers, the inertial forces dominate and the flow is typically turbulent. Inside the turbulent regime the Reynolds number is also used as the single non-dimensional parameter to compare the complex dynamics of turbulent flow with other numerical studies and experiments. By varying the Reynolds number in the simulation, the effects of different turbulent characteristics on the internal resistance of a SSFB can also be quantified.

There are different definitions of Re numbers that all depend on the choice of characteristic velocity and length scale. Examples are the center-line Reynolds number Re_c defined with the velocity in the center-line $U = U_c$ or the mean velocity Reynolds number Re_m with the mean velocity $U = U_m$. In turbulent channel flow research another common definition of the Reynolds number is the wall shear stress turbulent Reynolds number given by

$$Re_\tau = \frac{u_\tau H}{\nu} \quad (2.40)$$

with u_τ the wall friction velocity which is defined as

$$u_\tau = \sqrt{\frac{\tau_w}{\rho}} \quad (2.41)$$

with τ_w representing the statistically averaged wall shear stress [59].

For non-Newtonian fluids the viscosity can vary over space and time. It is therefore in general unclear what viscosity scale to use when defining a non-Newtonian Reynolds number. However, for some specific non-Newtonian viscosity models such as the power-law viscosity model used in this research, there are viscosity scales that result in useful Reynolds numbers. This study makes use of the wall viscosity ν_w as the relevant viscosity based on a discussion of various options by [71]. This viscosity scale results in the so called generalized Reynolds number defined as [50]

$$Re^G = \frac{UH}{\nu_w} = \frac{\rho U H}{K^{\frac{1}{n}} \tau_w^{1-\frac{1}{n}}} \quad (2.42)$$

which can be rewritten to the wall shear stress general Reynolds number

$$Re_\tau^G = \frac{\rho u_\tau H}{K^{\frac{1}{n}} \tau_w^{1-\frac{1}{n}}} \quad (2.43)$$

used in this research.

The generalised Reynolds number enables the Re_τ number to be determined in advance by using the relation for wall shear stress

$$\tau_w = \rho g H, \quad (2.44)$$

which directly follows from the macroscopic force balance in a channel [71]. With the help of the wall shear velocity and viscosity, all further parameters can be non-dimensionalised via

$$w^+ = \frac{u}{u_\tau} \quad z^+ = \frac{z u_\tau}{\nu_w} \quad t^+ = \frac{t u_\tau}{H} \quad \dot{\gamma}^+ = \frac{\dot{\gamma} \mu_w}{\tau_w}. \quad (2.45)$$

Using this non-dimensionalization together with the generalised Reynolds number and statistical quantities, the turbulent flow can be fully characterized. This enables the comparison of the turbulent fluid flow simulation in this research with literature values.

2.6. Parallel Programming on a Graphics Processing Unit

In this last section of the theory chapter, a shift is made from the physics theory behind electrochemical and fluid flow modeling to the computer science topic of implementing these models on high performance computers. This shift is needed since the turbulence simulations aimed for in this research will require a large amount of computations to comply with the resolution and domain size restrictions of DNS. As an example, the LBM simulation by Amati *et al.* sequentially reads in a 0.6 GB distribution function, changes every one of its 80 million entries and finally writes it back in memory more than a million times [3]. If every entry in this array were changed sequentially, the total computation time for such a simulation would span a lifetime.

Luckily, the LBM is easily broken down into small parts that can be solved in parallel, significantly reducing the total simulation time [42]. Although this can be done on a central processing unit (CPU), the Graphics Processing Unit (GPU) architecture has shown three hundred-fold performance gains compared to traditional CPU-based LBM implementations. This remarkable improvement is attributed to the highly parallel structure of the GPU, making it an attractive alternative for CFD simulations. This makes it a compelling alternative for Computational Fluid Dynamics (CFD) simulations [10]. This theoretical section aims to explore the concepts of parallel programming and the GPU architecture, with a particular focus on the NVIDIA specific Compute Unified Device Architecture (CUDA) programming language.

The advantages of parallel programming for the turbulent LBM simulations will be discussed in section 2.6.1. After this, an overview of the differences between GPU's and CPU's programming will be given in section 2.6.2. Section 2.6.3 will finalize this theoretical section with an overview of the NVIDIA specific GPU hardware and software hierarchies. In the next chapter, the exact FM-LBM implementation on the GPU will be discussed using the theory discussed here.

2.6.1. Parallel Programming

Parallel programming is a technique that involves breaking down a large computational task into smaller subtasks that can be executed simultaneously on multiple processing units, such as CPU cores or GPU threads. This approach enables faster execution of the task by exploiting the available processing power in parallel, rather than relying on a single processing unit to perform the entire task sequentially.

There are two main challenges when writing parallel algorithms. The first challenge is finding possibility's of breaking up the code efficiently to allocate tasks to available resources for simultaneous execution. Ideally, using N times more processors should result in N times faster computation or processing of N times more data in a fixed time. However, if the algorithm steps depend heavily on each other, they cannot take advantage of the additional resources and must run sequentially. The measure of an effective parallel implementation is the parallel efficiency, where the ideal situation of n more processors leading to an n -time reduction gives an efficiency of 100% [81]. Luckily the LBM is inherently parallelisable due to the collision step being totally independent of its neighbours and the stream step only requiring information of its next neighbours. Therefore, these steps can be easily broken down into many parts that can be executed efficiently in parallel [42].

The second challenge is making sure the program avoids race conditions. In programming, two forms of race conditions are considered [66]. The first occurs when multiple threads that solve different parts operate at different speeds and the algorithm that moves does not wait for both threads to finish. A good analogy for this is a car factory where the chassis and engine, both from different assembly lines, are combined before the engine is fully finished. The second race condition, also known as the data race condition, is when two threads write to the same piece of data simultaneously resulting in undefined memory corruption [80].

The programming techniques and tools used for overcoming the above-mentioned challenges in programming parallel systems depend on the organization of processors and memories within a parallel computer. The next section will discuss these different parallel systems.

2.6.2. CPU vs GPU

In the realm of parallel computing, there exist three primary paradigms that take advantage of different architectures: shared memory systems, distributed memory systems, and the GPU [24]. These different system architectures, schematically depicted in figure 2.10, can be characterised as follows.

- **Shared Memory Systems:** These systems consist of a CPU with multiple cores, all connected to the same shared random access memory (RAM). The computations are done on the CPU cores with high clock speeds, and information is shared via vast cache memory and easy RAM access. CPU's also have large control units that direct the operation of the processor, increasing the speed of the process [31]. The main advantage of shared memory systems is their ease of programming using for example the OpenMP programming interface (API) [13]. However, the main disadvantage is that scaling to larger systems becomes difficult due to limitations in the number of processors that can access shared memory.
- **Distributed Memory Systems:** These systems try to overcome the constraints of shared memory systems by coupling many CPU's together using a messaging passing algorithm like MPI [52].

Using the MPI protocol, shared results as well as synchronization messages are sent between the distributed systems through a connective network. Distributed memory systems are highly scalable and can be used to build very large systems with thousands of processors. However, the MPI protocol is more complex than the protocols used for shared memory systems. Also, the parallel efficiency is very much restricted by the connection speed of the network connecting the CPU's [24].

- **GPU systems:** Apart from speeding up code using conventional processors, one can also make use of a specialized co-processor like a GPU. Where a CPU is built to execute one task as fast as possible, a GPU is a processor built for executing as many tasks at the same time as possible. GPU's are therefore made up of multiple orders of magnitude more cores than a CPU enabling a task to be broken down in many more parts that can all be run in parallel. This drastically improves the instruction throughput and memory bandwidth of a GPU compared to a CPU. The drawback of a GPU w.r.t. to a CPU is the low clock speeds of the individual GPU cores as well as a significantly lower amount of cache memory creating memory latency when code is executed in an nonoptimal way [24]. Therefore, to fully unlock the GPU's potential, these factors need to be overcome with an efficient algorithm. To write this efficient algorithm for a GPU different API's can be used. For NVIDIA GPU's the CUDA api is usually used [19].

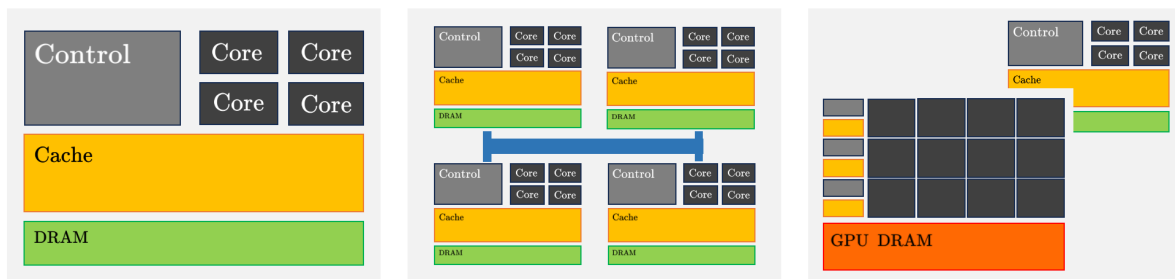


Figure 2.10: Difference in Shared Memory Systems, Distributed Memory Systems and GPU Systems.

2.6.3. GPU Hierarchies

To enable the GPU's full potential, it is vital to understand how the CUDA programming language interacts with the GPU hardware. To this end we will look at three hierarchies that lay the groundwork in understanding the NVIDIA GPU programming language, memory management and hardware specifications.

Software Hierarchy

NVIDIA GPU's make use of the CUDA programming language. This programming language breaks the code up into kernels that represent the code to run in parallel [19]. To manage the sequence of execution and the memory access pattern of each execution of this kernel, the computational domain outlined by the kernel is divided into three levels: threads, blocks, and grids. These three levels are represented in figure 2.11 and are defined as follows.

- **Threads** represent a single execution of a kernel.
- **Blocks** represent a group of threads that are executed at the same time. For every kernel, the number of threads per block is equal.
- **Grids** represent the full computational domain defined by the kernel. The thread/block/grid configurations can vary across different kernels.

Memory Hierarchy

The next hierarchy that will be discussed is the memory hierarchy. Due to the small cache memory and control unit for every thread, an non-optimal use of memory can lead to a substantial loss of parallel efficiency. A solid understanding of the memory hierarchy is therefore vital when writing efficient CUDA code. The most important memory forms are ordered here by thread access speed, going from fastest to slowest [19].

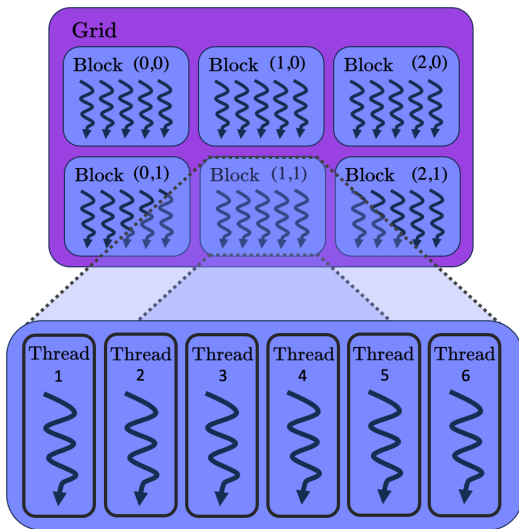


Figure 2.11

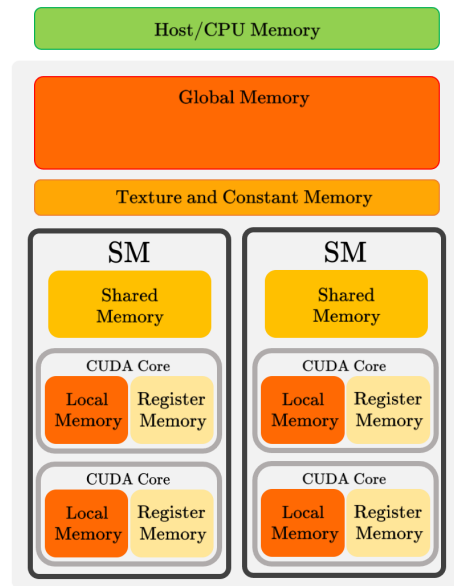


Figure 2.12

Figure 2.11 shows a schematic depiction of the thread, blocks and grid hierarchy used by the CUDA API to let the kernel know where to access memory. The memory and hardware hierarchy of a GPU is depicted in Figure 2.12

- **Register memory** is the fastest memory and is private to threads.
- **Shared memory** is also fast memory that is accessible for all threads in one block.
- **Constant and Texture memory** is read only and is private to a kernel.
- **Local memory** is part of global memory and therefore slow. It is private to threads and is used when the register spills.
- **Global memory** is slow memory private to a kernel and accessible by all threads.
- **Host memory** is the memory of the CPU that sends the kernel task to the GPU. The connection between global memory and host memory is very slow.

Hardware Hierarchy

Finally everything comes together in the hardware hierarchy, as depicted in Figure 2.12. At the core of the NVIDIA GPU architecture lie multiple streaming multiprocessors (SMs), each of which has its own set of CUDA cores that can execute threads concurrently. These SMs have a warp scheduler that organizes threads into groups of 32, called warps, and schedules them for execution on a set of available CUDA cores [19]. The number of SMs and CUDA cores per SM vary per device, but if, for example, there are 8 cores per SM it takes 4 clock cycles to execute all 32 threads in one warp. The warp scheduler optimizes the performance of the GPU by minimizing the number of instructions that are stalled or idle, resulting in efficient processing of data.

To bring it all together, the CPU functions are rewritten as kernels to implement the code on a GPU. Kernels are executed from the host CPU and can only access memory that is sent from the CPU to the GPU. Where a function iterates over the computational domain using loops, the GPU uses the aforementioned software hierarchy system built up of threads, blocks, and grids. This software hierarchy lets the kernel know what part of global memory it needs to change, and it also determines which kernels are executed at the same time in the SM and can therefore access shared memory. The kernel takes as input the number of threads per block (tpb) and blocks per grid (bpg), which determines the threads that are executed at the same time in an SM. Due to the large difference in memory bandwidth between the different types of memory, determining tpb and bpg, as well as managing other memory access, is very important. The decisions made in implementing FM-LBM on the GPU are elaborated on in Section 3.5.

3

Fluid Dynamics Model

This chapter is dedicated to the implementation of the model that utilizes the LBM to describe the turbulent flow inside an SSFB. The CB suspensions inside this SSFB exhibits strong shear-thinning non-Newtonian behavior, making the viscosity range for which the fluid model needs to operate large. To accurately model this non-Newtonian turbulent behavior, the FM-LBM collision operator is used. The FM-LBM has been shown to be more stable than MRT-LBM and BGK-LBM [89], where especially BGK-LBM shows problems with low viscosity [15][42]. Section 3.1 discusses the specifics of the FM-LBM model, where 3.2 discusses the initial and boundary conditions used. To be able to simulate turbulent flows via the high-fidelity DNS method the large amounts of calculations are preformed on a GPU. Section 3.5 explains in detail the implementation of FM-LBM on the GPU.

3.1. Filter Matrix Lattice Boltzmann Method Implementation

The Filter Matrix Lattice Boltzmann Method (FM-LBM) is a method developed by Somers *et al.* [75] and subsequently extended to D3Q19 by Zhou and Zhong [89][88].

To find the collision operator $\Omega(N_i)$ that mimics the average effect of collision, the FM-LBM makes use of a staggered grid. This staggered grid shifts the Lattice Boltzmann equation (2.21) half a grid node and time step

$$f_i \left(\mathbf{x} + \frac{\mathbf{c}_i \delta t}{2}, t + \frac{\delta t}{2} \right) - f_i \left(\mathbf{x} - \frac{\mathbf{c}_i \delta t}{2}, t - \frac{\delta t}{2} \right) = \Omega_i(\mathbf{x}, t) \quad (3.1)$$

Subsequently this shifted equation is Taylor expanded around $f_i(\mathbf{x}, t)$

$$f_i \left(\mathbf{x} \pm \frac{\mathbf{c}_i \delta t}{2}, t \pm \frac{\delta t}{2} \right) = f_i(\mathbf{x}, t) \pm \frac{\delta t}{2} \mathbf{c}_i \cdot \nabla f_i(\mathbf{x}, t) \pm \frac{\delta t}{2} \partial_t f_i(\mathbf{x}, t) + \mathcal{O}(\delta t^2) \quad (3.2)$$

where the higher order terms are omitted. By substituting the distribution function $f_i = f_i^{eq} + f_i^{neq}$ (2.26), found using the Chapman-Enskog expansion, into (3.2) one finds the collision operator

$$\Omega_i(f) = \frac{\rho w_i}{c_s^2} ((\mathbf{c}_i \cdot \nabla)(\mathbf{c}_i \cdot \mathbf{u}) - c_s^2 \nabla \cdot \mathbf{u} + \mathbf{c}_i \cdot \mathbf{g}) \quad (3.3)$$

where \mathbf{g} represents the body force term. In this derivation, the mass conservation equation (2.15) is used, as well as a simplification of the Navier-Stokes equation in the form of $\partial_t \rho \mathbf{u} \approx -\nabla p + F = -\frac{1}{c_s^2} \nabla \rho + F$ [75].

Combining the first order Taylor expansion of the LBM equation (2.25) with the second order Taylor expansion of the staggered LBM equation (3.2) one can now derive the FM-LBM

$$f_i \left(\mathbf{x} \pm \frac{\mathbf{c}_i \delta t}{2}, t \pm \frac{\delta t}{2} \right) = f_i(\mathbf{x}, t) + \frac{\delta t}{2} \Omega(f_i) \quad (3.4)$$

Substituting (2.26) and (3.3) into this equation leads to the full distribution function:

$$f_i \left(\mathbf{x} \pm \frac{\mathbf{c}_i \delta t}{2}, t \pm \frac{\delta t}{2} \right) = \begin{cases} \rho \omega_i \left[1 + \frac{\bar{c}_i \cdot \bar{\mathbf{u}}}{c_s^2} + \frac{1}{2} \left(\frac{(\bar{c}_i \cdot \bar{\mathbf{u}})^2}{c_s^4} - \frac{\bar{\mathbf{u}} \cdot \bar{\mathbf{u}}}{c_s^2} \right) \right. \\ \left. - \nu \left(\frac{(\bar{c}_i \cdot \bar{\nabla})(\bar{c}_i \cdot \bar{\mathbf{u}})}{c_s^4} - \left(1 + \frac{2}{D} - B \right) \frac{\bar{\nabla} \cdot \bar{\mathbf{u}}}{c_s^2} \right) \right. \\ \left. + \delta t \left(\frac{(\mathbf{c}_i \cdot \nabla)(\mathbf{c}_i \cdot \mathbf{u})}{c_s^2} - \nabla \cdot \mathbf{u} + \frac{\mathbf{c}_i \cdot \mathbf{g}}{c_s^2} \right) \right] \end{cases} \quad (3.5)$$

A reversible filter matrix E_{ik} can be introduced to transform this distribution function to moment space α . The distribution then takes the form of

$$f_i \left(\mathbf{x} \pm \frac{\mathbf{c}_i \delta t}{2}, t \pm \frac{\delta t}{2} \right) = \sum_k w_i E_{ik} \alpha_k^\pm(\mathbf{x}) \quad (3.6)$$

with $\omega_i E_{ik} = E_{ki}^{-1}$ and the moment space represented by:

$$\alpha_k^\pm = \sum_i E_{ki} f_i \left(\mathbf{x} \pm \frac{\mathbf{c}_i \delta t}{2}, t \pm \frac{\delta t}{2} \right) \quad (3.7)$$

Due to the 3 dimensional nature of turbulent flow, this thesis uses the D3Q19 scheme of the FM-LBM. As described by Zhuo and Zhong [88] the filter matrix E_{ik} can be chosen as

$$E_{ki} = \begin{bmatrix} 1, c_{ix}, c_{iy}, c_{iz}, 3c_{ix}^2 - 1, 3c_{iy}^2 - 1, 3c_{iz}^2 - 1, 3c_{iy}c_{iz}, 3c_{ix}c_{iz}, \\ 3c_{ix}c_{iy}, 3c_{ix}(c_{iy}^2 - c_{iz}^2), 3c_{iy}(c_{iz}^2 - c_{ix}^2), 3c_{iz}(c_{ix}^2 - c_{iy}^2), \\ c_{ix}(3c_{iy}^2 + 3c_{iz}^2 - 2), c_{iy}(3c_{ix}^2 + 3c_{iz}^2 - 2), \\ c_{iz}(3c_{ix}^2 + 3c_{iy}^2 - 2), 3(2c_{ix}^2 - c_{iy}^2 - c_{iz}^2)(|c_i|^2 - 1.5) \\ 3(c_{iy}^2 - c_{iz}^2)(|c_i|^2 - 1.5), 3|c_i|^2(|c_i|^2 - 2) + 1 \end{bmatrix}^T \quad (3.8)$$

and by using equations (3.8) and (3.5) the moment vectors can be expressed as:

$$\alpha_k^\pm = \begin{bmatrix} \rho \\ \rho u_x \pm \delta t F_x / 2 \\ \rho u_y \pm \delta t F_y / 2 \\ \rho u_z \pm \delta t F_z / 2 \\ 3\rho u_x^2 + \rho(-6v \pm \delta t) \partial_x u_x + (2 - 3B) \rho v \nabla \cdot \mathbf{u} \\ 3\rho u_y^2 + \rho(-6v \pm \delta t) \partial_y u_y + (2 - 3B) \rho v \nabla \cdot \mathbf{u} \\ 3\rho u_z^2 + \rho(-6v \pm \delta t) \partial_z u_z + (2 - 3B) \rho v \nabla \cdot \mathbf{u} \\ 3\rho u_y u_z + \rho(-3v \pm 0.5\delta t) (\partial_y u_z + \partial_z u_y) \\ 3\rho u_x u_z + \rho(-3v \pm 0.5\delta t) (\partial_x u_z + \partial_z u_x) \\ 3\rho u_x u_y + \rho(-3v \pm 0.5\delta t) (\partial_x u_y + \partial_y u_x) \\ 0, k = 10, \dots, 15 \\ 0, k = 16, 17, 18 \end{bmatrix} \quad (3.9)$$

The α_{10-15}^\pm terms represent the six third higher order terms and can be applied with a free parameter ϑ_1 via $\alpha_{10-15}^+ = -\vartheta_1 \alpha_{10-15}^-$. The three fourth higher-order terms α_{10-15}^\pm can be applied in the same way using the free parameter ϑ_2 . To increase numerical stability, the same free parameters $B = 3$, $\vartheta_1 = 0.8$, and $\vartheta_2 = 0.95$ are chosen as in the turbulent simulation work done in [88].

3.2. Boundary Conditions

The computational domain in which the turbulent non-Newtonian fluid flow will be simulated is represented by a rectangular channel shown in figure 3.1. The domain is bounded by periodic boundary conditions in the span and streamwise directions and a no-slip boundary at the top and bottom of the channel. This wall-bounded flow can represent either the anode or cathode of an SSFB when the height of the electrode $2H_{phy}$ is much smaller than the length L_{phy} and width W_{phy} of the electrode. In this case, it can be assumed that the inlet and electrode walls in the stream direction x and the span direction y have very little effect on the total stream profile inside the SSFB. The current collector and membrane, representing the top and bottom of the electrode, are assumed to be flat parallel plates. Therefore, the surface roughness of both materials is not taken into account.

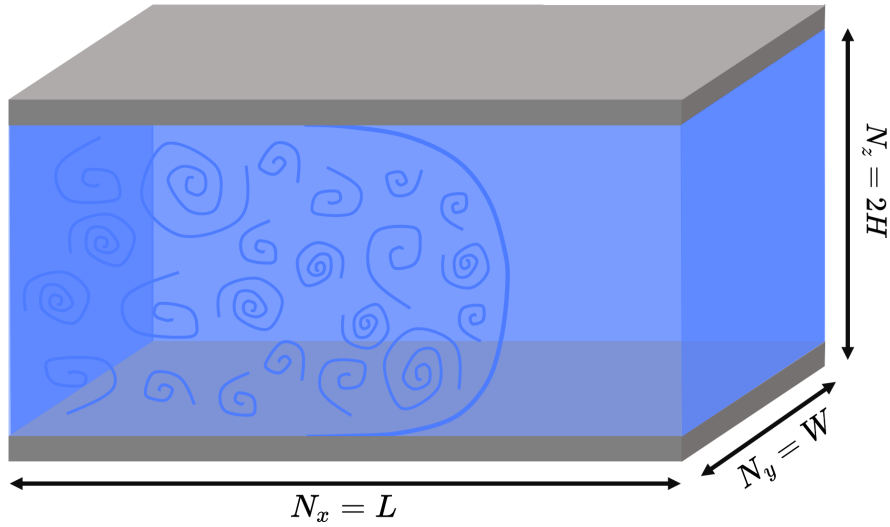


Figure 3.1: Computational domain with periodic boundary conditions in the stream- and span-wise directions and a no slip boundary condition at the parallel plates.

No Slip Boundary Condition

The no slip velocity boundary condition is applied to set the fluid velocity to zero at the walls. In the lattice Boltzmann method, the bounce back method is commonly used for implementing this condition [69]. This method reverses the velocities of particles that collide with the wall, causing them to be reflected back to their original node. The wall is typically positioned halfway between two lattice nodes.

There are two approaches to the bounce back method: the full-way and the halfway bounce back methods. The full-way method reflects populations directed at the wall to nodes inside the wall and reverses their directions in the next collision step, which takes two time steps and is first order accurate [42]. In the halfway method, particles are assumed to hit the wall halfway through the streaming step, their directions are immediately reversed, and the streaming step is completed. This method is second-order accurate [42].

In this research, the halfway bounce back method was preferred because of its higher accuracy. This method is represented with the dark gray arrows in Figure 3.2.

Periodic Boundary Condition

The periodic boundary conditions, applied in this research, represent the domain that extends to infinity in the span and stream directions. However, due to the periodicity of the domain, it is important that the computational domain is large enough to not effect the turbulence in an unphysical manner. To this end, the computational domain must encompass the large-scale turbulent structures. The implementation of the periodic boundary condition is represented in the light gray arrows in figure 3.2.

3.3. Initialisation

To study the turbulent characteristics of non-Newtonian turbulence inside a SSFB, the simulation is initiated in such a way to that it creates the desired chaotic turbulent characteristics in a sustained matter. To this end, two things need to be done. First, a body force and viscosity characteristic are chosen in such a way as to obtain the desired statistical characteristics represented by the Reynolds number of general wall shear stress Re_τ^G . Second, a random fluctuating initial velocity field is chosen to induce a turbulent field that is lasting. These two steps will be elaborated on in this section.

Parameter Input

First the choice of the body force and viscosity field is elaborated on. The most important factor in this choice is the numerical stability limits that restrict the maximum velocity U_{max} . For the BGK method, theoretical stability analysis results in a maximum lattice velocity of $U_{max} \approx \frac{1}{2} \frac{\delta x}{\delta t}$ [42], where practical stability lies well below this value [15]. The practical stability limit for the FM-LBM is less well documented. When considering turbulent channel flow simulations, previous research has found that for an

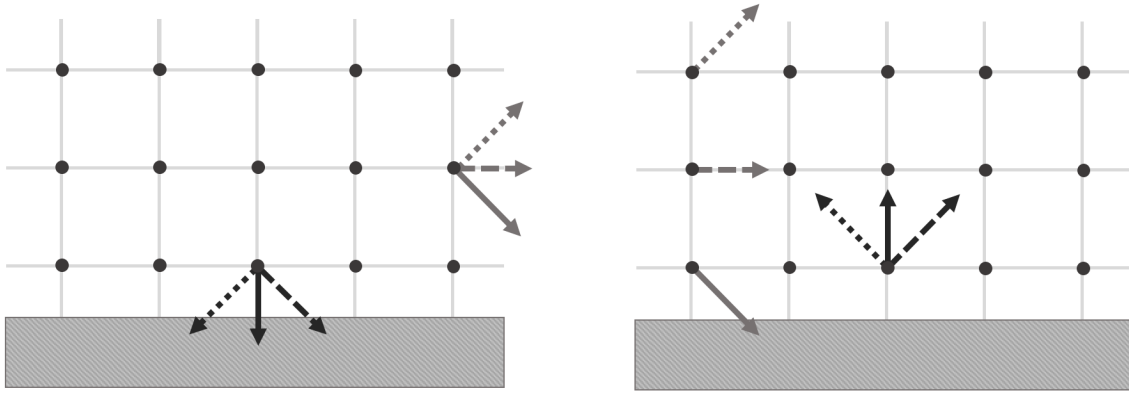


Figure 3.2: Halfway bounceback and periodic boundary conditions for the no slip wall boundary conditions and the stream and span-wise periodic boundary conditions.

average maximum velocity of $\bar{u}_{max} \leq 0.13 [ls\ lt^{-1}]$ the simulation remains stable [69][88]. Using this \bar{u}_{max} and a desired Re_τ^G and power index n one can obtain the grid dimensions \mathcal{D} , body force g and consistency index K following the next steps:

1. Determine \bar{u}_{max}^+ either from known turbulent simulation data or from the known analytical solution in the laminar regime.
2. Use \bar{u}_{max}^+ and the known stability constraint \bar{u}_{max} to obtain u_τ using formula (2.45).
(Simulation tip) Note that we want to take u_τ as high as possible since this increases t^+ and, consequently, decreases the number of simulation steps needed to obtain the desired turbulent statistics.
3. In theory, the dimension of the grid $\mathcal{D} = (N_x, N_y, N_z)$ should now be determined from the Reynolds number using the approximation given by equation (2.32). However, in practice, the domain is chosen with memory constraints in mind, as will be extensively discussed in the results chapter 6.
4. Using the chosen \mathcal{D} and with that $H = \frac{1}{2}N_z$ one can now determine g from u_τ using the definition of u_τ (2.41) combined with the known expression of t_w (2.44).
5. Using the desired Re_τ^G for a given n one can obtain the consistency index K from equation (2.43).

$$\frac{K}{\rho} = \left(\frac{1}{Re_\tau^G} \right)^n \left(\frac{H^{n+2}}{g^{n-2}} \right)^{\frac{1}{2}} \quad (3.10)$$

where $K/\rho = \nu$ for $n = 1$.

These steps result in all the input parameters needed for the turbulent non-Newtonian simulation.

Induced Turbulence

To create the sustained turbulent flow characteristics given the input parameters, random fluctuations must be induced. To this end, there are two possible routes. Either a distribution function f_i^{start} with known turbulent channel flow characteristics is used or a fluctuating velocity together with a viscosity and density field is used to create f_i^{start} . The second method will be discussed here.

To build the initial velocity field, first a laminar parabolic flow field is taken with $U_{max} = 0.12 [ls\ lt^{-1}]$. To this flow field, divergence free random fluctuations are added, in the form of a sum of sine waves with random frequencies. An upper limit of these frequencies is defined, such that the velocity derivatives over the initial velocity field do not become too high. This results in a damping effect on the turbulence and therefore a reduced chance of inducing sustained turbulence. In practice, an upper limit of the frequency is defined as $a_{max}2\pi/N_i$ with $a_{max} = 50$.

The initial velocity field, together with the density and viscosity field, is used to first derive α_k^- using (3.9). This is then in turn used to derive the initial distribution function $f_i^- = f_i^{start}$ using equation (3.6).

3.4. Turbulent Statistics Implementation

The turbulent fluid flow simulation consists of three distinct phases. First, the simulation is initialized, as discussed above. Subsequently, the simulation progresses towards a statistically converged state, and finally, the statistical quantities of the flow are determined. The process of obtaining the statistical quantities, which are discussed in Section 2.5.3, is explained first. This knowledge is then applied to describe the statistical convergence phase.

Mean and Root Mean Square Implementation

Firstly the method behind obtaining the statistical data will shortly be discussed. The foundation of all turbulent statistics lies in the calculation of average values and Root Mean Square (RMS) fluctuations. When the simulated turbulence is statistically converged, this average is obtained by average over space and time. Therefore, this average resembles the assembled average [59].

Specifically, the average of a observable λ , for example the streamwise velocity u or shear rate $\dot{\gamma}$, is calculated via

$$\bar{\lambda}(z) = \frac{1}{N_p N_x N_y} \sum_{t_s=t_{p_0}}^{N_p} \sum_{x=0}^{N_x} \sum_{y=0}^{N_y} \lambda(x, y, z, \Delta t_p t_s) \quad (3.11)$$

with N_p representing the number of times the observable field is saved over time, t_{p_0} the simulation time step of the first saved field and Δt_p the number simulation steps between each save. The RMS fluctuation of an observable λ is very similarly computed via

$$\lambda'_{RMS}(z) = \sqrt{\frac{1}{N_p N_x N_y} \sum_{t_s=t_{p_0}}^{N_p} \sum_{x=0}^{N_x} \sum_{y=0}^{N_y} [\lambda(x, y, z, \Delta t_p t_s) - \bar{\lambda}(z)]^2} \quad (3.12)$$

with $\bar{\lambda}$ the average of the observable. In all the simulations presented in this study $N_p = 80$ and $\Delta t_p = 10000$.

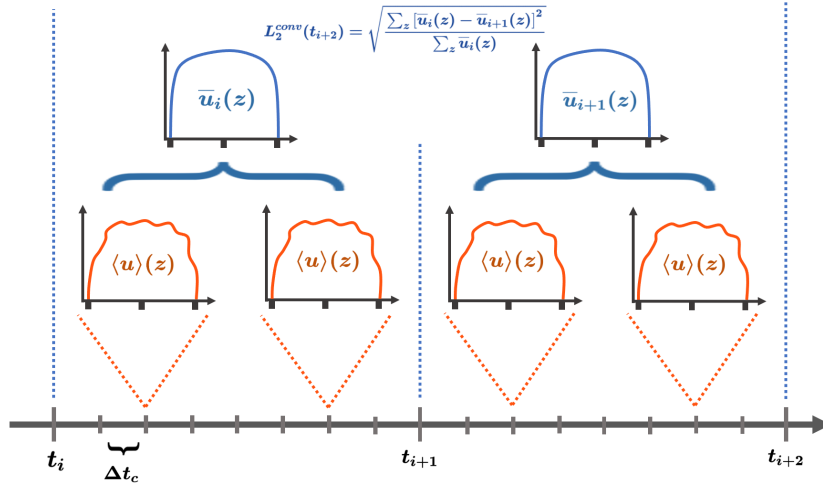


Figure 3.3: Schematic depiction of the statistical convergence check implemented in this study using the L_2^{conv} error norm represented in equation (3.13).

Statistical Convergence Implementation

To determine the simulation time t_{conv} after which the simulation exhibits statistically converged turbulence, the L_2 error norm is used [42]. Specifically, the L_2 error norm is used in this research to compare the average stream-wise velocity profile $\bar{u}_i(z)$ with another stream-wise velocity $\bar{u}_{i+1}(z)$, obtained from data later in time. If the simulation is statistically converged, the average velocity profiles $\bar{u}_i(z)$ and $\bar{u}_{i+1}(z)$ will be the same, and the convergence error norm L_2^{conv} will go to zero.

The averaged velocities are obtained using equation (3.11) with $N_p = N_c$ and $\Delta t_p = \Delta t_c$. The convergence error norm can therefore be defined as

$$L_2^{conv}(t_{i+2}) := \sqrt{\frac{\sum_z [\bar{u}_i(z, t_i \rightarrow t_{i+1}) - \bar{u}_{i+1}(z, t_{i+1} \rightarrow t_{i+2})]^2}{\sum_z \bar{u}_{i+1}^2(z)}} \quad (3.13)$$

where $t_{i+1} = t_i + N_c \Delta t_c$. This is also schematically depicted in figure 3.3.

3.5. GPU Implementation

In this research, the programming language Python is chosen because of its large user base, producing a vast amount of documentation, making the implementation of the code easier. However, Python, being a high-level language, is very slow compared to compiled languages like C++ and FORTRAN. To achieve the computational speed needed for the DNS simulations required in this study, the NUMBA-CUDA package is used to compile the GPU part of the code to C-CUDA, using just in time compilation (jit), after which it can be read by the GPU [45]. After compilation it is found that the performance of NUMBA-CUDA and C-CUDA are comparable, when implemented correctly [62]. The Python GPU implementation proposed here therefore has the potential to fully make use of the GPU power. To optimize the NUMBA-CUDA implementation of the FM-LBM on the GPU, some important decisions were made. These decisions will be elaborated on here. A full overview of the algorithm, used to simulate the turbulent non-Newtonian fluid flow, will be given in the next section.

Optimizing Threads per Block and Blocks per Grid

The first optimization has to do with optimizing the use of GPU resources. To this end the following optimization was made:

- The threads per block (tpb) and blocks per grid (bpg) orientation is taken as such that the tpb are a multiple of 32. As mentioned, the warp scheduler clusters 32 threads to be executed on the cores of one streaming multiprocessor (SM), and the SM runs one block at a time [19]. Therefore, if the tpb are not a multiple of 32 some cuda cores will remain unoccupied within one warp cycle. Specifically, in this research the tpb is oriented to be $t_{pb} = (N_x, 1, 1)$.

Optimizing Memory Handeling

Due to the large amount of data involved in a LBM simulation, GPU implementations for the LBM usually run into memory bandwidth problems [77][61]. Therefore, the memory access patterns are optimized in the following way's:

- The transmission of data between the CPU and GPU is minimized due to the low memory bandwidth connection between these devise memories. Specifically, data is only sent to the GPU using the call `.to_device()` at the beginning while data is only sent back to the CPU using `.copy_to_host()` for saving scalar data N_p times.
- To optimize the memory use on the GPU, the kernel makes use of register memory where possible. However, to save the moment array of length $N_c=19$ inside the kernel, local memory is used with the call `cuda.local.array(Nc, float32)`. The input `float32` sets the datatype of this array to single precision. This is done for all the variables and array's inside the full simulation. To this end, the numpy array types are specified using `numpy.single`.
- The scalar and distribution values are stored in one-dimensional arrays. As stated by [42] the overhead of C type n-dimensional arrays is badly handled by a GPU compared to 1-dimensional arrays. Therefore, it is faster to store the 3D scalar and 4D distribution data in a 1-dimensional array.
- The data is stored in such a way that consecutive reads from memory read consecutive parts inside the array. This is called memory coalescence and significantly increases the simulation speeds for GPUs [42][21]. To this end, the Array of Structures method or AoS is imitated by placing the N_c velocity distributions next to each other in the array since these velocity distribution values are summed over at every node. Due to the tpb orientation in the streamwise direction, the N_x nodes are clustered next since the threads executing these collision steps are run successively inside a block. To this end, $f(x, y, z, i)$ is represented in a 1-dimensional array as $f(i + N_c x + N_c N_x y + N_c N_x N_y z)$ and a scalar $\lambda(x, y, z)$ is represented as $\lambda(x + N_x y + N_x N_y z)$.

- Optimizing the memory access pattern is more difficult for the stream step, as this step is inherently uncoalesced [28]. Different papers present methods of using shared memory to optimize the memory access pattern of threads inside a block [67][77]. However, these methods create a large overhead in the implementation and reduce the scalability of the final code. Therefore, this research used global memory to store the post-stream distribution function f_i^{post} . To increase the access speed of this slow memory, the pull-in stream method is used over the push-out stream method. Since, as found by [82], reading from uncoalesced memory is faster than writing to uncoalesced memory [21]. The pull-in method is used.

Avoiding Race Conditions

Lastly, to avoid race-conditions when executing the code in parallel on the GPU, the code makes use of kernel synchronization. Within the CUDA API the call `cuda.synchronize()` is used to let the next kernel execution wait before all the threads from the previous kernel are executed.

3.6. FM-LBM GPU Algorithm

The full DNS procedure of the FM-LBM implementation of a body force driven turbulent non-Newtonian flow on the GPU is defined in the following Algorithm. With this algorithm the turbulent flow profile of the CB suspension inside a SSFB will be simulated. A schematic depiction of this algorithm is also found in figure 3.4.

1. **Initialisation** [CPU] Either using a $f_{start} = f_i^-$ from a previous simulation or by following the initialisation steps to build f_i^- in CPU memory.
 - Build initial fluid properties: velocity u_i , velocity derivatives $\partial u_i / \partial x_i$, density ρ and viscosity ν fields from random fluctuations.
 - Build α_k^- using fluid properties and equation (3.9).
 - Build f_i^- from α_k^- using equation (3.6).
2. **Kernel Activation's** [CPU] To activate the Kernels the following steps are taken.
 - Send all the scalar array's holding the fluid properties as well as the distribution array's holding f_i^- , f_i^{post} , f_i^+ to GPU global memory.
 - Define tpb and bpg
 - Invoke the activation of both the Stream and Collide kernel for every simulation time step N_t
3. **Stream Step Kernel** [GPU] To let the neighboring nodes interact with each other the following stream steps are taken per node.
 - Pull in the neighboring distribution functions into the f_i^{post} array in global memory.
 - Apply bounce back and or periodic boundary condition if the node sits on a boundary.

After the Stream Kernel is done working through all the threads, the simulation is synchronised.
4. **Collision Step Kernel** [GPU] The kernel is executed for every point in the computational domain using the tpb and bpg to define its location in memory.
 - a **Pre-collision moment** [GPU] α_k^- is obtained from f_i^- using equation (3.7) where the information of f_i^- is extracted from global memory and α_k^- is stored in local memory.
 - b **Fluid properties extraction** [GPU] From α_k^- and the viscosity of the previous time step, the new kinematic viscosity ν , density ρ and the fluid velocities and their derivatives are extracted using equation (3.9)
 - Density is obtained from α_0^-
 - Velocity components are extracted from α_{1-3}^-
 - Velocity divergence components are extracted from α_{4-6}^- and cross derivatives are extracted from α_{6-9}^- .
 - Using the velocity derivatives the shear rate $\dot{\gamma}$ is derived using equation (2.29)
 - With $\dot{\gamma}$ the viscosity is determined and updated in global memory
 - c **Post-collision moment** [GPU] Using the fluid properties and α_k^- the post-collision moment vector α_k^+ is built according to (3.9) and saved in the local memory of α_k^- .

- d **Post-collision distribution** [GPU] Using equation (3.6) the post-collision distribution f_i^+ is updated in global memory.
5. **Convergence Check** [GPU/CPU] Running steps 3 and 4 until the simulation is statistically converged, which is checked using the L_2^{conv} error norm (3.13).
- [GPU] Add the streamwise velocity profile u from register memory to the global array u_{sum} every Δt_c simulation time steps.
 - [GPU] When the velocity profiles are summed up N_c times, the u_{sum} array is sent from global to CPU memory.
 - [CPU] The average velocity profile $\bar{u}_{i+1}(z)$ is made from u_{sum} using equation (3.11).
 - [CPU] The L_2^{conv} is determined using $\bar{u}_{i+1}(z)$ and the average velocity $\bar{u}_i(z)$ determined $N_c \Delta t_c$ time steps back using equation (3.13).
 - [CPU] Average velocity is saved to CPU memory to be used for next L_2^{conv} calculation.
6. **Data Save** [GPU/CPU] After the simulation is statistically converged (t_{p0}) steps 3 and 4 are repeated to obtain the statistical data. To this end the fluid properties are saved N_p times to a binary file once every Δt_p simulation time steps.
- [GPU] Load the fluid properties from register memory to global memory.
 - [GPU] Synchronise the kernel such to make sure all the threads have updated the scalar array in global memory.
 - [GPU] Send the filled scalar array's to the CPU ram memory.
 - [CPU] Save the scalar array in a binary file on the host hard drive.

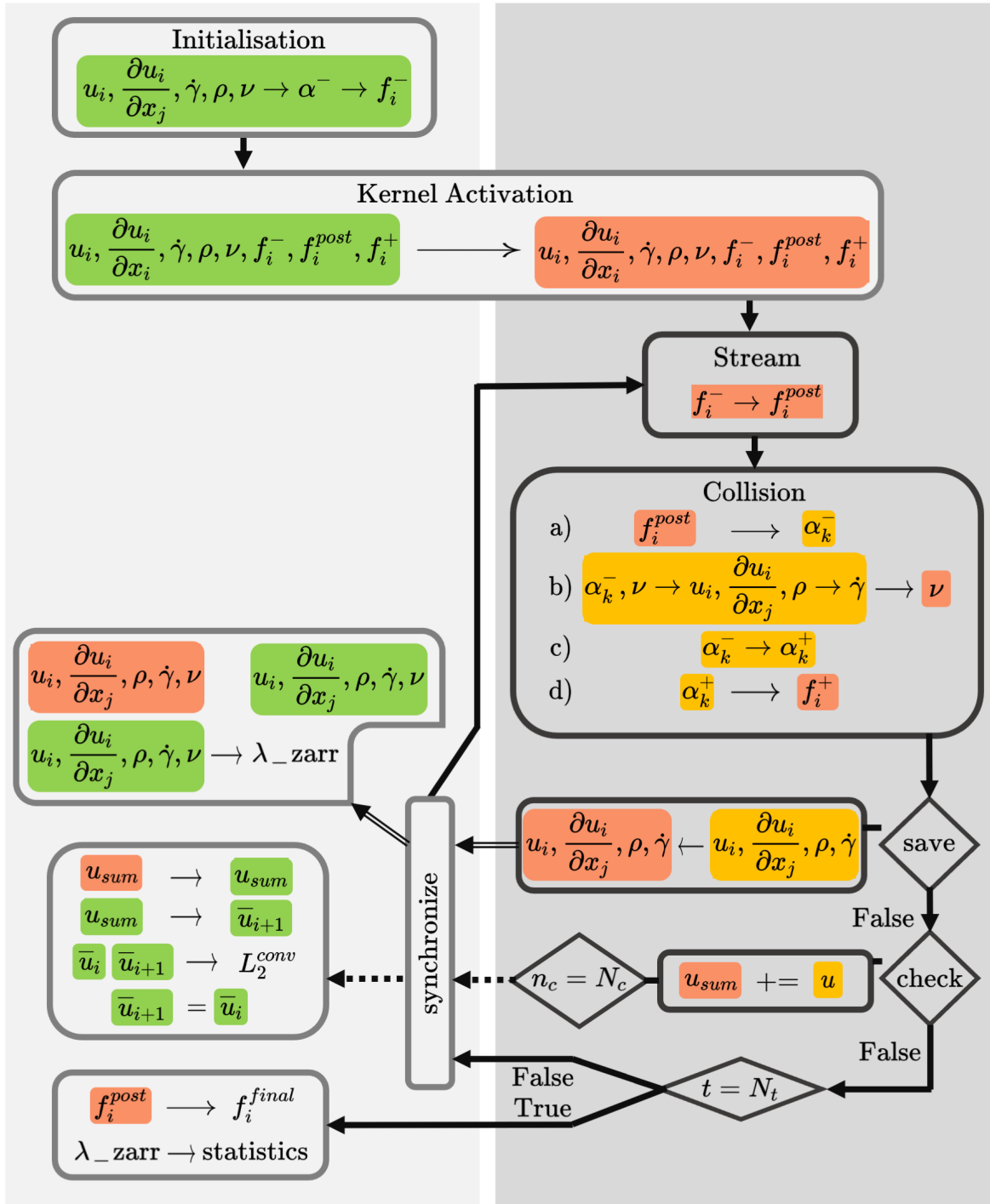


Figure 3.4: Algorithm for the FM-LBM implementation on a GPU. CPU-memory is represented in green, Global-memory is represented in red and Local/Register-memory is represented in orange

4

Electric Potential Model

This chapter is devoted to the implementation of the model describing the electric potential inside the Carbon Black suspension flowing through a SSFB. As described in section 2.1.5 the electric potential equation (2.11) takes the form of a conservation law. The Finite Volume Method (FVM) is a well-established technique used to solve differential equations related to conservation laws in various fields such as fluid dynamics, heat transfer, and electromagnetics. Therefore, this research will use the FVM to solve the electric potential to determine the total internal resistance and effective conductivity inside an SSFB. Specifically, the 2D method developed by Peters will be extended to 3D to incorporate the 3D effects of turbulence [64].

In this chapter, we will elaborate on how the FVM is used to solve the potential equation inside an SSFB under equilibrium conditions. First, section 4.1 will describe how the governing conservation law is rewritten to Finite Volume form and discretized in 3D. Then, section 4.2 will discuss the geometry and how the boundary conditions are implemented. How this system of equations is converted to matrix form and solved is then discussed in section 4.3. Finally, section 4.4 describes how the internal resistance is obtained from the electric potential.

4.1. Finite Volume Discretization

With finite volume models, the computational domain is divided into contiguous, non-overlapping volume elements. Differential equations are integrated over each control volume and then converted to surface integrals using the divergence theorem to calculate the flow of the integrand through the surface of the control volume. The flux emerging from a control volume is equal to the flux entering its adjacent control volumes, creating a system of interdependent equations [27].

Applying the divergence theorem on the potential equation one obtains

$$\iiint_{\Omega} \nabla \cdot \sigma \nabla \Phi d^3 r = \iint_{\partial\Omega} \sigma \nabla \Phi \cdot \hat{n} dA = \iint_{\partial\Omega} \mathbf{J} \cdot \hat{n} dA = \iint_{\partial\Omega} \frac{\partial \rho_c}{\partial t} \cdot \hat{n} dA = 0 \quad (4.1)$$

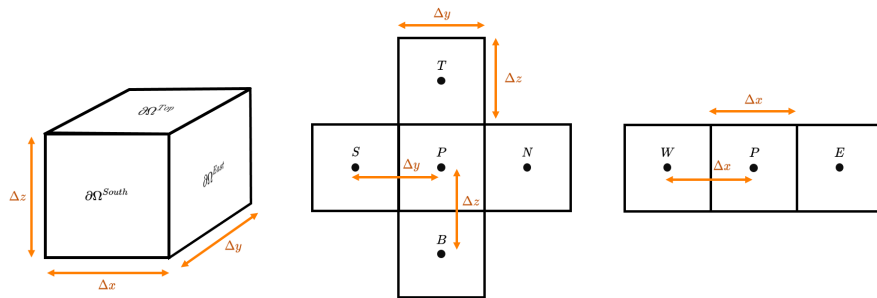


Figure 4.1: Figure shows the cuboidal finite volume element for discretization of the potential equation (left). It also shows the neighboring volume elements are oriented w.r.t. the central element represented by P .

where Ω represents a volume element. The meaning behind this charge conservation equation is that if a closed surface does not enclose any current source ($\partial\rho_c/\partial t = 0$), the sum of the currents passing through that surface will be zero [32].

If one takes a cuboidal volume elements (Figure 4.1), the above mentioned surface integral can be rewritten to a sum of 6 surface integrals integrating the potential gradient over the faces of the cube. Equation (4.1) can in that case be rewritten as

$$\begin{aligned} 0 = & \iint_{\partial\Omega_{East}} \sigma \frac{\partial\Phi}{\partial x} dydz - \iint_{\partial\Omega_{West}} \sigma \frac{\partial\Phi}{\partial x} dydz \\ & + \iint_{\partial\Omega_{North}} \sigma \frac{\partial\Phi}{\partial y} dx dz - \iint_{\partial\Omega_{South}} \sigma \frac{\partial\Phi}{\partial y} dx dz \\ & + \iint_{\partial\Omega_{Top}} \sigma \frac{\partial\Phi}{\partial z} dx dy - \iint_{\partial\Omega_{Bottom}} \sigma \frac{\partial\Phi}{\partial z} dx dy \end{aligned} \quad (4.2)$$

where every element represents the electric current flowing through the respective surface of the finite volume element.

For the discretization, the gradient of the electric potential is approximated on the surface using the central difference method. Since the information of σ is also stored in the center of the finite volume its value at the surface of the element also needs to be approximated. To do so, linear interpolation is used. As an example, the east surface element of a volume element is expanded. In the example, P represents the internal point and the W its west neighboring volume element. The discretization of this surface element becomes

$$\iint_{\partial\Omega_{West}} \sigma \frac{\partial\Phi}{\partial x} dydz = - \int_b^t \int_s^n \sigma(\mathbf{x}_w) \frac{\partial\Phi(\mathbf{x}_w)}{\partial x} dydz = \frac{\sigma(\mathbf{x}_P) + \sigma(\mathbf{x}_W)}{2} \frac{\Phi(\mathbf{x}_W) - \Phi(\mathbf{x}_P)}{\Delta x} \Delta y \Delta z + \mathcal{O}(\Delta x^2) \quad (4.3)$$

where the lower case characters represent the position at the respective boundary of the volume element. In this derivation the volume elements are assumed to be equally sized, since this choice is made in the rest of this research. The order of accuracy results from the truncation error that originates from the central difference method [27].

Apart from this choice and the choice of a square volume element, this discretization is fully general. How it is implemented in the domain representing a SSFB is discussed in the next section.

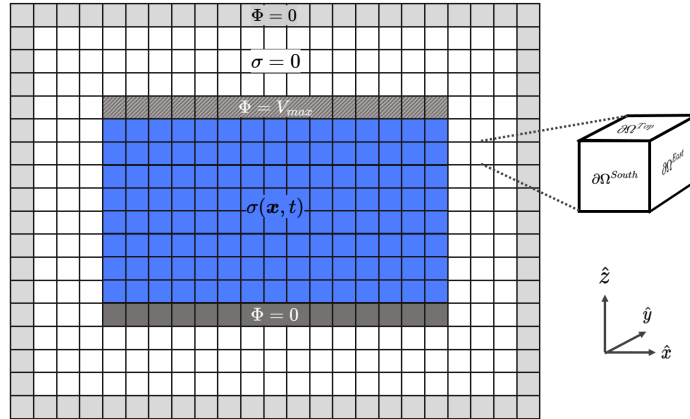


Figure 4.2: The flow channel and surrounding domain discretized using the finite volume method with equally sized volume elements.

4.2. Geometry and Boundary Conditions

This section will discuss the geometry and subsequent boundary conditions used to solve the potential field in a SSFB. As discussed in section 2.1.5, the assumption is made that all the reactions take place near the membrane. The flow channel can therefore be seen as a cuboidal conductor with variable

conductivity $\sigma(\mathbf{x}, t)$. The flow profile in the anode and the cathode is assumed to be the same, making the $\sigma(\mathbf{x}, t)$ profile in both half cells the same. As a result, the internal potential field Φ will also be equal up to a minus sign. Therefore, only one cell will be considered and the external potential will be applied over the conducting plate located at the top representing the current collector and a insulator plate at the bottom representing the membrane. Since the potential will not be zero around the cuboidal conductor, a surrounding medium is added to close the system of equations. A schematic 2D representation of the computational domain is found in figure 4.2. In the figure four distinct regions are found:

- **Flow channel (blue):** This region represents the flow channel where the turbulent LBM simulation generates a shear rate profile ($\dot{\gamma}_{LBM}$) which results in a spatial conductivity profile $\sigma = \sigma(\dot{\gamma}_{LBM}(\mathbf{x}))$.
- **Parallel plates (dark gray):** The top plate represents the membrane where the reactions take place, resulting in $\Phi = V_{max}$ and the bottom plate represents the cathodic current collector set to zero potential $\Phi = 0$. The potential difference is therefore $\Delta V = V_{max}$. The height or thickness of the plate is defined by T_{plate} .
- **Surrounding medium (white):** In this region the conductivity is set to a small value $\sigma \rightarrow 0$ to ensure that all current flows from the membrane through the channel to the current collector. The thickness of the surrounding medium is defined as T_{sur} . The number of volume elements in every direction N_{sur} will remain constant making $\frac{T_{sur}}{\Delta x} = \frac{T_{sur}}{\Delta y} = \frac{T_{sur}}{\Delta z}$.
- **Boundary (light gray):** The potential at the boundary is set to zero ($\Phi = V_{boundary} = 0$). In reality, the electric potential approaches zero at $T_{sur} \rightarrow \infty$. However, for large channel dimensions, the edges of the channel have a small contribution to the total potential inside the channel. Therefore, the solution will remain accurate for a relatively small numbers T_{sur} .

To discretize the domain, the cuboidal volume elements will have dimensions equal to $\Delta x = \frac{N_x}{L}$, $\Delta y = \frac{N_y}{W}$ and $\Delta z = \frac{N_z}{2H}$ where L , W , H represent the flow channel length, width and half height, respectively. The dimensions of the channel (N_x, N_y, N_z) are determined by the LBM turbulent flow simulations. The entire computational domain will have dimension (N_i, N_j, N_k) that includes the thickness of the plates and the surrounding medium. Indices i, j and k will represent the Cartesian coordinates x, y, z respectively.

At the domain boundary or at the boundary of the parallel plates, the Dirichlet boundary condition is used. In this case the potential gradient from equation (4.2) at the finite volume face neighboring the boundary is approximated using either the forward or backward difference method. The conductivity at this surface is not interpolated but chosen to be equal to that of the internal volume point, since the conductivity outside the boundary is not defined. If the same example is chosen as in the previous section but with the west neighbor W being a domain boundary node the discretization becomes

$$\iint_{\partial\Omega_{West}} \sigma \frac{\partial\Phi}{\partial x} dydz = - \int_b^t \int_s^n \sigma(\mathbf{x}_w) \frac{\partial\Phi(\mathbf{x}_w)}{\partial x} dydz = \sigma(\mathbf{x}_P) \frac{V_{boundary} - \Phi(\mathbf{x}_P)}{\Delta x/2} \Delta y \Delta z + \mathcal{O}(\Delta x) \quad (4.4)$$

where the order of accuracy results from the truncation error that originates from the forward or backwards difference method [27]. The total discretization of this node then becomes

$$\begin{aligned} 0 = & \frac{\sigma_{i,j,k} + \sigma_{i+1,j,k}}{2} \frac{\Phi_{i+1,j,k} - \Phi_{i,j,k}}{\Delta x} \Delta y \Delta z + \sigma_{i,j,k} \frac{V_{boundary} - \Phi_{i,j,k}}{\Delta x/2} \Delta y \Delta z \\ & + \frac{\sigma_{i,j,k} + \sigma_{i,j+1,k}}{2} \frac{\Phi_{i,j+1,k} - \Phi_{i,j,k}}{\Delta y} \Delta x \Delta z + \frac{\sigma_{i,j,k} + \sigma_{i,j-1,k}}{2} \frac{\Phi_{i,j-1,k} - \Phi_{i,j,k}}{\Delta y} \Delta x \Delta z \\ & + \frac{\sigma_{i,j,k} + \sigma_{i,j,k+1}}{2} \frac{\Phi_{i,j,k+1} - \Phi_{i,j,k}}{\Delta z} \Delta x \Delta y + \frac{\sigma_{i,j,k} + \sigma_{i,j,k-1}}{2} \frac{\Phi_{i,j,k-1} - \Phi_{i,j,k}}{\Delta z} \Delta x \Delta y \end{aligned} \quad (4.5)$$

Now we know how and where potential equation is discretized, the next section will elaborate on the solution method for the system of linear equations.

4.3. Solution Method

For each cuboidal volume element the integral over the 6 faces described by (4.2) can be discretized using equations (4.3) and (4.4) for, respectively, an internal and boundary neighbor. Since this equation

is linked to its six neighboring elements due to their shared boundary surface, the equations form a system of linear equations. This system can be written in the form a matrix equation

$$\mathbf{M}U = \mathbf{b} \quad (4.6)$$

where \mathbf{M} represents a square matrix of size $(N_i N_j N_k) \times (N_i N_j N_k)$ and U and \mathbf{b} represent vectors of length $(N_i N_j N_k)$. U is defined as such that $U(i N_j N_k + j N_k + k)$ represents $\Phi(i, j, k)$.

The equation for every volume element is translated into six components of \mathbf{M} and one component of \mathbf{b} . As an example equation (4.5) will be converted to matrix form resulting in the next entry's

$$\begin{aligned} \mathbf{M}(i N_j N_k + j N_k + k; i N_j N_k + j N_k + (\mathbf{k} + 1)) &= t = \frac{\sigma_{i,j,k} + \sigma_{i,j,k+1}}{2} \frac{\Delta x \Delta y}{\Delta z} \\ \mathbf{M}(i N_j N_k + j N_k + k; i N_j N_k + j N_k + (\mathbf{k} - 1)) &= b = \frac{\sigma_{i,j,k} + \sigma_{i,j,k-1}}{2} \frac{\Delta x \Delta y}{\Delta z} \\ \mathbf{M}(i N_j N_k + j N_k + k; i N_j N_k + (\mathbf{j} + 1) N_k + k) &= n = \frac{\sigma_{i,j,k} + \sigma_{i,j+1,k}}{2} \frac{\Delta x \Delta z}{\Delta y} \\ \mathbf{M}(i N_j N_k + j N_k + k; i N_j N_k + (\mathbf{j} - 1) N_k + k) &= s = \frac{\sigma_{i,j,k} + \sigma_{i,j-1,k}}{2} \frac{\Delta x \Delta z}{\Delta y} \\ \mathbf{M}(i N_j N_k + j N_k + k; (\mathbf{i} + 1) N_j N_k + j N_k + k) &= e = \frac{\sigma_{i,j,k} + \sigma_{i+1,j,k}}{2} \frac{\Delta y \Delta z}{\Delta x} \\ \mathbf{M}(i N_j N_k + j N_k + k; i N_j N_k + j N_k + k) &= - \left(t + b + s + w + e + \sigma_{i,j,k} \frac{2 \Delta y \Delta z}{\Delta x} \right) \\ \mathbf{b}(i N_j N_k + j N_k + k) &= -V_{\text{boundary}} + \sigma_{i,j,k} \frac{2 \Delta y \Delta z}{\Delta x} \end{aligned} \quad (4.7)$$

This method generates a non-Singular banded matrix \mathbf{M} . For which the solution vector U represents the potential field.

To solve the system of equations, package `pyamg` is used. Specifically, `pyamg` implementation of the Ruge-Stuben applied multigrid (AMG) method is used [6]. This choice is made due to its ability to solve large-scale linear systems with optimal performance whilst not requiring any information about the structure of the matrix.

4.4. Electric Field and Resistance

Using the potential field derived from solving the linear set of equations, the total internal resistance and effective conductivity of the CB suspension inside a SSFB can be calculated. From Ohms law it can be seen that the flux through every face of the volume element is equal to the current flowing from one volume to the other. The current flowing through the top of a volume element can therefore be discretized via

$$j_z(\mathbf{x}_t) = - \left(\frac{\sigma_{i,j,k-1} + \sigma_{i,j,k}}{2} \right) \left(\frac{\Phi_{i,j,k} - \Phi_{i,j,k-1}}{\Delta z} \right) \Delta x \Delta y \quad (4.8)$$

where \mathbf{x}_t is the location of the interface between the volume elements.

Since there is no charge generated inside the channel and the charge is conserved, the net current flowing through the channel is constant. This means that the total current I can be computed by summing up the current density's j_z between any contour in between the two parallel plates. The total resistance R_{tot} can then be easily computed using the potential difference between the parallel plates ΔV . Using Pouillet's law (2.14) the effective conductivity can then easily be computed with A the area of the parallel plates defined as $A = L \cdot W$

5

Validation and Turbulent Flow Results

The goal of this research is subdivided into two parts. The first part has the goal of correctly simulating the turbulent flow profile of a shear-thinning fluid. The second part will use the data from these turbulent simulations to determine conductivity of the carbon black suspension, after which the electrical resistance will be determined by computing the potential inside the SSFB. This chapter will focus on the first part where the non-Newtonian flow will be simulated using the FM-LBM implemented on a NVIDIA GPU.

Before the proposed simulation method is used to obtain the turbulent non-Newtonian channel flow characteristics, this chapter describes how the setup was validated. The validation results of the LBM on the GPU are described in Sections 5.1, 5.2 and 5.3, respectively, dealing with the computational performance, laminar flow, and Newtonian turbulent flow results. After benchmarking the LBM implementation, it is used to simulate turbulent non-Newtonian power-law flow in section 5.4. In section 5.5 the shear rate profiles of the Newtonian and non-Newtonian simulations are analyzed, setting the stage for Chapter 6, in which the conductivity measurements which will make use of these shear rate profiles.

5.1. Parallel Performance GPU

In this study the FMLBM-D3Q19 model was implemented in Python. The code was parallelized using the CUDA programming language such that it could run on a NVIDIA Tesla A100 GPU, facilitated by Delft Blue [1]. The hardware specifications of the GPU used are given in table 5.1. In this section, the performance of this code, used for all other simulations, is elaborated on.

To obtain the computational performance of the current FM-LBM GPU implementation, the simulation speed is tested on a square grid. As a measure of kernel performance, the number of 10^6 grid nodes that are updated per second (MLUPS) is used to compare the data with other LBM GPU implementations. As can be seen in Figure 5.1, the simulation performance plateaus around 350 MLUPS. As expected, the simulation time for a simulation step where all the scalar parameters are stored on CPU memory is approximately 2 times slower.

Since the LBM is constrained by its memory use, the theoretical maximum LUPS can be derived from

$$\text{LUPS} = \frac{\text{BW}_{SDK}}{N_A} \quad (5.1)$$

with BW_{SDK} the memory bandwidth of the GPU, and N_A the number of memory accesses per node [21]. In this research N_A is made up of one read and one write of the $N_c = 19$ distributions for the stream and collide kernel. Additionally, the viscosity array is read from and written to every collision step to enable the non-Newtonian behaviour. Using single precision, every element is made up of 4 bytes, so in total $N_A = 4 \cdot (4 \cdot 19 + 2 \cdot 1) = 312$ bytes for a single node. As found by Delbosc *et al.* [21] and Forslund *et al.* [28] the BW_{SDK} is approximately 70% percent of the theoretical bandwidth of $\text{BW} = 1134 \text{ GB/s}$. Using the maximum theoretical performance derived from equation (5.1) and comparing it to the simulation performance found in Figure 5.1 the bandwidth utilization of this setup equates to 14%. This is significantly lower than the 80% utilization other GPU-LBM implementations find [21][38][28].

Table 5.1: GPU hardware specifications [60], [1]

NVIDIA Tesla V100S	
CUDA cores	5120
dims of grid	$(2^{31}, 2^{16}, 2^{16})$
dims of block	$(2^{10}, 2^{10}, 2^6)$
Number of SM	4
Blocks per SM	32
Threads per SM	2048
Register per SM (K)	64
Shared mem. per block (KiB)	64
Local mem. per thread (KiB)	512
Global memory (Gb)	32
Memory bandwidth (GB/s)	1134

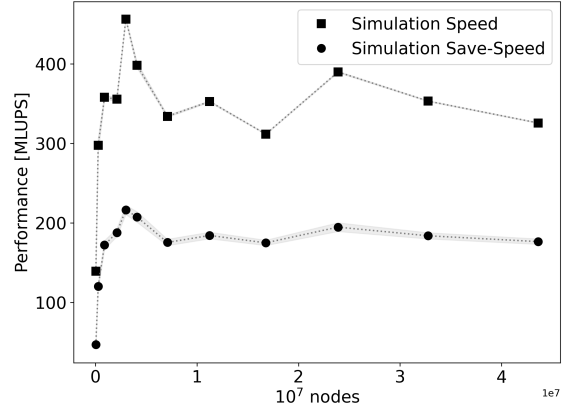


Figure 5.1: FM-LBM GPU implementation performance for a 3D channel of size N^3 nodes, where $N \in [32, 352]$. Performance of a simulation step with and without saving the simulation data is show in million lattice updates per second (MLUPS).

The main difference between the current GPU implementation compared to the more efficient algorithms implemented in [21][38][28] is the use of shared memory in the stream and collision step. As mentioned in section 2.6.3, this significantly improves the speed at which the kernels inside a block can access the neighboring and intrinsic distributions. This therefore explains the low bandwidth utilization of the current algorithm. Further research can implement shared memory use by either writing an MPI-like algorithm [21][38] or using an Open Graphics Library OpenGL [28].

The second disadvantage of the current setup is the implementation of the stream and collision steps in separate kernels. This separation doubles the number of reads from and writes to global memory, resulting in the total number of MLUPS more than halving when compared to an algorithm that combines the stream and collide step in one kernel. Specifically, this combined algorithm achieves a plateau of approximately 900 MLUPS. However, this combined kernel suffered from unresolved race conditions, resulting in a slight asymmetry in the channel flow simulations. This error rendered this implementation ineffective.

Given the low efficiency, the current algorithm is not an optimal LBM GPU implementation. However, the current GPU implementation is around three times faster than the simulation speed found by the FM-LBM implementation reported by Zhuo and Zhong on a 16-core CPU [88]. Given this improvement, which results in a maximum simulation time of approximately 30 hours, the current setup is adequate for the goal of this research.

5.2. Laminar Flow

To determine if the proposed FM-LBM implementation on the GPU constitutes basic physical behavior, the algorithm is first benchmarked in the laminar regime. To this end, the laminar flow simulation of the shear-thinning CB rheology, approximated by the power-law viscosity model, is compared with analytical solutions. This section will discuss these laminar flow results or power-law simulations with decreasing power-law index n .

Analytical Solution

Due to the computational domain with its periodic boundary conditions in the x and y directions, the simulation represents a parallel plate configuration which stretches to infinity in the x and y directions. For this situation, the analytical solution can easily be computed from (2.16) by assuming steady state, fully developed flow in the streamwise direction. For a body force g driven flow this solution takes the form of

$$u_x^a(z) = \left(\frac{n}{n+1} \right) \left(\frac{\rho g}{K} \right)^{\frac{1}{n}} \left(H^{\frac{n+1}{n}} - |H-z|^{\frac{n+1}{n}} \right) \quad (5.2)$$

with the channel half height H . The rheology is represented in the power-law index n and the consistency index K of equation (2.30). Using this equation for the streamwise velocity profile the analytical

solution for the shear rate can be derived from (2.29) via

$$\dot{\gamma}(z) = \sqrt{\left(\frac{\partial u_x}{\partial z}\right)^2} = \frac{g}{K} (|H - z|)^{\frac{1}{n}} \quad (5.3)$$

and with the definition of the power-law (2.30) also the analytical solution for the viscosity ν becomes

$$\nu = \frac{K}{\rho} \left(\frac{g}{K} (|H - z|)^{\frac{1}{n}}\right)^{n-1}. \quad (5.4)$$

Input Parameters and Convergence

To check if the LBM represents shear thinning fluids in a physical way, 5 simulations with decreasing power index n are simulated on the GPU and compared to the analytical solutions mentioned above. These simulations are executed for a Reynolds number equal to $Re_c = 100$ that is well in the laminar range [59] and a domain equal to $D = (5, 5, 128)$. This domain is chosen such to equal the number of wall normal gridpoints N_z that will be used in the turbulent simulations. The consistency index K and stream-wise body force g are chosen in such a manner that $Re_c = 100$ and $U_{max} = u_x^{max} = 0.1 [ls\,lt^{-1}]$ via

$$g = \left(\frac{n+1}{n}\right) \frac{U_{max}^2}{H Re_c} \quad K = \left(\frac{U_{max} H}{Re_c (gH)^{\frac{n-1}{n}}}\right)^n \quad (5.5)$$

where the restriction of maximum lattice speed U_{max} is important since FM-LBM becomes unstable for much higher lattice velocities [42].

Another important input parameter choice is the cut-off viscosity. Since, for shear thinning fluids, the viscosity goes to infinity when $\dot{\gamma} \rightarrow 0$, a choice for ν_{max} needs to be made. Different ν_{max} were tested, and for $\nu_{max} > 20 [ls^2\,lt^{-1}]$ the simulation showed good agreement with the analytical solutions. Therefore, to be safe, the maximum viscosity was set to $\nu_{max} = 50 [ls^2\,lt^{-1}]$ for the remainder of all shear thinning simulations. Another choice of input parameter that remains constant for all other simulations is the lattice density $\rho_0 = 1 [ls^{-3}]$.

The simulations are initiated with zero velocity, after which, driven by the body force, the flow profile transitions to a steady state. To determine whether the simulation converges to this steady state, the L_2^{conv} convergence method is used as stated in section 3.4. Specifically, equation (3.13) is used with $N_c = 1$ and $\Delta t_c = 1 [lt]$ to determine the difference between $u(z, t)$ and $u(z, t + \Delta t)$. The simulation is taken to represent a steady state for $L_2^{conv} \leq 10^{-7}$.

Results and Discussion

Figures 5.2 show the simulation results of the laminar power law simulations with power law indices $n \in [1, 0.7, 0.5, 0.3, 0.1]$. To characterise the total error of the simulated profiles with respect to their respective analytical solutions the L_2 error norm is used in the following form

$$L_2(t) := \sqrt{\frac{\sum_z (\phi_n(z, t) - \phi_a(z, t))^2}{\sum_z \phi_a^2(z, t)}} \quad (5.6)$$

where ϕ is either the velocity, shear rate or viscosity [42]. In Figures 5.2a, 5.2c and 5.2d it can be seen that the converged steady-state simulations match the analytical solutions represented in the dotted lines. Especially the viscosity 5.2c and shear rate 5.2d profiles match their analytical solutions very well with a maximum error $L_2 = 5.5 \cdot 10^{-5}$.

For the stream-wise velocity profiles, the L_2 errors are approximately a factor 10 higher than for the ν and $\dot{\gamma}$ profiles. To further sort out where this deviation comes from, the local error of the analytical solution w.r.t. the simulation is determined via

$$\epsilon_u(z) = \left| \frac{u_n(z) - u_a(z)}{u_a(z)} \right| * 100\% \quad (5.7)$$

for which the results are shown in Figure 5.2b. Two things can be noticed from these errors.

- Firstly, the error increases near the boundary and this effect is larger for lower power indices n . This behavior can be explained by the second-order accuracy of the half-way bounce-back method. Since for a lower n the shear rate increases near the wall, the error also increases. As a result of this error behavior, the velocity profiles u_y and u_z are not zero. These non-zero velocity profiles generate the error in the u_x velocity profile seen in Figure 5.2b. However, since the error is still relatively small and especially the L_2 error norm value speaks of a very good agreement, this wall error is not considered a problem.
- Second, for $n = 0.1$ there is an increased error in the middle of the channel. This can be explained by the cut of viscosity being a bit too low for such a shear-thinning fluid. However, since in further research $n > 0.6$, $\nu_{max} = 50$ is found to be sufficient, as this error only occurs for $n = 0.1$.

In conclusion, the laminar simulations show good agreement with the analytical solutions, especially for $n > 0.6$. For the number of gridpoints chosen, the local error in the velocity profile remains within 1% at the boundary for moderately small $n > 0.6$ and the shear rate and viscosity profiles show even better agreement.

All in all the laminar flow can be regarded as validated. The next sections will be devoted to Newtonian turbulent simulations to further benchmark the numerical setup before it will be used to simulate non-Newtonian flow.

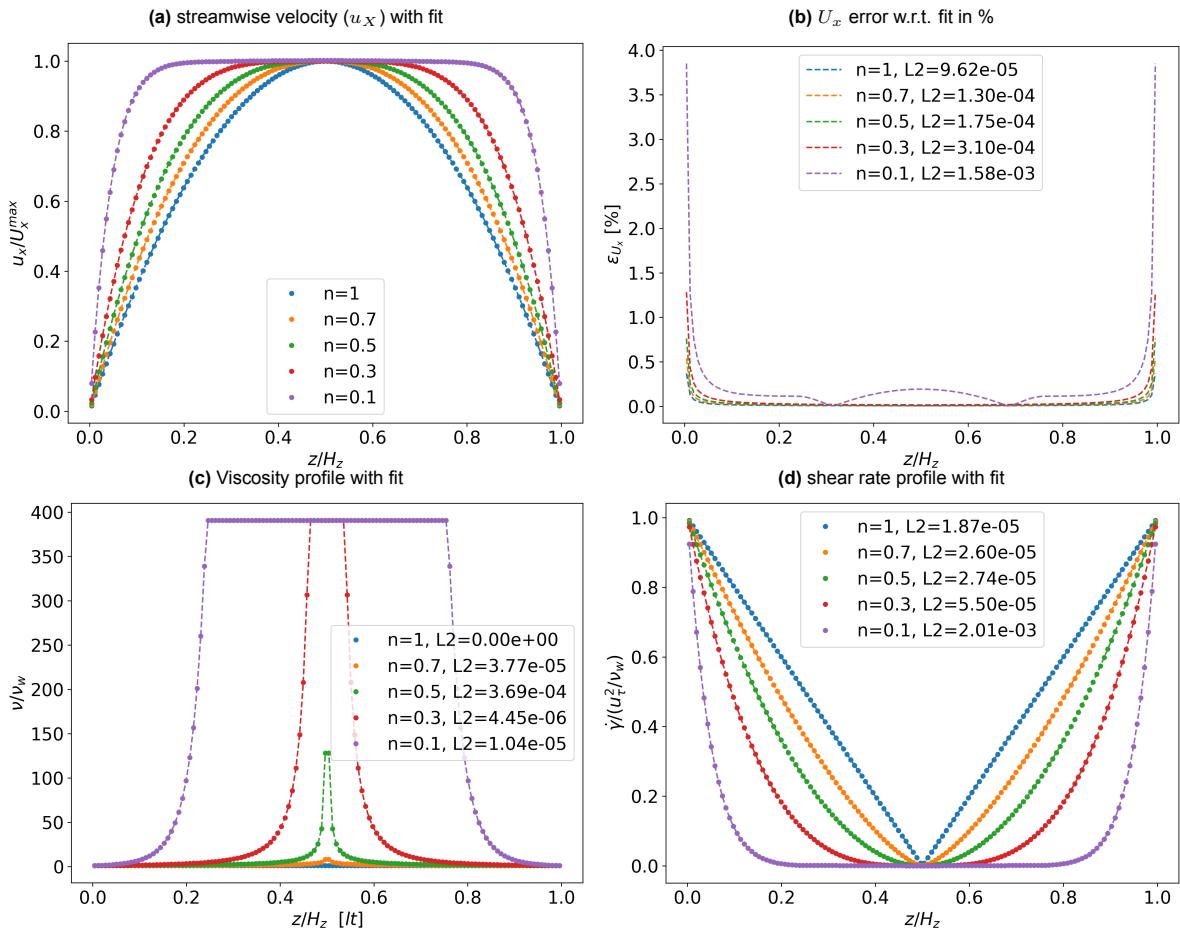


Figure 5.2: Figures show normalised velocity (u) 5.2a, viscosity (ν) 5.2c and shear rate ($\dot{\gamma}$) 5.2d of a laminar flow profile. All data is compared with the analytical solution (5.2) where the L_2 error norm is obtained via (5.6) with t the simulation step after which the simulation is fully converged. The error between the numerical and analytical velocity profile as calculated using (5.7) is shown in 5.2b

5.3. Turbulent Newtonian Flow

To find out if the FB-LBM implemented on the GPU also represents physical behavior in the turbulent regime, the method is benchmarked to known Newtonian turbulent channel flow statistics. This is done for the three different wall shear stress turbulent Reynolds numbers $Re_\tau = \{110, 180, 395\}$ for which the numerical input data can be found in table 5.2. These Reynolds numbers represent transitional, low Re and high Re turbulence, respectively. Eventually, the turbulent non-Newtonian simulations will also be executed in the different turbulent regimes represented by these Reynolds numbers. This will help determine the effects of turbulence on the electrical resistance of a CB suspension inside a SSFB in different turbulent regimes.

First, the results of $Re_\tau = 180$ will be compared to other turbulent LBM simulations in section 5.3.1. Then section 5.3.2 will compare the different Re_τ simulations with each other and with known simulation data using different simulation methods.

Table 5.2: Numerical settings for the turbulent Newtonian channel flows for bench marking against the simulations done by KMM [54] and TS [79]

Re_τ	Re_τ^{out}	Re_m	$N_x \times N_y \times N_z$	u^+	Δz^+	ν	g
110	109.6	1618	512 x 128 x 128	3.636e-3	1.72	2.116e-3	2.07e-7
180	180.2	2795	256 x 128 x 128	6.667e-3	2.8	2.37e-3	6.94e-7
180	180.9	2800	512 x 128 x 128	6.667e-3	2.8	2.37e-3	6.94e-7
395	398.3	7020	460 x 230 x 230	5.714e-3	3.4	1.66e-3	2.84e-7

5.3.1. Low turbulent statistics results

The paper by Kim *et al.* on the DNS simulation of $Re_\tau = 180$ turbulence was the first of its kind [39]. Therefore, the simulation of turbulent channel flow $Re_\tau = 180$ has been widely used as a primary reference in many subsequent research on turbulence [87][33]. So also in turbulent simulation research using the (FM-)LBM [69][88][3].

This section compares the FM-LBM D3Q19 GPU implementation simulation results to the turbulence characteristics found by Kim, Moser, and Mansour [54] (KMM). The turbulent first-order statistics are also compared to the BGK simulation by Amati *et al.* [3], the FM-LBM D3Q18 simulation using local grid refinement by Rohde [69] and the FM-LBM D3Q19 CPU implementation by Zhuo and Zhong [88] (ZZ).

First, some comments will be made on the question if the proposed simulations did in fact statistically converge. Following that, the agreement of first- and second-order turbulent statistics with the expected physical behavior is elaborated on.

Statistical Convergence

The simulations of Newtonian turbulent flow discussed in the following two sections all started from random fluctuations as described in section 3.3. To be able to compare the turbulence statistics with KMM, first the simulation needed to reach a statistically converged state. As mentioned in section 3.4 this is checked by determining the change in average streamwise flow profile over time. The change is expressed in terms of L_2^{conv} through equation (3.13).

Figure 5.3 shows the L_2^{conv} time dependence for the simulation $Re_\tau = 180$. For this simulation, every average flow profile is obtained by saving u_x over intervals of $\Delta t_c = 100 [t]$, $N_c = 1000$ times. As can be seen in Figure 5.3 it takes approximately $0.6 \cdot 10^6 [t]$ time steps for L_2^{conv} to approach a small constant value of approximately $L_2^{conv} \approx 0.005$. Therefore, the convergence time of this simulation can be approximated to be $t^+ \approx 63$. This is slightly more than the convergence time taken by ZZ ($t^+ = 56$) but less than the time taken by Rohde ($t^+ = 80$).

It is interesting to note that the method to determine statistical convergence differs from the method used by KMM. They chose to wait for the total shear stress to reach a linear relation in z following the equation

$$-\overline{u'w'} + (1/Re_\tau) \frac{\partial \bar{u}}{\partial z} \quad (5.8)$$

to determine the point the simulation reached the statistical converged state [59][54].

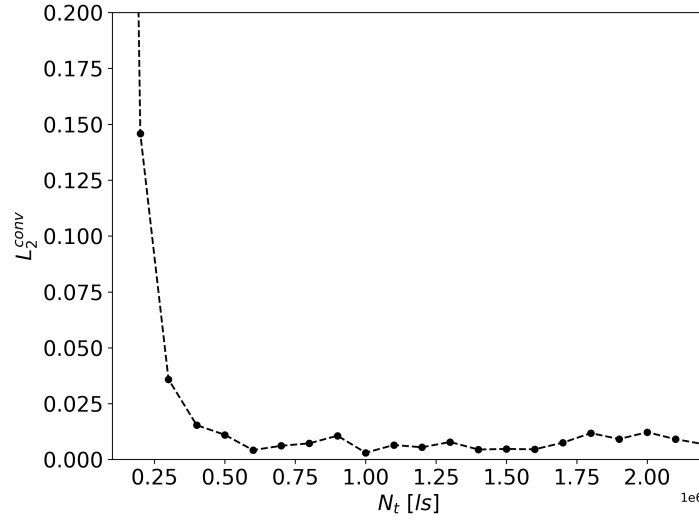


Figure 5.3: Figure shows the L_2^{conv} convergence over time for the long $Re_\tau = 180$ turbulent simulation

This method is not applied in this research because it requires more memory and simulation time steps to determine if the simulation has reached a converged turbulent state. This is due to the fact that, to obtain $-\overline{u'w'}$, the average of u and w must first be obtained. The number of time steps between every determination of convergence is therefore doubled, requiring more simulation steps to pinpoint the moment of convergence. However, in retrospect, the efficiency gain for the method chosen in this research is negligible compared to the overall simulation time. Upcoming researchers are therefore advised to opt for the method used by KMM.

The convergence method does, however, result in a good determination of the statistically converged turbulent state. The final total shear stress relation follows the expected behavior, as can be seen in Figure 5.4d and the convergence indication $L_2^{conv} \approx 0.005$ happens around the same t^+ as other research. The method is therefore assumed to be adequate and all the statistical data for the next chapter will therefore be regarded as statistically converged.

First Order Turbulent Statistics

The results of all the theoretically non-zero first-order turbulent statistics of the converged $Re_\tau = 180$ turbulent channel flow are presented in Figure 5.4. These figures show good agreement with the widely used benchmark case by KMM [39][54]. Where the results differ from the expected behavior and why will be discussed in the next section.

That the average stream-wise velocity profile \bar{u} as calculated via (3.11) corresponds well with the expected behavior, can be seen in Figure 5.4a. The \bar{u} profile shows good agreement with KMM as well as with the linear viscous sub layer relation

$$u^+ = z^+ \quad (5.9)$$

for $z^+ < 5$ and the wall region relation

$$u^+ = 2.5 \log(z^+) + 5.5 \quad (5.10)$$

for $z^+ > 30$ [59].

Interestingly, KMM used a variable grid spacing with the first mesh point in $z^+ \approx 0.05$ and a maximum grid spacing in the center of $\Delta z^+ = 4.4$. On the contrary, the LBM simulations presented in this research all have constant grid spacing. The spacing for the $Re_\tau = 180$ simulations is equal to $\Delta z^+ = 2.8$ making the difference in spacing of the first halfway point $1.4/0.05 = 28$ times larger compared to KMM. However, this low resolution does not seem to have a significant effect on \bar{u} .

However, the low resolution has a significant effect on the results in the streamwise vorticity found in Figure 5.4c. Here, an 70% overestimation of streamwise vorticity fluctuations near the wall is found w.r.t. KMM. The fact that this deviation can be attributed to a higher spatial resolution can be substantiated

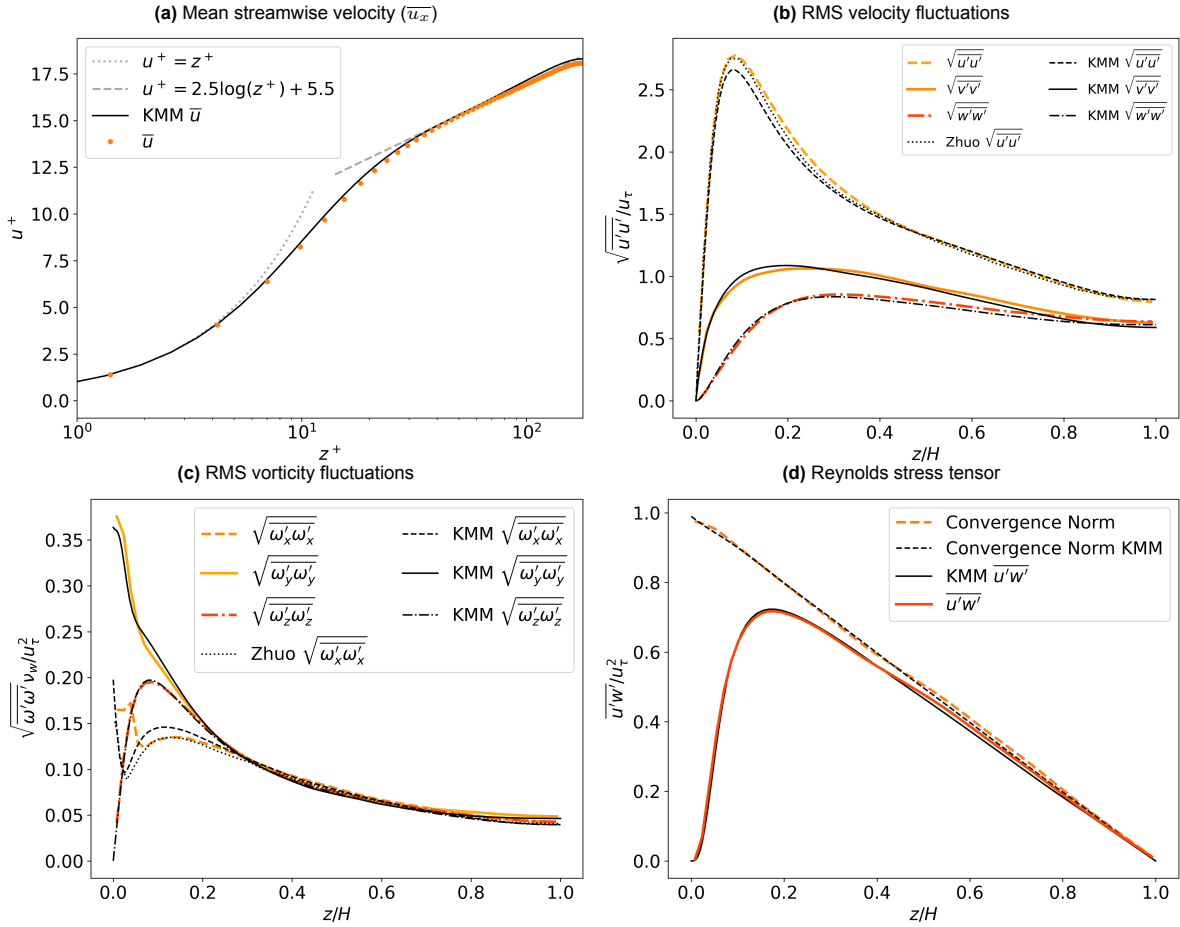


Figure 5.4: Figures display turbulent statistics from the fully developed Newtonian turbulent channel flow simulation at $Re_\tau = 180$. Data is compared to a spectral method simulation by KMM [39][54] and a LBM simulation by Amati *et al.* [3]

with two observations. First, the results found by ZZ show better agreement in the vorticity. They achieved this improvement by increasing the resolution and increasing the domain size. Second, further research in finding the effects of a larger domain presented in this research in Table 5.2 did not improve the vorticity profile. Therefore, it can be deduced that the superior results found by ZZ can be attributed to the higher spatial resolution.

The low spatial resolution compared to KMM has an unknown effect on the statistical results, such as the fluctuating velocity statistics, as found in the figures 5.4b. Here, the streamwise component of the fluctuating velocity $\overline{u'u'}$ shows a 5% deviation from the expected behavior found by KMM. Amati *et al.*, who also found the same error in $\sqrt{u'u'}$, contribute this to two effects [3]. Firstly, Amati *et al.* state that lack of resolution can result in this overshoot, as reported by Kravchenko and Moin [41]. Secondly, the overestimation could be explained by the second-order accuracy of the LBM. The exact contribution of these two errors remains unknown. Given the goal of this research, this will be left for further research.

Regarding the low Reynolds number $Re_\tau = 180$ turbulent results, the following can be concluded. Most first-order statistics show very good agreement with the expected physical behavior represented by the DNS results of KMM. Only the streamwise vorticity and velocity fluctuations show a slight error, which can mostly be attributed to the low wall resolution, and will be taken for granted in the remainder of this study. What effect these inconsistencies will have on the final results will, however, be considered in the next sections.

5.3.2. Transitional and high turbulent flow simulations

To further benchmark the FM-LBM implementation, the turbulent statistics of transitional and high Reynolds number regimes will now be compared to results from literature. Specifically, the well es-

established high Reynolds number simulations by KMM [54] and the extensive transitional turbulent DNS study by Tsukahara *et al.* (TS) [79] will be used for comparison. The results of this study are shown in Figures 5.5 where the results of low $Re_\tau = 180$ are also added.

Computational Domain Size

Before the statistical data is analyzed, a quick note will be made on how the input data for the different simulations found in table 5.2 are chosen. To determine the domain size for step 3 in the initialization steps of section 3.3, the following decisions are made for the high and transitional turbulent regimes.

For the high turbulent simulations the number of grid points is increased with the scaling found in (2.32) rewritten to

$$\frac{N_z^{(2)}}{N_z^{(1)}} = \left(\frac{Re_\tau^{(2)}}{Re_\tau^{(1)}} \right)^{\frac{3}{4}} \quad (5.11)$$

where 1 correspond to the $Re_\tau = 180$ simulation input. This is a larger increase in the number of grid points compared to KMM. However, due to homogeneous grid spacing restrictions of the LBM, the resulting domain size and wall resolution still fall way behind on the simulations by KMM. Specifically, in the current simulation, the wall resolution is still 25 times coarser, and the domain sizes in the stream and span directions are $\frac{1}{2}\pi$ times smaller.

The decision to set the transitional $Re_\tau = 110$ computational domain to match the long simulation domain of $Re_\tau = 180$ is based on the findings of TS [79]. According to their research, in transitional turbulence, the size of large turbulent structures increased with decreasing Re_τ . The simulation therefore requires a correspondingly larger domain to fully encompass them. However, the current LBM $Re_\tau = 110$ simulation still utilizes a domain size that is smaller than the one used by TS. Specifically, the stream-wise domain is 1.6 times smaller and the span-wise domain is 3.2 times smaller compared to the domain used by TS.

The rest of the simulation parameters are found using the steps from section 3.3. How the simulation results hold up on the smaller domains will be discussed next.

First Order Turbulent Statistics

When looking at the first-order statistically converged turbulent statistics in Figure 5.5 the results show almost equally good agreement for transitional and high turbulent statistics as for the $Re_\tau = 180$ turbulent statistics discussed in the previous section. There are, however, two issues to discuss, regarding the streamwise velocity fluctuations and the average flow profile of the $Re_\tau = 110$ simulation.

In Figure 5.5a, it is interesting to observe that the $Re_\tau = 110$ simulation displays an underestimation of the expected behavior in the average velocity profiles. Upon closer examination of the velocity fluctuations in Figure 5.5b, the overestimation compared to the expected behavior decreases from 5% for the $Re_\tau = 395$ and $Re_\tau = 180$ simulations to 3.5% for the $Re_\tau = 110$ simulation. This decrease in both average and fluctuating stream-wise velocity statistics can be attributed to the insufficient domain size, as noted by TS. They discovered an underestimation of the stream-wise velocity statistics due to inadequate domain sizes in a transitional turbulent state with $Re_\tau = 80$. Interestingly, this effect of insufficient domain size on velocity statistics is not observed for the $Re_\tau = 180$ and $Re_\tau = 395$ simulations, as confirmed by Chin *et al.* [17]. Their research demonstrated that insufficient domain size has a limited impact on first-order turbulent statistics when considering higher Re_τ turbulence.

Considering the goal of this research the $Re_\tau = 110$ first-order turbulence statistics are sufficient. However, the fact that transitional turbulent simulations require a longer domain whilst maintaining a fine resolution creates a challenge for the current FM-LBM implementation. In the current setup the resolution and domain size cannot scale independently from each other, which directly scales the number of grid points with the size of the domain. Without a form of grid refinement, the further study of transitional turbulence is therefore hindered by memory constraints.

Two Point Correlation

When considering second-order turbulent statistics, the insufficient domain size has a more significant influence on the results. This can be seen in Figure 5.5d where the long and medium $Re_\tau = 180$ simulations show different medium streamwise correlation results. The reason for the increased correlation for the shorter domain size is due to the periodic boundary conditions making the correlation go to 1

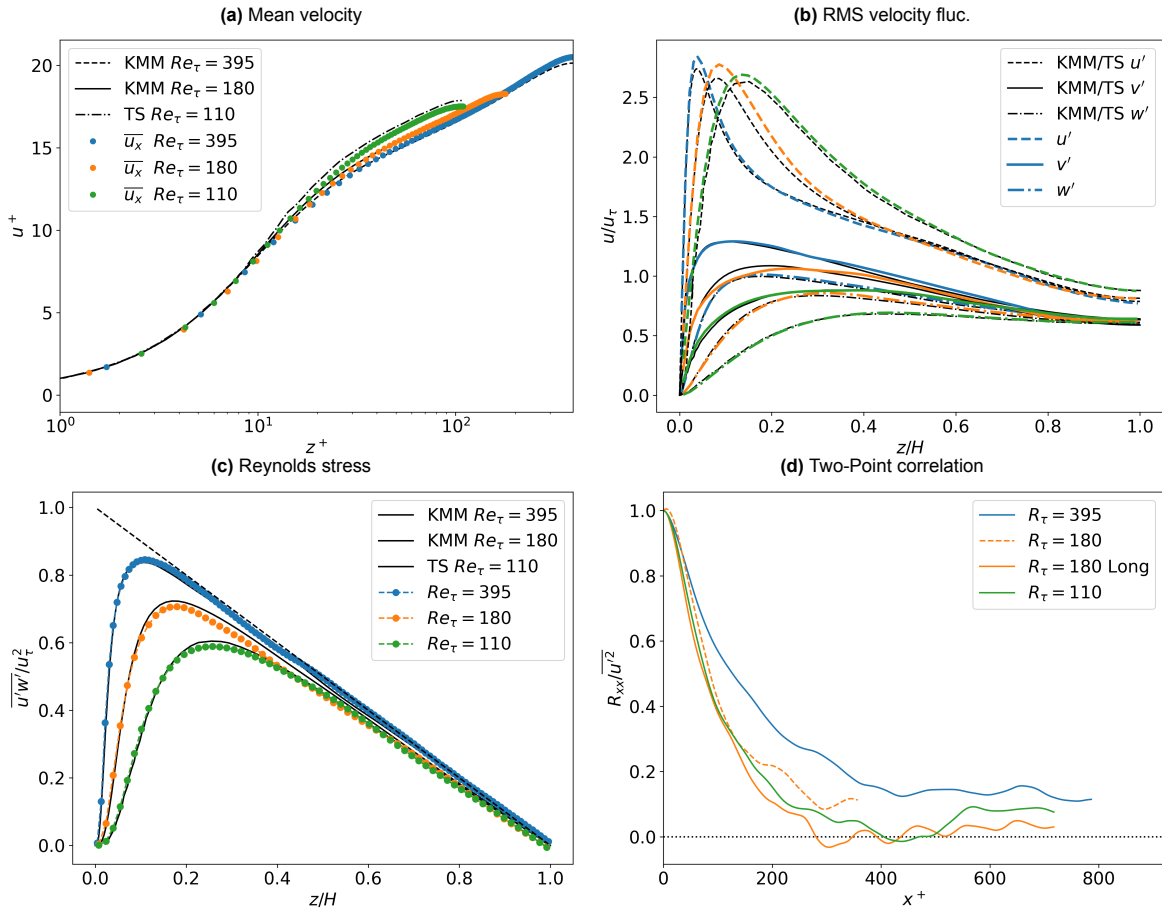


Figure 5.5: Figures display turbulent statistics from the fully developed Newtonian turbulent channel flow simulation at $Re_\tau = 180$ and $Re_\tau = 395$. The first order turbulent statistics in Figures 5.5a, 5.5b and 5.5c are compared to the simulation by KMM [54] and TS [79]. Figure 5.5d shows the streamwise component of the two point correlation function in the middle of the channel ($z^+ = 179$). The two point correlations do not represent the physical behaviour represented by KMM due to among other things an insufficient domain length and sample size.

exactly a domain length away from the reference point. This same effect also overestimates the correlation of $Re_\tau = 395$ since KMM also finds a slight overestimation with a $\frac{1}{2}\pi$ longer domain. This effect of insufficient domain size on the two-point correlation is also reported by TS.

It must also be noted that the fluctuations in the two-point correlation profiles are artifacts generated through an insufficient amount of data samples N_p . This observation aligns with the findings of KMM, who also reported slight fluctuations in their data. The data represented in the figure is therefore not a good representation of the expected behavior.

An effect that can be deduced from the different simulations is the increased stream-wise correlation for lower Re_τ turbulent simulations. This gives an indication that transitional turbulence generates larger turbulent structures. The same trend was also observed by TS, providing an additional indication for the slight underestimation of streamwise mean and fluctuating velocity in the $Re_\tau = 110$ simulation, which can be attributed to the insufficient domain size.

5.3.3. Newtonian Turbulence Benchmark Conclusion

Overall, the first-order turbulent statistics show reasonably good agreement with well established turbulent statistics from KMM and TS [54][79]. Larger deviations from expected behavior come to show when looking at the second-order turbulent statistics. However, given the goal of this research, only requiring first-order shear rate statistics, this extra deviation is less important. Therefore, the current results are deemed adequate for use in this research.

With these final Newtonian turbulent channel flow simulations, the bench marking of the proposed fluid dynamics model, consisting of the FM-LBM implemented on the GPU, is finalised. For low and high

turbulent simulations the current method shows good performance. However, given the coupled resolution and spatial dimensions, the near-wall resolution and total domain size remain limited by memory. This influences the stream-wise velocity fluctuations and transitional turbulence characteristics more significantly. Given that the non-Newtonian simulations presented in the next section will use similar resolutions as the simulations stated in this section, the influence of these lower resolutions will be considered in the further results. Specifically the resolution effects on the shear rate profiles discussed in Section 5.5 as well as the conductivity and resistance results in Chapter 6 are thoroughly discussed.

5.4. Turbulent non-Newtonian Simulations

Now that the FM-LBM method has proven its reliability by benchmarking against analytical and literature data, it will be used to simulate non-Newtonian turbulence in a SSFB. The power-law viscosity model (2.30) will be used to mimic the shear thinning behavior of the CB suspension. Specifically, this section will discuss turbulent DNS simulations for fluids with a non-Newtonian shear thinning rheology at different general wall shear stress Reynolds numbers Re_τ^G for decreasing power-law indices n . The simulation results from this section will be used in the research below, to determine the effect of turbulence on the internal conductivity and resistance of the CB suspension inside an SSFB.

Section 5.4.1 will discuss the input parameters used in shear thinning turbulent simulations at different turbulent regimes, represented in Reynolds numbers $Re_\tau = 110$, $Re_\tau = 180$ and $Re_\tau = 395$. Subsequently, Section 5.4.2 will discuss the first-order turbulent statistics and compare these results with non-Newtonian pipe flow simulations. Finally, Section 5.4.3 concludes by discussing the damped turbulent effect found for shear thinning rheologies.

Table 5.3: Numerical settings for the turbulent non-Newtonian power-law viscosity channel flow simulations

Re_τ^G	n	$Re_\tau^{G,out}$	Re_m^G	$\frac{K}{\rho} [ls^2 lt^{2-n}]$	$g [ls lt^{-2}]$	$u_\tau [ls lt^{-1}]$
110	0.6	109.1	3292	4.157e-4	3.674e-7	4.849e-3
180	0.9	181.1	2828	1.592e-3	6.942e-7	6.667e-3
180	0.8	177.9	2930	1.070e-3	6.942e-7	6.667e-3
180	0.7	178.4	3005	7.118e-4	6.942e-7	6.667e-3
180	0.6	174.9	3174	1.552e-4	1.372e-7	2.962e-3
395	0.8	399.8	7227	7.581e-4	2.839e-7	5.714e-3
395	0.6	396.3	7470	3.453e-4	2.839e-7	5.714e-3

5.4.1. Non-Newtonian Input Parameters

Before we look at the statistical results, the input parameters and initialization are discussed that are used for the simulation that are represented in Table 5.3. To obtain these input parameters for the varying combinations of n and Re_τ^G , the steps of Section 3.3 are used. This section, elaborates on, the decisions for the wall friction velocity u_τ and domain size D needed for Steps 2 and 3, respectively.

- **Step 2:** There are several choices made for u_τ in Step 2. In most cases, u_τ is taken to be equal to its Newtonian counterpart. However, when the combinations of Re_τ^G and n are expected to show weakly turbulent or even fully laminar characteristics, a different u_τ is chosen. In these cases, specifically for $(Re_\tau^G = 110, n = 0.6)$ and $(Re_\tau^G = 180, n = 0.6)$ u_τ is obtained taking the laminar u_{max}^+ . This is done to make sure the lattice velocity does not exceed $\bar{u}_{max} \leq 0.2 [ls lt^{-1}]$.
- **Step 3:** The choice of domain size D in Step 3 varies for Re_τ^G . The non-Newtonian simulations of $Re_\tau^G = 110$ and $Re_\tau^G = 395$ make use of the computational domain $D = (512, 128, 128)$ and $D = (460, 230, 230)$, equal to that of their Newtonian counterparts. The $Re_\tau^G = 180$ simulation uses a domain identical to that of the $Re_\tau^G = 110$ simulation. The choice of larger domain sizes for lower turbulent regimes is made due to the longer turbulent structures expected for shear-thinning turbulence, as found in [30].

The final input parameters g and K are found by completing the steps in section 3.3. The non-Newtonian simulations are initialised using the statistically converged distribution function of the respective Newtonian Re_τ^G simulation. Finally, similar to the Newtonian simulation, equation (3.13) is

used to determine the moment the simulation reaches a statistically convergent state. After this moment, the statistical data discussed in the next section are gathered using the same number of probes $N_p = 80$ and time steps between them $\Delta t_p = 10.000 [lt]$ as the Newtonian simulations.

5.4.2. Non-Newtonian Turbulence Results

This section will discuss the results of the shear thinning turbulent channel flow simulation found using FM-LBM. The statistical characteristics of the power-law viscosity simulations for varying general wall shear stress Reynolds number Re_τ^G and power-index n will be compared to comparable data for pipe flow simulations. Specifically, the DNS work done by, among others, Gavrilov and Rudyak [30] (GR) and Rudman *et al.* [71][70] will be used as validation material for the channel flow DNS simulations presented in this study.

First Order Non-Newtonian Turbulent Viscosity Statistics

First, the first order viscosity statistics will be discussed shortly. This is done to determine whether the cut-off viscosity of $\nu_{max} = 50 [ls^2 lt^{-1}]$ is adequate when simulating shear thinning turbulence using the FM-LBM. As can be seen in a randomly chosen fluctuating viscosity field from the simulation of $Re_\tau = 395$, $n = 0.6$ in Figure 5.6a, the viscosity fluctuates between $\nu = 0.0023 [ls^2 lt^{-1}]$ and $\nu = 0.02 [ls^2 lt^{-1}]$, which is well below the maximum viscosity. Also, the average viscosity curves shown in Figure 5.6b show a smooth line with no unexpected behavior. Since the viscosity lies well below the cutoff point of the viscosity $\nu_{max} = 50 [ls^2 lt^{-1}]$, it is assumed that it is adequate. Since viscosity only increases compared to Newtonian viscosity the under limit of the viscosity ν_w is also assumed adequate.

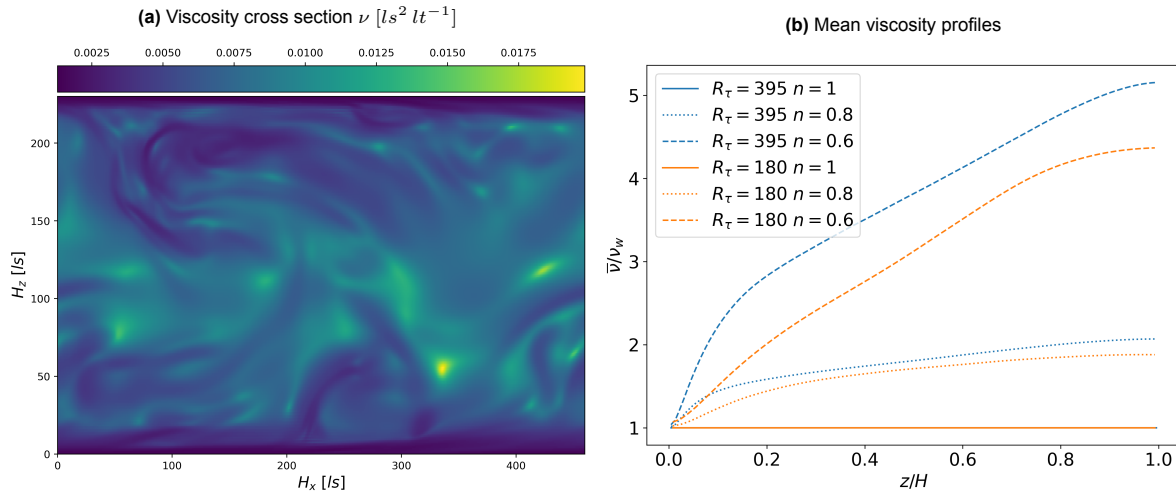


Figure 5.6: The left Figure shows a cross section of an instantaneous viscosity field of the $Re_\tau^G = 395$, $n = 1$ simulation at $y = \frac{1}{2}H_y$. The right Figure shows the mean viscosity scaled with the wall viscosity for the power indices $n = (1, 0.8, 0.6)$

First Order Non-Newtonian Turbulent Velocity Statistics

Figures 5.7 show the $Re_\tau^G = 180$ and $Re_\tau^G = 395$ statistically converged turbulent statistics of the power-law channel flow simulations with power-law index $n = (1, 0.8, 0.6)$. This section will discuss the validity and identify the main characteristics of these simulation results. The statistical data will also be compared to the turbulent velocity statistics of shear thinning turbulent characteristics found in power-law pipe flow simulations.

The first thing to note is the average stream-wise velocity profile, increasing in the middle for constant Re_τ^G . This can clearly be seen in Figure 5.7a for $Re_\tau^G = 180$ and in Figure 5.7b for $Re_\tau^G = 395$. The physical explanation for this is the high shear rate near the wall, decreasing the viscosity of the shear thinning fluid. To characterise this increase in center line velocity, Clapp's scaling law is used [18]. This scaling law takes the form of

$$\hat{u} = nu^+ = A + B \log \hat{z} \quad (5.12)$$

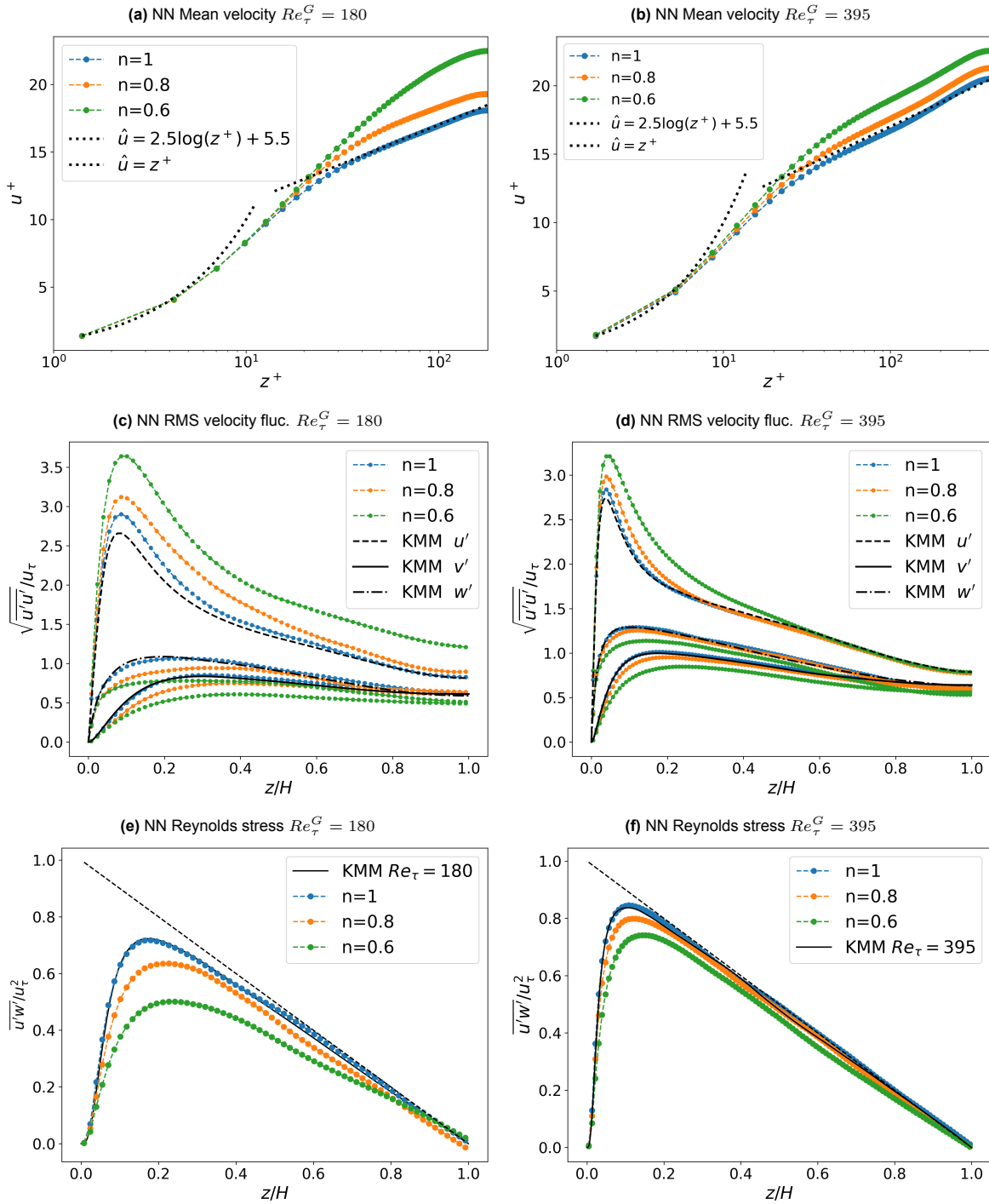


Figure 5.7: Figure shows the velocity statistics for shear thinning power-law fluids in a low and high turbulent state. The low turbulent state is represented by a general wall shear stress Reynolds number of $Re_{\tau}^G = 180$ where the high turbulent state is represented by $Re_{\tau}^G = 395$. Varying degrees of shear thinning characteristics are represented in the power-indices $n \in [1, 0.8, 0.6]$, where $n = 1$ represents the Newtonian behaviour discussed in the previous section.

where

$$\hat{z} = \left[\frac{(\rho^n \tau_w^{2-n})^{1/2}}{K} \right] z^n \quad (5.13)$$

where the constants A and B are set to $A = 2.5$ and $B = 5.5$ for low Re number turbulence and $B = 5.0$ for high Re number turbulence to resemble the Newtonian scaling law (5.10) in the limit $n = 1$. Figures 5.8a and 5.8b compare $\hat{u} = nu^+$ to Clapp's scaling law (5.12). Apart from the $Re_\tau^G = 180$, $n = 0.6$ simulation, the $Re_\tau^G = 180$ results collapse to Clapp's experimentally defined scaling law. Figure 5.8a shows a strong correlation with the scaling law for $\hat{z} > 10$. The simulation $Re_\tau = 395$ shows less agreement with the scaling law, which can be expected since the high turbulent simulation results for $n = 1$ already do not resemble the Newtonian wall region relation (5.10) as found by KMM [54]. The $Re_\tau^G = 180$, $n = 0.6$ simulation differs from the expected behavior, since it exhibits advanced transitional turbulent characteristics [70], which will be further discussed in the next two sections.

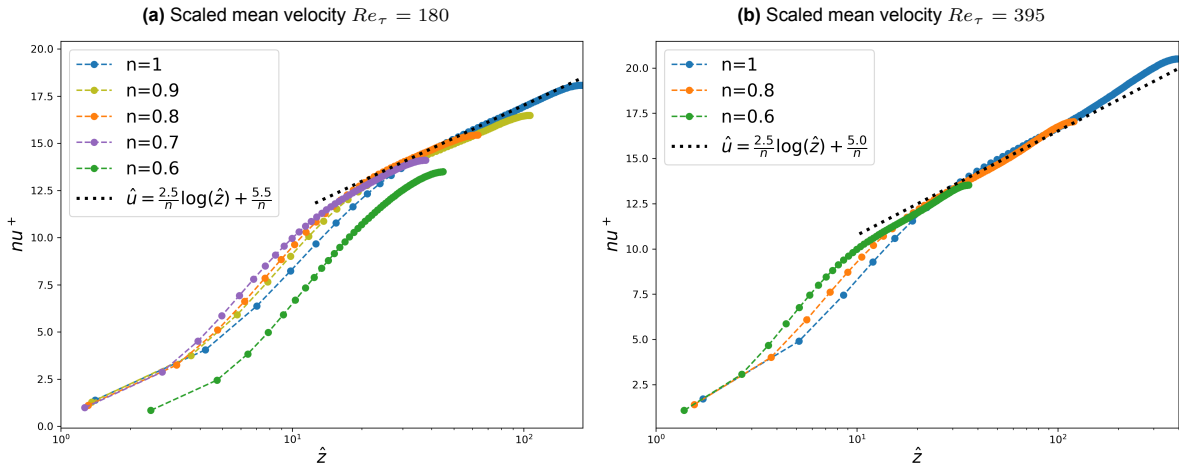


Figure 5.8: Figure shows the mean velocity times profiles (times n) of the non-Newtonian $Re_\tau = 180$ and $Re_\tau = 395$ simulations. The velocity is compared to Clapp's scaling law defined by equation (5.12) with for $Re_\tau = 180$ the constants $A = 2.5$ and $B = 5.5$ and for the $Re_\tau = 395$ simulation a $B = 5.0$.

Secondly, the velocity fluctuations will be discussed in order to further quantify the characteristics of shear-thinning turbulent channel flow. The velocity fluctuations and Reynolds stress characteristics from Figure 5.7 will also qualitatively be compared to known pipe flow simulations. When comparing the current channel flow simulations at $Re_m^G \approx 3000$ ($Re_\tau^G = 180$) and $Re_m^G \approx 7300$ ($Re_\tau^G = 395$) with the high $Re_m^G = 10000$ pipe flow simulation by GR [30] and intermediate $Re_m^G = 5500$ pipe flow simulations by Rudman *et al.* [71], the following similarity is observed.

1. The peak in the streamwise velocity fluctuations $\overline{u'u'}$ increases and slightly moves to the right for decreasing power index n .
2. The non-streamwise fluctuations $\overline{v'v'}$ and $\overline{w'w'}$ decrease with decreasing n .
3. The Reynolds stress term $\overline{u'w'}$ also decreases with decreasing n .

These observations result in the following conclusions, when regarding non-Newtonian turbulence and the reliability of current results.

Firstly, observations 1 and 2 indicate an increased anisotropic turbulence effect for decreasing n . Anisotropic turbulence is the counterpart of isotropic turbulence, which is defined as the invariance of statistical properties under axis rotation [76]. As an example, the Newtonian high channel flow turbulence $Re_\tau = 395$ shows almost isotropic turbulent characteristics in the channel center, since the velocity fluctuations are almost equal in all directions. The increase in shear thinning fluid rheology clearly has an adverse effect on isotropic characteristics, which is especially evident in Figure 5.7c. Here, the decreasing power index n results in an increase in the difference between u', v' and w' constituting a decrease of isotropic turbulence characteristics.

Another conclusion that can be drawn from the first two observations is that the high Re_τ^G simulations show a damped wall normal momentum transfer. To further study this, the turbulent kinetic energy k

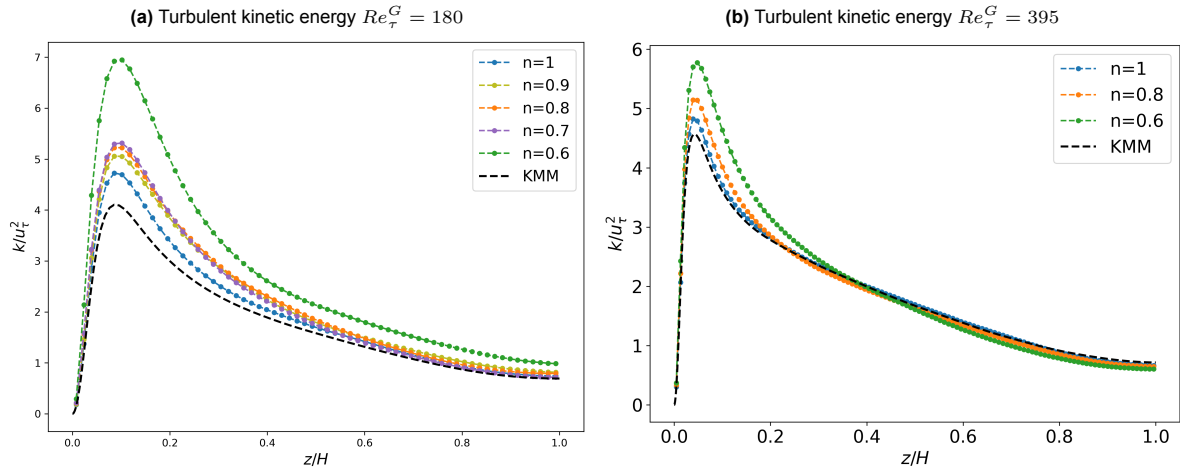


Figure 5.9: Figure shows turbulent kinetic energy for power-law viscosity simulations at low $Re_\tau^G = 180$ and high $Re_\tau^G = 395$.

determined by equation (2.36) is shown in Figure 5.9a for $Re_\tau^G = 180$ and in Figure 5.9b for $Re_\tau^G = 395$. For the $Re_\tau^G = 395$ simulation, a clear increase in k is observed near the wall and a slight decrease in k in the middle of the channel. The pipe-flow simulations by GR also show this change for increased shear-thinning viscosity, but with this change being even more pronounced. The explanation for this behavior for k is a reduced momentum transfer between the near-wall layer and the flow core due to shear thinning viscosity [30]. Specifically, the further away from the wall the lower the shear and therefore the higher the viscosity, resulting in a damped wall normal momentum transfer.

The current low $Re_\tau^G = 180$ channel simulation does not exhibit a decrease k in the center. This can be described in part by a combination of shear thinning and transitional turbulent effects, that increase both the anisotropy of the turbulence and, therefore, the streamwise fluctuations in the center of the channel [78]. Since there is no data, to compare the low Re characteristics with, it is harder to say if the current simulations accurately capture the change in turbulent anisotropy ¹.

5.4.3. Damped Turbulent Effect

The section on non-Newtonian turbulent results will now be concluded with a description of the main effect a shear-thinning rheology has on the turbulent characteristics. This is the observed damped turbulent effect. The main indicators of this damped turbulent effect, as well as its consequences for the design of the SSFB, will be discussed.

A shear-thinning rheology has a damping effect on the characteristics of the turbulence compared to Newtonian turbulence of equal general wall shear stress Re_τ^G . This effect, also found in pipe flow research [71][71], can be substantiated by two observations found when comparing the Newtonian and non-Newtonian results from Figures 5.5 and 5.7, respectively.

- The first indication of the damped turbulence effect is strongly represented in the velocity fluctuations. Specifically, the increase in streamwise fluctuations u' and a decrease in spanwise fluctuations v' and wall normal fluctuations w' , as found in Figures 5.7c and 5.7d, resemble the same trend for decreasing n as it does for decreasing Newtonian Re_t demonstrated by Figure 5.5b. Therefore, a shear thinning rheology has the same anisotropic turbulent effect as decreasing Reynolds numbers [78].
- The damped turbulence effect is also strongly represented in the Reynolds stress term $\overline{u'w'}$. Where the Newtonian results from Figure 5.5c represent the same decrease in $-\overline{u'w'}$ for decreasing Re_τ as the non-Newtonian simulations exhibit for decreasing n .

From these observations, it can be concluded that the turbulent shear thinning flow for a given Re_τ^G resembles the same turbulent characteristics in velocity fluctuations as Newtonian flow with lower Re_τ . As a result, the Re_τ^G for which the laminar flow starts to transition to turbulence, from now on called

¹During the finalisation of the current research a paper did come out studying $Re_\tau = 180$ turbulent power-law flow at a power index $n = 0.5$ [36] using OpenFOAM with a larger domain. Upcoming research on non-Newtonian turbulence simulations using the LBM is advised to use this research for further analysis.

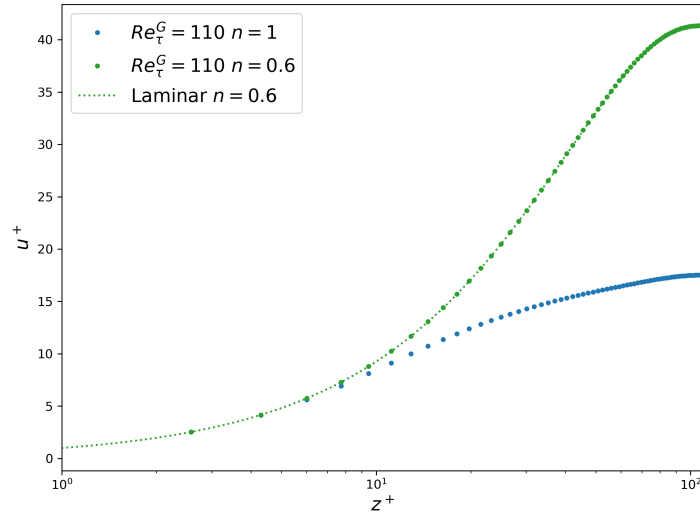


Figure 5.10: shows the mean streamwise velocity profile for the $Re_{\tau}^G = 110$ power-law viscosity simulations. The two power-law indices show are $n = 1$ representing Newtonian flow and $n = 0.6$. The $n = 0.6$ simulation shows full agreement with the laminar solution (5.2).

$Re_{\tau}^{G, \text{Transition}}$, also increases for shear-thinning fluids. This can be clearly seen in Figure 5.10 where the turbulence in the simulation ($Re_{\tau}^G = 110, n = 0.6$) has completely died down, creating a laminar flow profile in the stream direction.

For Newtonian flow, the wall shear stress Reynolds number for which the flow transitions from a laminar to a turbulent state is found to be $Re_{\tau}^{\text{Transition}} \approx 64$ [79]. Given the strong shear thinning characteristics of the CB suspension, the suspension will reach a turbulent state for $Re_{\tau}^{G, \text{Transition}} \gg 64$. However, more research is needed on how $Re_{\tau}^{G, \text{Transition}}$ depends on n and what the exact transition point will be for the CB suspension in an SSFB.

The next sections will focus on the effect of turbulence on the conductivity and resistance of a CB suspension. This will help determine if reaching a turbulent state is favorable in the first place. Some notes on the scaling of the pumping power will also be made.

5.5. Turbulent shear profiles

Within the field of turbulent channel flow research, the statistical characteristics of the shear rate are under reported. However, shear rate profiles are central to studying the effect that turbulence has on the conductivity of CB suspensions and with that the internal conductivity and resistance of a SSFB [86]. Therefore, this section will report on the statistical shear rate characteristics of a shear thinning power-law viscosity fluid for different turbulent domains.

Effect of Shear Thinning Rheology and Re_{τ}^G on shear rate

Figure 5.11a shows the normalised mean shear rate profiles, and Figure 5.11b its RMS fluctuations, derived from the fluctuating shear rate profiles using equation (3.11) and (3.12) respectively. The shear rate $\dot{\gamma}$ is defined by (2.29) where the velocity gradients follow directly from the moment vector α_k in the FM-LBM. To obtain the shear-rate statistics an equal amount of probes is used as for the previous-mentioned turbulent statistics.

The following can be observed when comparing the shear rate characteristics of different flow regimes Re_{τ}^G and rheologies n .

- Firstly, when considering the effects of shear thinning rheology, Figures 5.11 only show a small effect of the power index n on $\bar{\gamma}$ and $\dot{\gamma}'$. Specifically, only a small difference is found in the shear rate profile between the simulations $Re_{\tau}^G = 180, 395$ for the power law indices $n = 1, 0.8, 0.6$.
- Second, when considering the differences between the shear rate profiles at different flow regimes, the most drastic difference for varying Re_{τ}^G is found when comparing the laminar and turbulent flow regimes. In the center region where the laminar flow profiles go to zero, the turbulent flow

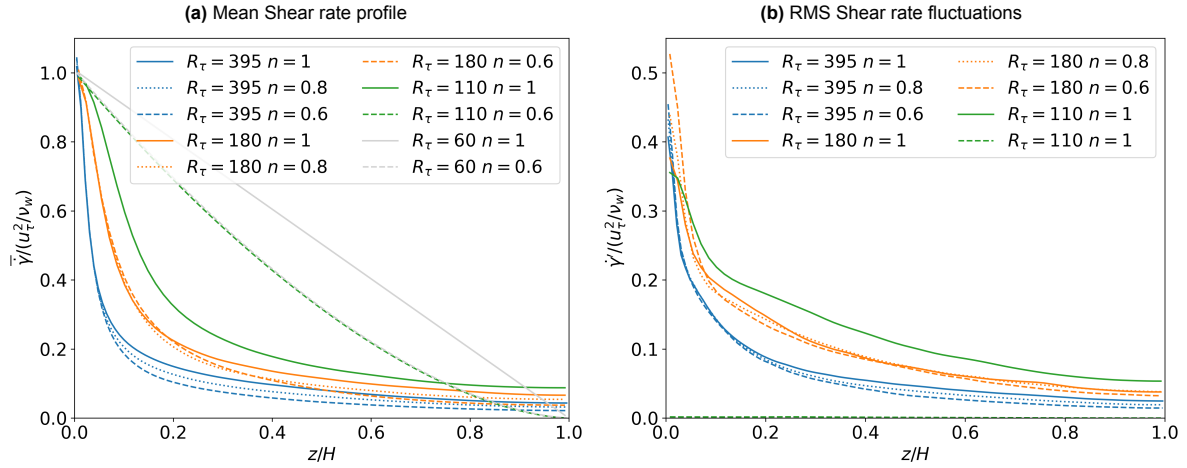


Figure 5.11: Figure shows the mean and RMS fluctuating shear rate profiles for different turbulent power-law fluid channel flow simulations.

profiles remain $\bar{\dot{\gamma}} > 0$ throughout the channel. Noteworthy, the laminar $\dot{\gamma}$ do not go to zero entirely, due to the finite resolution and an even amount of N_z grid points.

Given the significant difference in the laminar and turbulent shear rate profile, the most significant effect a shear thinning rheology has on the shear rate profile is the increase in $Re_\tau^{G, \text{Transition}}$ for decreasing n . This is evident when comparing the Newtonian transitional turbulent simulation ($Re_\tau^G = 110$, $n = 1$) with the non-Newtonian laminar simulation ($Re_\tau^G = 110$, $n = 0.6$).

Comparing Shear Rate Profiles in Physical Units

The above analysis compared the shear rate profiles in a non-dimensional sense. In the next chapter, the shear rate profiles will have to be converted to physical units, such to use the experimental data from Youssry *et al.* to obtain the conductivity fields [86]. Here, the shear rate profiles will be compared in a randomly chosen physical dimension such to get a feeling of how the Re_τ^G compare in the physical world. The following section will discuss how the conversion to physical units is made as well as elaborate on the main takeaways from the results shown in Figure 5.12.

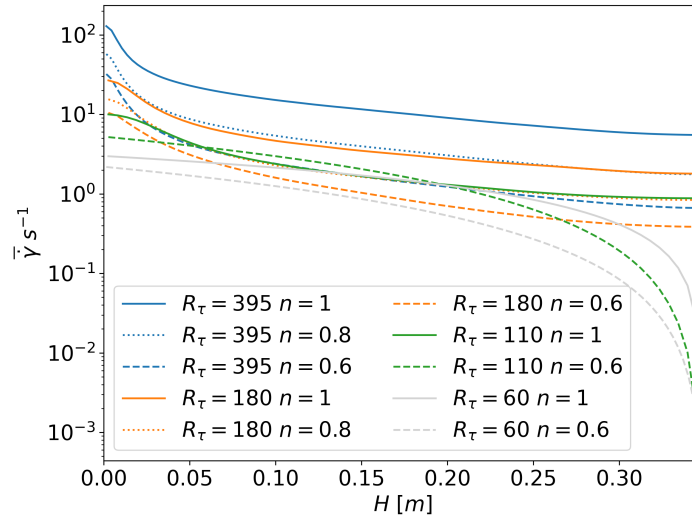


Figure 5.12: Figure shows same average shear rate results as found in Figure 5.11a but converted to dimensional units. For this conversion an arbitrary height $H = 0.35$ [m] and consistency index/density combination $K/\rho = 1e-4$ [$m^2 s^{2-n}$] is chosen.

To convert the shear rate to dimensional units given a Reynolds number, the following equation

derived from (2.42) is used

$$\bar{\dot{\gamma}}_w = \left(\left(\frac{Re_\tau^G}{H} \right)^2 \frac{K}{\rho} \right)^{\frac{1}{2-n}} \quad (5.14)$$

The height is arbitrarily set to $H = 0.35 [m]$ and consistency index/density combination is set to $K/\rho = 1e-4 [m^2 s^{2-n}]$.

It is clear that, while the shapes may not differ much in the turbulent state, the dimensional shear rates increase substantially with increasing Re and n . This increase follows directly from (5.14) and can be expressed by

$$\frac{\bar{\dot{\gamma}}_w^{(1)}}{\bar{\dot{\gamma}}_w^{(2)}} = \left(\frac{Re_\tau^{G(1)}}{Re_\tau^{G(2)}} \right)^{\frac{2}{2-n}} \quad (5.15)$$

for equal height H and viscosity characteristics n, K between situations (1) and (2). The decrease of $\bar{\dot{\gamma}}_w$ for decreasing n represents the drag-reducing property of shear-thinning turbulence. Therefore, the pumping power needed to reach a certain Re_τ^G decreases, as will be discussed in the next chapter.

Discussion

When evaluating the reliability of the given shear rate characteristics, it is important to consider the impacts of insufficient resolution and domain size, as mentioned in the previous section. The effects can be summarised as follows.

- The largest error due to the insufficient resolution in first-order Newtonian turbulent statistics is the overestimation of velocity fluctuations, with a maximum overestimation of 5% in streamwise velocity fluctuations. Although this overestimation may have a small effect on shear rate fluctuations ($\dot{\gamma}'$), it has minimal impact on the mean shear rate ($\bar{\dot{\gamma}}$) since increased fluctuations contribute equally to positive and negative shear rate contributions.
- As discussed, the insufficient domain size will have the most significant effect on the transitional turbulent effects. It is unknown how this effect translates into the shear rate profile. Therefore, further research is recommended, using larger domain sizes.

Overall, the errors are assumed to be small and the shear rate data are therefore deemed sufficient for the rest of this research.

6

Carbon Black Turbulent Conductivity and Resistance Results

This final chapter will discuss the effects of turbulence on the electrical conductivity and resistance of a Carbon Black suspension inside a semi-solid flow battery. The shear rate profiles obtained in the previous sections will be used to determine the turbulent conductivity fields inside the anode and cathode flow channels. Since there are no general laws describing the conductivity of CB, the experimental results of Youssry *et al.* will be used to convert the shear rate fields discussed in section 5.5 to turbulent conductivity fields. Using the Finite Volume method, the electric potential inside these turbulent conductivity fields will be determined as described in chapter 4. From these electric potential fields, the resistance and effective conductivity will be determined for varying laminar and turbulent regimes and SSFB dimensions.

Before using the FVM to determine the electrical resistance of the CB suspension, it is first validated in Section 6.1. Then a non-dimensional relation for the resistance characteristics will be derived in section 6.2. The non-dimensional scaling relations from Section 6.2 will then be used, first, to describe the Newtonian effective conductivity and resistance characteristics in Section 6.3. After this, the shear-thinning rheology of CB is also incorporated in section 6.4. Lastly, a thorough analysis of how turbulence affects the electrical conductivity and overall resistance will be discussed. This analysis forms the crux of the research question, shedding light on the implications of turbulence for potential SSFB design, as explored in Section 6.5

6.1. Finite Volume Method Validation

This section deals with the benchmarking of the FVM, implemented to determine the potential inside the variable conductive CB suspension flowing through the SSFB. There are three different checks that can be carried out to determine if the FVM solution corresponds to the expected physical behavior. The chosen checks are the same as in [64] but extended to three dimensions.

The first two checks result from the absence of sources and sinks in the governing differential equation (2.11).

1. The divergence of the current should be zero. Therefore, the net current, through any closed contour outside of the current collectors should be zero. This is checked by adding up the I_x , I_y and I_z contributions within a finite volume which should equate to zero.
2. The current cannot leave the conductor, which means that the total current normal to the potential gradient (z-direction), should be constant inside the conductor, and zero outside.

On top of these checks, a benchmark study is performed with the goal to determine adequate input parameters. Specifically, the benchmark study checks the different choices for the number of grid points making up the surroundings of the conductor N_{sur} as well as the conductivity of that surrounding medium.. To do so, the analytically known potential in a conductor of constant conductance σ is simulated, using the FVM. The reliability of this result is determined by comparing the resistance obtained

Table 6.1: Constant input parameters for potential field calculations.

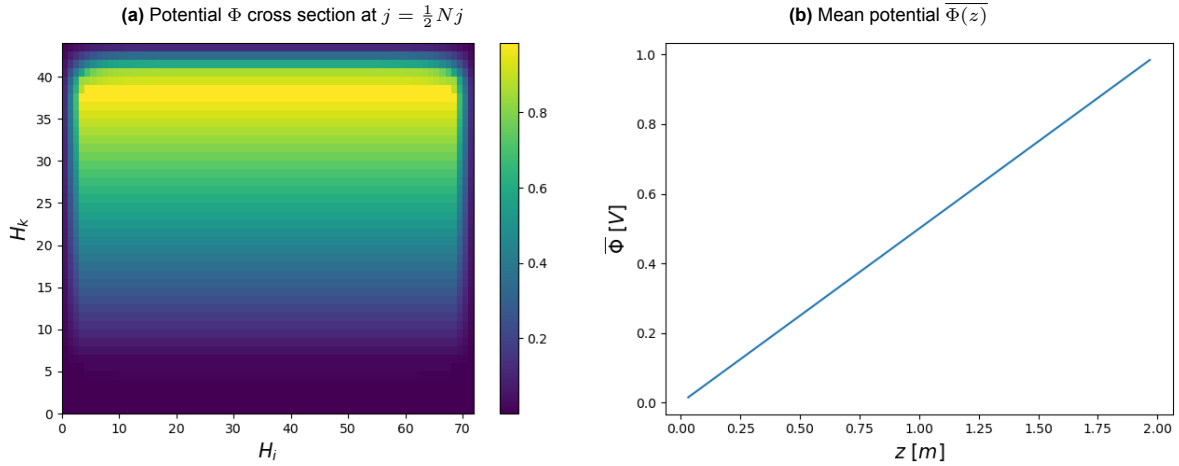
L_{phy}, W_{phy}	2, 0.5	[m]
ΔV	1	[V]
N_{sur}	4	
σ_{sur}	$1e-15$	[mS/cm]

from the simulation R , as described in section 2.1.5 and 4.4, to the resistance given by Pouillet's law

$$R_a = \frac{1}{\sigma_{eff}} \frac{H}{A} \quad (6.1)$$

with H distance between the electrodes and A the area of the electrodes.

Table 6.1 shows the parameters that remain constant in the benchmark simulation as for all further potential simulations. For the benchmark study, the channel half height, which varies in the subsequent simulation, is set to $H_{phy} = 1$, which constitutes the upper limit of the expected simulations to come. The N_{sur} and σ_{sur} were varied just as in [64] and found to be optimal for $N_{sur} = 4$ and $\sigma_{sur} = 10^{-15}$. The average and cross section of the potential field Φ for this simulation are shown in figures 6.1 respectively. The benchmark error of R with respect to R_a was found to be 0.002% which is more than adequate for this study.

**Figure 6.1:** Figure shows the benchmark results of the potential field inside a conductor of constant conductance.

6.2. Non-Dimensional Scaling Analysis

Since there are no known formulas relating turbulent characteristics to conductivity, the Buckingham π_i theorem is used to compute a set of non-dimensional numbers from the known variables influencing the effective conductivity [11][7].

The effective conductivity σ_{eff} , as defined by Pouillet's law (6.1), depends on at least 6 other physical variables such as the electrode-related physical dimensions A and H and potential difference $V = \Delta V$, as well as flow-related variables such as viscosity ν , flow velocity U , and wall shear stress τ_w . The physical dimensions these variables share tallies up to 4. The problem can therefore be described by $p = 7 - 4 = 3$ dimensionless variables.

Different dependent dimensionless parameters can be chosen and the form used in this study is

$$\frac{\sigma_{eff} V^2}{\tau_w U_m H} \propto Re_\tau^\theta \left(\frac{A}{H^2} \right)^\psi \quad (6.2)$$

where the non-dimensional σ_{eff} depends on the Reynolds number describing flow and A/H^2 representing the electrode dimensions. Exponents θ and ψ represent scaling parameters that determine the unknown relation between dimensionless numbers. The next section will establish what these exponents are.

A detailed examination of the non-dimensional effective conductivity is conducted. This non-dimensional number, represented by the left-hand side of (6.2), which encompasses σ_{eff} , can be rewritten in a form that represents the ratio between the electric power and the pumping power. Using the definition of the pumping power in a channel

$$P_p = F_{fric}U_m = 2\tau_wAU_m \quad (6.3)$$

this power number is defined as

$$P_o = \frac{\sigma_{eff}V^2}{\tau_wU_mH} = \frac{V^2\frac{\sigma_{eff}A}{H}}{\tau_wAU_m} = \frac{\frac{V^2}{R}}{\frac{1}{2}F_{fric}U_m} = \frac{P_e}{P_p} \quad (6.4)$$

where P_e represents an electric power obtained using Pouillet's law. It is important to note that P_e does not represent the electrical power of a SSFB. It does, however, represent the ease at which current can flow through the CB network where P_e increases for decreasing R .

The final non-dimensional scaling becomes

$$P_o \propto Re_{\tau}^{\theta_{P_o}} \left(\frac{A}{H^2} \right)^{\psi_{P_o}} \quad (6.5)$$

where the non-Newtonian version can be approximated by replacing the constant kinematic viscosity μ in Re_{τ} , by the wall viscosity μ_w to obtain Re_{τ}^G . It is important to note that the three non-dimensional numbers cannot be easily changed independent of each other. The channel or electrode height H is found, for example, in the Reynolds numbers as well as in the electrode dimensions. The wall shear stress is on the other hand found in the power and wall shear stress Reynolds number.

The next section will use the results of the turbulent flow simulation and the calculation of the resistance R to gain a sense of the scaling in the non-dimensional power scaling represented by (6.5). On top of that the scaling of the dimensional σ_{eff} will be studied using

$$\sigma_{eff} \propto Re_{\tau}^{\theta_{\sigma}} \left(\frac{A}{H^2} \right)^{\psi_{\sigma}} \quad (6.6)$$

to express the characteristics in the exponents θ_{σ} and ψ_{σ} . The scaling of the dimensional R will be expressed using

$$R \propto Re_{\tau}^{\theta_R} \left(\frac{A}{H^2} \right)^{\psi_R} \quad (6.7)$$

6.3. Turbulent Carbon Black Conductivity and Resistance in Newtonian limit

To characterize the effect of turbulence on the effective conductivity and the CB resistance, the effect of Newtonian turbulence is studied first. To do so, the experimentally obtained conductivity dependence on shear rate found by Youssry *et al.* [86] will be used to convert the Newtonian shear rate fields discussed in Section 5.5 to turbulent conductivity fields. Three different conversions to physical units have been performed, to study the effect of turbulence on the CB conductivity in a wide range of that conductivity curve. This will in turn help to define the effect of turbulence on the electron conductivity inside a wide range of SSFB designs.

In this section, the methodology behind the realization of these three different conversions will be elaborated on and discussed in Section 6.3.1. The conductivity fields that result from these conversions are discussed in 6.3.2. After this, the FVM is used to calculate the resistance R and effective conductivity σ_{eff} of the CB suspension resulting from the conductivity fields. Finally, these results are compared to the non-dimensional equations found in the previous section to obtain the different characteristics scaling parameters θ and ψ in the Newtonian limit.

6.3.1. Newtonian Conversion to Physical Units

In all the previous sections, the results were represented without dimensions using the Reynolds number to differentiate between turbulent regimes. The turbulent regimes represented by Re_{τ} are defined by a particular ratio between inertial forces and viscous forces. However, this ratio can be made up of infinitely many combinations of channel half height H , wall shear velocity u_{τ} , and viscosity ν . To determine the conductivity profiles and electrical resistance of the CB suspension inside an SSFB, different

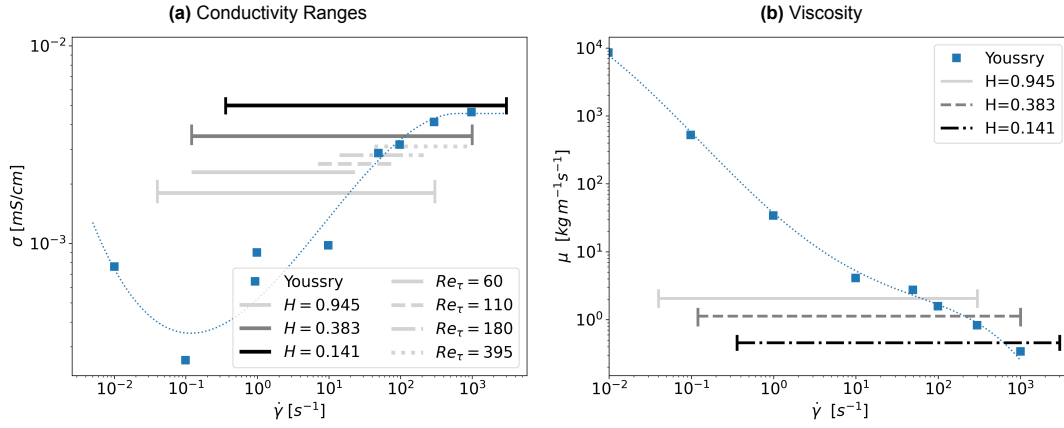


Figure 6.2: Figures show where the different shear rate ranges lie on the conductivity curve for the three H_{phy} chosen. The shear rate range is defined as $\dot{\gamma}_{min}^{(60)} \rightarrow \dot{\gamma}_w^{(395)}$ and encompasses all the local shear rates of the flow regimes considered. As an example, the way the different $\dot{\gamma}_{min}^{(i)} \rightarrow \dot{\gamma}_w^{(i)}$ ranges corresponding to the different Re_τ are represented in full shear rate range is shown for $H_{phy} = 0.383 [m]$ in Figure 6.2a.

choices of physical parameters will be made such as to represent the turbulent flow in different SSFB designs. This section will examine the choices made to determine these physical parameters.

The effect of turbulence on the conductivity of a CB suspension, and with that the internal resistance and effective conductivity of an SSFB, will be studied for different laminar and turbulent regimes. Specifically, the laminar, transitional turbulent, low turbulent, and high turbulent regimes represented by $Re_\tau = (60, 110, 180, 395)$ will be considered.

To make the conversion from lattice units to physical units given the different Re_τ , three different physical channel half height H_{phy} are chosen. These H_{phy} together with Re_τ in turn determine other physical parameters such as the average velocity U_m and the pumping power P_p . How the three different H_{phy} , represented in table 6.2, are chosen, is broken down in the next steps.

1. First, a shear rate range is chosen such to represent the different regions on the experimentally obtained conductivity curve 6.2a[86]. The shear rate range is defined as going from the lowest shear rate of the current simulations belonging to $Re_\tau = 60$ to the highest shear rate belonging to $Re_\tau = 395$. To determine the appropriate shear rate range, three steps are taken.
 - First an upper limit of the shear rate range, corresponding to $\dot{\gamma}_{max}^{(395)} = \dot{\gamma}_w^{(395)}$, is chosen.
 - Then Equation (5.15) is used to determine $\dot{\gamma}_w$ for the other simulations Re_τ .
 - Finally, $\dot{\gamma}_{min}^{(60)}$ is obtained from $\dot{\gamma}_w^{(60)}$ and the shear rate data represented in section 5.5.

How the different shear rate ranges, resulting in the different H_{phy} , lay on the conductivity curve, can be seen in Figure 6.2a. Here for each H_{phy} the ranges, going from $\dot{\gamma}_{min}^{(60)} \rightarrow \dot{\gamma}_{max}^{(395)}$ are expressed in the solid lines.

2. Now a viscosity needs to be chosen, which will be taken constant within one choice of H_{phy} , such to represent a Newtonian rheology. Three different physical viscosities for three different H_{phy} are therefore chosen by taking the viscosity that corresponds to the CB viscosity at the wall shear rate of the $Re_\tau = 180$ simulation, using the viscosity dependence found by Yousry [85]. The choice of $\dot{\gamma}_w^{(180)}$ as reference is due to the $Re_\tau = 180$ simulation lying within the maximum and minimum Re_τ considered in this study. The different constant viscosities used are represented in figure 6.2b.
3. Next to a viscosity, a density also needs to be chosen. To this end the density of the CB suspension used in this study is approximated by $\rho \approx 1200 [kg m^{-3}]$.
4. Finally the physical channel half height can be determined. Using equation (2.40) one can obtain

$$H_{phy} = \sqrt{\frac{Re_\tau^2 K}{\dot{\gamma}_w^{2-n} \rho}} \stackrel{n=1}{=} \sqrt{\frac{Re_\tau^2 \mu}{\dot{\gamma}_w \rho}}. \quad (6.8)$$

Table 6.2: Table represents the different H_{phy} chosen and the resulting physical parameters of the flow profile inside the SSFB assuming constant viscosity per chosen H_{phy} .

H_{phy} [m]	$\dot{\gamma}_{min}$	→	$\dot{\gamma}_w$	Re_τ	\bar{u}^+	$\dot{\gamma}_w$ [s^{-1}]	\bar{U} [$m s^{-1}$]	P_p [kW]
0.945	0.04	→	6.94	60	19.9	6.92	2.17	0.062
	2.1	→	23.3	110	9.30	23.3	1.86	0.178
	4.2	→	62.3	180	15.6	62.3	5.1	1.30
	13	→	300	395	17.8	300	12.6	15.8
0.383	0.12	→	23.1	60	19.9	23.1	2.94	0.153
	7.0	→	77.6	110	9.30	77.6	2.52	0.442
	14	→	208	180	15.6	208	6.90	3.25
	43	→	1000	395	17.8	1000	17.3	39.1
0.141	0.36	→	69.2	60	19.9	69.2	3.25	0.207
	21	→	233	110	9.30	233	2.78	0.597
	42	→	623	180	15.6	623	7.63	4.39
	130	→	3000	395	17.8	3000	19.1	52.9

where μ , $\dot{\gamma}_w$ and ρ represent the physical parameters chosen above. The different H_{phy} resulting from the different shear rate ranges are found in table 6.2

- Using the average velocity \bar{u}^+ obtained from the Newtonian simulations represented in section 5.3.2 and the $\dot{\gamma}_w$ from step 1 the physical velocity \bar{U}_{phy} can be defined using equation (2.45). With this information the pumping power P_p can be determined using equation (6.3) and (2.28)

$$P_p = F_{fric} U_m = 2\tau_w A U_m = 2\mu_w \dot{\gamma}_w A U_m \quad (6.9)$$

where with A the electrode surface set to 1 [m^2].

The above mentioned steps are repeated 3 times resulting in 3 different H_{phy} . The physical parameters corresponding the 4 different Re_τ and 3 different H_{phy} considered are represented in table 6.2.

Now the fluctuating shear rate fields of every Re_τ simulation need to be converted from lattice to SI units given the three different conversions mentioned above. This conversion is simply done by $\dot{\gamma}_{field}^{phy} = \dot{\gamma}_{field}^{sim} \dot{\gamma}_w^{phy}$ where $\dot{\gamma}_{field}^{sim}$ represents the normalised fluctuating shear rate field obtained from the Newtonian simulations presented in section 5.3.2.

How these shear rate fields influence the internal conductivity of CB, and with that the internal resistance and effective conductivity of a SSFB, will be shown in the next sections.

6.3.2. Newtonian Conductivity Results

First of all, the conductivity statistics that result from the different Newtonian Re_τ simulations and subsequent varying conversions are shown in figures 6.3a, 6.3b, 6.3c corresponding to $H_{phy} = 0.141, 0.383, 0.945$ [m] respectively. To obtain these results, the shear rate fields are converted to conductivity fields using experimental measurements by Yousry expressed in equation (2.4). From these fluctuating conductivity fields, the average and RMS conductivity is obtained using equations (3.11) and (3.12) with $N_p = 80$ and $\Delta t_p = 10000$ (equal to the velocity data collection).

Two things can be clearly observed. First, given H_{phy} , a higher Re_τ results in a higher conductivity. This is due to the fact that the conductivity increases in the chosen shear rate ranges. Second, there is a region for which the laminar $Re_\tau = 60$ simulation has a higher average conductivity than the $Re_\tau = 110$ simulation. However, on average, the turbulent simulation still shows slightly higher conductivity. Specifically the varying average conductivity over the full channel $\bar{\sigma}$ for the $Re_\tau = 110$ compared to $Re_\tau = 60$ flow regimes equate to (11.9, 15.6, 16.7) [%] for the heights (0.141, 0.383, 0.945) [m].

It is important to note that the increase in conductivity due to an increase in Re_τ only holds for the SSFB dimensions chosen here. If the H_{phy} is chosen to be smaller i.e. < 0.141 [m] and the shear rate range subsequently higher, the shear rate will become $\dot{\gamma} \geq 634$ [s^{-1}] resulting in a constant σ as can be seen in Figure 6.2a. With constant σ there will obviously be no improvement in conductivity with increasing Re_τ . This also explains the decrease in the percentile difference between the $\bar{\sigma}$ with decreasing H_{phy} discussed in the previous paragraph.

In the particular H_{phy} chosen here, a significant increase in conductivity is found here. The next section will elaborate on the effect this has on the CB resistance and effective conductivity.

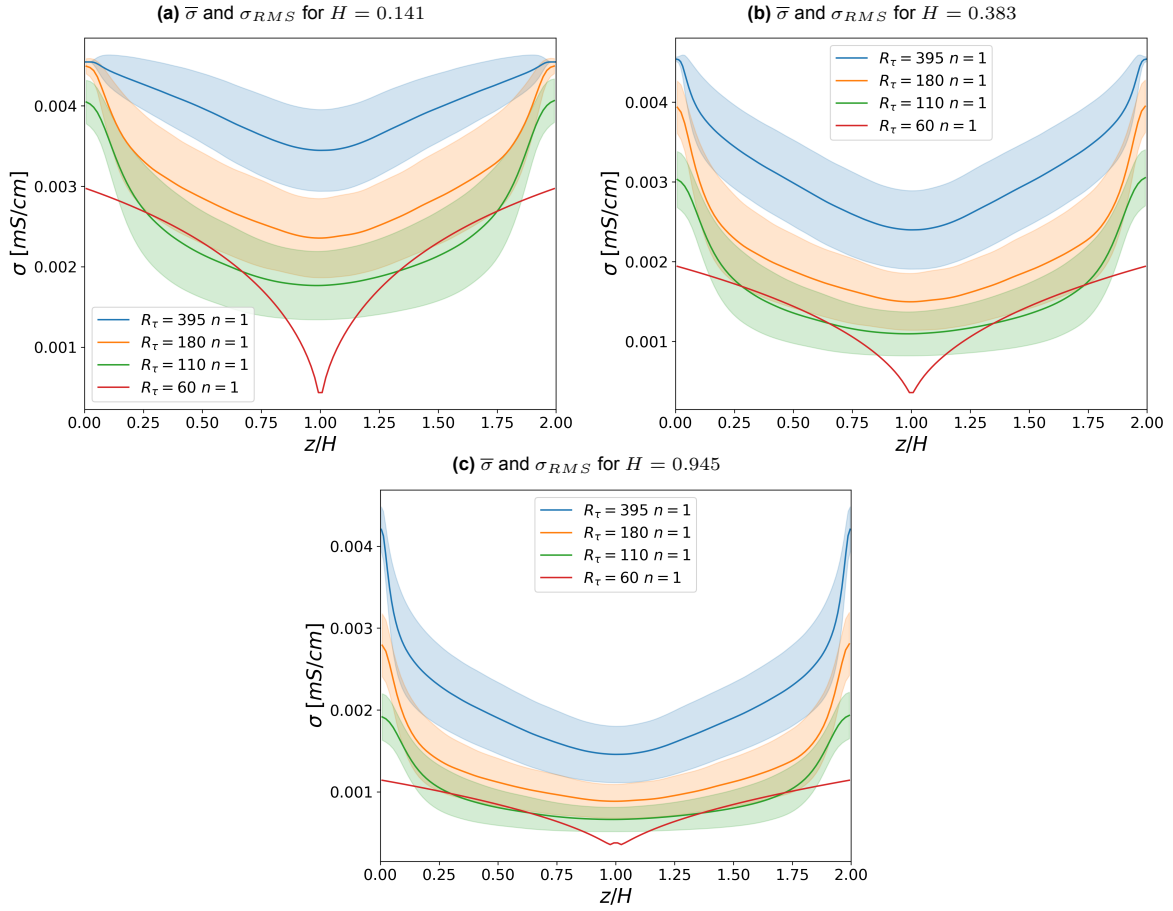


Figure 6.3: The data presented illustrates the mean conductivity curve $\bar{\sigma}(z)$ and the fluctuating conductivity curve $\sigma'(z)$ across the entire channel, considering various channel half heights H_{phy} that were examined. The RMS conductivity fluctuations are represented by the shaded area defined as $\bar{\sigma}(z) - \sigma_{RMS}(z) \rightarrow \bar{\sigma}(z) + \sigma_{RMS}(z)$. The conductivity field from which the statistics are represented here are obtained by converting the Newtonian turbulence shear rate fields to conductivity fields with the experimental data from Youssry *et al.* [86]

6.3.3. Newtonian Resistance and Effective Conductivity Results

Using the Finite Volume method as described in chapter 4 the potential through the varying conductivity field is calculated for every N_p . From this, the fluctuating and average CB resistance \bar{R}_{tot}/R'_{tot} and effective conductivity $\bar{\sigma}_{eff}/\sigma'_{eff}$ are determined. As input for this FVM calculation the heights from table 6.2 and the further input from table 6.1 is used. The dependence of the average and fluctuating contributions of σ_{eff} and R_{tot} as well as the power number P_o on Re_τ for the three different H_{phy} are plotted in figures 6.4. The small RMS fluctuations of all quantities are represented as error bars in the plot.

To the R_{tot} , σ_{eff} and P_o dependencies on Re_τ the corresponding form of (6.5) is plotted in the turbulent regime. The results in the varying scaling parameters θ are listed in the legends of the figures. Noticeable is the increase in effective conductivity and decrease in internal resistance with increased turbulence where, due to the definition of the effective conductivity, the $\theta_\sigma = -\theta_R$. That the θ_R and θ_σ tend towards zero for decreasing H can be explained by the conductivity curve being regarded as constants for high shear rate. As explained in the previous subsection, when the value of H is smaller and the corresponding $\dot{\gamma}_w$ is higher, the impact of increased Re_τ on conductivity becomes less significant.

Where the slight advantage of increased Re_τ cancels out, is for the power number P_o . Here the decrease in resistance and subsequent increase in P_e is drastically canceled out by the negative effect higher Re_τ have on the pumping power P_p . Specifically, the pumping power scaling in the turbulent regime can be derived from the definition of Re_τ (2.40), the definition of u^+ and z^+ from (2.45), and the relation of $\bar{u}^+(z^+)$ in the wall region (5.10). Taking $U_c = u_\tau \bar{u}^+(H^+)$ and the known $U_m \propto U_c$

relation [20], one derives for the pumping power the proportionality:

$$P_p \propto Re_\tau^3 \log(Re_\tau) \approx Re_\tau^3 \quad (6.10)$$

in the turbulent regime $Re_\tau \gtrsim 150$ [79].

By applying the scaling law and considering the value of θ_R obtained from the scaling analysis of R in Figure 6.4a, along with the definition of the power number in Equation (6.4), we can understand the behavior of θ_{Po} as shown in Figure 6.4c. This behaviour can be expressed in equation

$$Po = \frac{P_e}{P_p} \propto \frac{\frac{1}{R}}{\tau_w U_c} \propto \frac{Re_\tau^{-\theta_R}}{Re_\tau^3} = Re_\tau^{-\theta_R-3} \quad (6.11)$$

where the difference between θ_{Po} and $-\theta_R - 3$ is approximately 10%. Specifically, for channel heights $H_{phy} = 0.141/0.945$, we observe that $\theta_{Po} = -2.85/-2.67$, while $-\theta_R - 3 = -2.57/-2.36$, resulting in a difference of 10/12%.

Since $-\theta_R < 3$, the decrease in the overall power number for increasing turbulence is dominated by the increase in pumping power. This means that for a aqueous CB suspension in a SSFB the slight increase in conductivity increase due to turbulence is nullified by the drastic increase in pumping power to reach that turbulent state.

From the effect of channel half height H on power number P_o shown in figure 6.4d, no clear scaling law can be derived. Further research in more physical SSFB dimensions needs to be done, to pin down the expected scaling of the power number in this regard. However, the next section will dive deeper in the effects of channel height on σ_{eff} in the non-Newtonian regime.

6.3.4. Newtonian Conductivity and Resistance Results Summary

All in all, from the results presented here, the following important observations can be distilled.

- Given the range of channel heights chosen here, an increasing turbulent Re_τ results in a slight decrease in CB resistance, and an equal inverse increase in its effective conductivity and electric power number P_e .
- However, due to the large increase in pumping power needed to achieve the higher turbulent regimes, the power number P_o decreases.
- In the turbulent regimes, the non-dimensional numbers seem to fit a constant exponential for varying Re_τ and constant H , reasonably well. However, the θ_R and θ_σ scaling laws vary for H which is expected from a theoretical standpoint since Re_τ also dependent on H . The more physical explanation, for the conductivity advantage of higher Re_τ going to zero for smaller H , has to do with the conductivity becoming constant for $\dot{\gamma} \geq 634 [s^{-1}]$.

The effect of the shear-thinning rheology found in the CB suspension on conductivity and resistance will be considered next, after which all the results will be discussed in the final section of this chapter.

6.4. Turbulent Carbon Black Conductivity and Resistance considering the Non-Newtonian Rheology

To incorporate the shear thinning behaviour in the analysis of the effect of turbulence on the internal resistance and effective conductivity, the turbulent power-law simulations from the previous chapter will be used.

Specifically, the shear-rate profiles of the simulations with power index $n = 0.6$ will be converted to conductivity fields, due to their resemblance with the CB rheology found by Youssry *et al.* [86]. The conversion will be discussed shortly in Section 6.4.1, and the resulting conductivity fields are discussed in section 6.4.2. How the resulting CB resistance R and effective conductivity σ_{eff} compare to the Newtonian results will be discussed in section 6.4.3. Finally the difference between the laminar and turbulent CB resistance R and effective conductivity σ_{eff} will be discussed in section 6.4.4. How the results can be interpreted when considering SSFB designs will be discussed in the final section of this chapter.

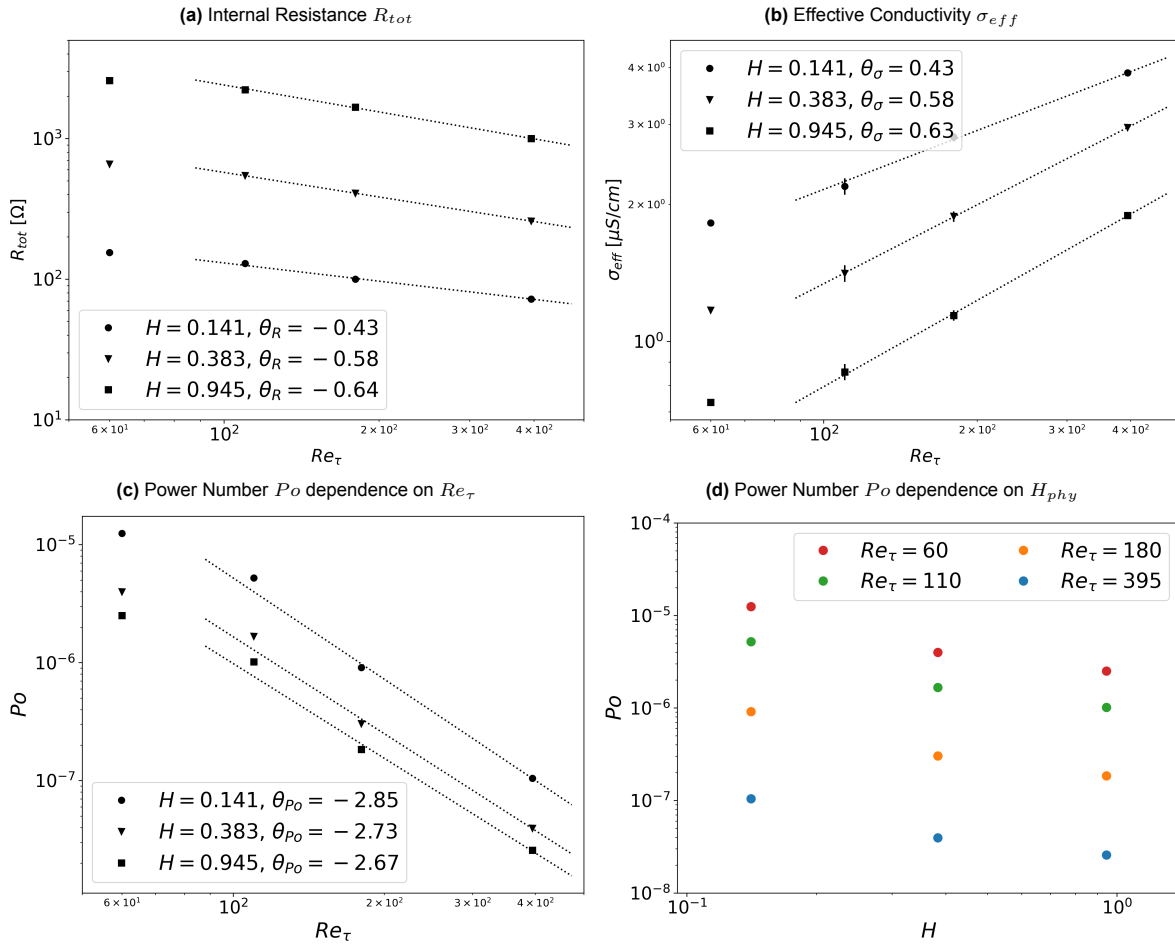


Figure 6.4: The non-dimensional scaling of the power number Po with the Newtonian approximation is represented in Figures 6.4c and 6.4d. Figures 6.4a and 6.4b display the scaling for the CB resistance R and effective conductivity σ_{eff} respectively. The different scaling parameters θ from equations (6.5), (6.6) and (6.7) are fitted to the turbulent data represented by $Re_\tau > 60$.

6.4.1. Non-Newtonian Conversion to Physical Units

The conversion steps to physical units are the same as for the Newtonian limit discussed in Section 6.3.1, with the only difference lying in the approximation of the viscosity (step 2). Where in Section 6.3.1 the viscosity was approximated to be constant for a given shear rate range, here the viscosity will be approximated using the power-law viscosity model. A power-law of $n = 0.6$ is found to show reasonable agreement with the CB viscosity in the range $\dot{\gamma} \approx 10 \rightarrow \dot{\gamma} \approx 200$ [s^{-1}] as can be seen in Figure 6.5. The effects of turbulence on the internal resistance and effective conductivity will therefore be conducted with a shear range that lies within this range. The specific range chosen goes from $\dot{\gamma}_{min}^{(60)} = 0.02 \rightarrow \dot{\gamma}_w^{(395)} = 1000$ (step 1) and results in a height of $H_{phy} = 0.286$ using equation (6.8). The physical parameters are summed up in table 6.3.

Table 6.3: Table represents the physical parameters for varying Re_τ^G that results from the choice of H_{phy} and power-law viscosity characteristics.

H_{phy} [m]	$\dot{\gamma}_{min}$	\rightarrow	$\dot{\gamma}_w$	Re_τ	$\overline{u^+}$	μ_w [$kg\ m^{-1}\ s^{-1}$]	\overline{U} [$m\ s^{-1}$]	P_p [kW]
0.286	0.02	\rightarrow	68	60	16.3	1.85	5.3	1.3
	0.5	\rightarrow	161	110	30	1.3	12.5	5.3
	12	\rightarrow	325	180	18.8	0.989	9.7	6.3
	20	\rightarrow	1000	395	19.5	0.63	14	18

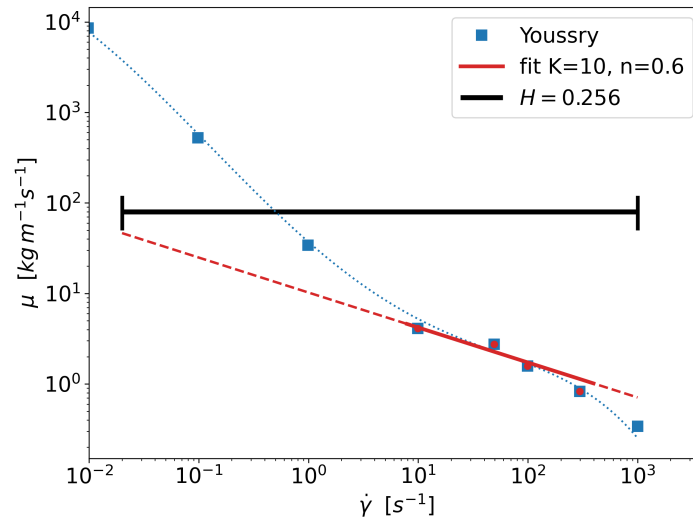


Figure 6.5: Figure shows the power-law fit through the Experimentally obtained rheological data by Youssry *et al.*[86]. For the data points ranging from $\dot{\gamma} \in [10, 300]$ the fit results in a consistency index of $K = 10 [kg m^{-1} s^{n-2}]$ and a power-law index of $n = 0.6$

6.4.2. Non-Newtonian Conductivity Results

The average and fluctuating conductivity inside the channel are shown in figure 6.6a. These results were obtained by converting the turbulent shear rate profiles of the $n = 0.6$ simulations to conductivity profiles using the physical parameters mentioned above, and the conversion method described in the previous section. When comparing the non-Newtonian characteristic conductivity to the conductivity curves found for the Newtonian simulations, one significant observation can be made. The difference between $\dot{\gamma}_w$ from varying Re_τ^G as found by equation (5.15) becomes smaller for $n = 0.6$ w.r.t. $n = 1$. The conductivity curves therefore lie closer to each other. Now the laminar $Re_\tau^G = 110$ simulation has a 12% higher average conductivity than its turbulent $Re_\tau^G = 180$ neighbor. The positive effect of turbulence on the CB conductivity is therefore diminished in the transitional region. The laminar simulation does have a pronounced dip in the middle of the channel. How this translates to the electrical resistance and effective conductivity will be discussed next.

6.4.3. Non-Newtonian Resistance and Effective Conductivity Results

Using the non-Newtonian conductivity fields and physical parameters discussed above as input for the FVM, the electric potential and with that the resistance and effective conductivity of the CB suspension is determined. These results are found in figure 6.6. Due to the laminar characteristics of the ($Re_\tau^G = 110$, $n = 1$) simulation, the number of points in the turbulent and laminar regime is restricted to pairs. The fits of the scaling laws to the laminar and turbulent regimes are therefore not meant for any definitive statements. The results do however tell an interesting story when comparing the laminar and turbulent scaling parameters as well as comparing the turbulent scaling to its Newtonian counterparts. In this regard the following statements can be made.

First, the turbulent non-Newtonian results are compared to the Newtonian results with equal $\dot{\gamma}_w^{(395)} = 1000$ constituting the channel half height $H = 0.383 [m]$. The following observations can be made:

- The resistance of the non-Newtonian turbulent simulations in Figure 6.6b are lower than the Newtonian simulations in Figure 6.4a, with a relative decrease ranging from 32% to 10% for increasing Re_τ^G . This decrease in resistance for the non-Newtonian flow can be explained by the decreased size of the channel due to the shear thinning rheology at equal $\dot{\gamma}_w$ and Re_τ . That the electrical resistance is lower for non-Newtonian flow therefore directly follows from equation (6.8).
- The $\theta_R^{\text{Turbulent}}$ scaling is less negative for the non-Newtonian simulation as compared to the Newtonian simulation. This can be explained by the mentioned decreased distance between the $\dot{\gamma}_w$ for varying Re_τ^G as found by equation (5.15). This results in the non-Newtonian $\dot{\gamma}_w$ for $Re_\tau^G < 395$ laying above their Newtonian counterparts, resulting in a higher overall conductivity and lower resistance for $Re_\tau^G < 395$. This in turn makes the scaling of $\theta_R^{\text{Turbulent}}$ less negative.

When comparing the laminar and turbulent scaling parameters the following observations can be made:

- It can be seen in Figure 6.6c that the turbulent σ_{eff} values are slightly higher than their laminar counterparts. However, the laminar σ_{eff} values grow faster with $\theta_{\sigma}^{Laminar} = 0.46$ than the turbulent ones characterised by $\theta_{\sigma}^{Turbulent} = 0.30$. Therefore there is a possibility that the laminar effective conductivity is higher at some point in the transition region. The inverse can obviously be said of the resistance scaling.
- That there are unknowns in the transition region can also be seen in the in the power number scaling in Figure 6.6d. Just as with the Newtonian simulations the power number clearly favours the laminar simulations due to the lower pumping power involved i.e. high P_o . The approximate exponential decay of the laminar P_o , however, is larger with $\theta_{P_o}^{Laminar} = -1.82$ than the turbulent scaling of $\theta_{P_o}^{Turbulent} = -1.04$. This leads to the P_o for $Re_{\tau}^G = 110$ and $Re_{\tau}^G = 180$ being almost equal, raising the question if the turbulent P_o will be higher then the laminar P_o , somewhere in the transition region.

Apart from the unknowns concerning the transition region, the above mentioned results also only concern one shear rate region with subsequent physical channel half height. To better understand the effect of turbulence on the conductivity of CB in the transition region, as well as for more shear rate regions, the next section will pit the laminar and turbulent conductivity field against each other in a more broad sense.

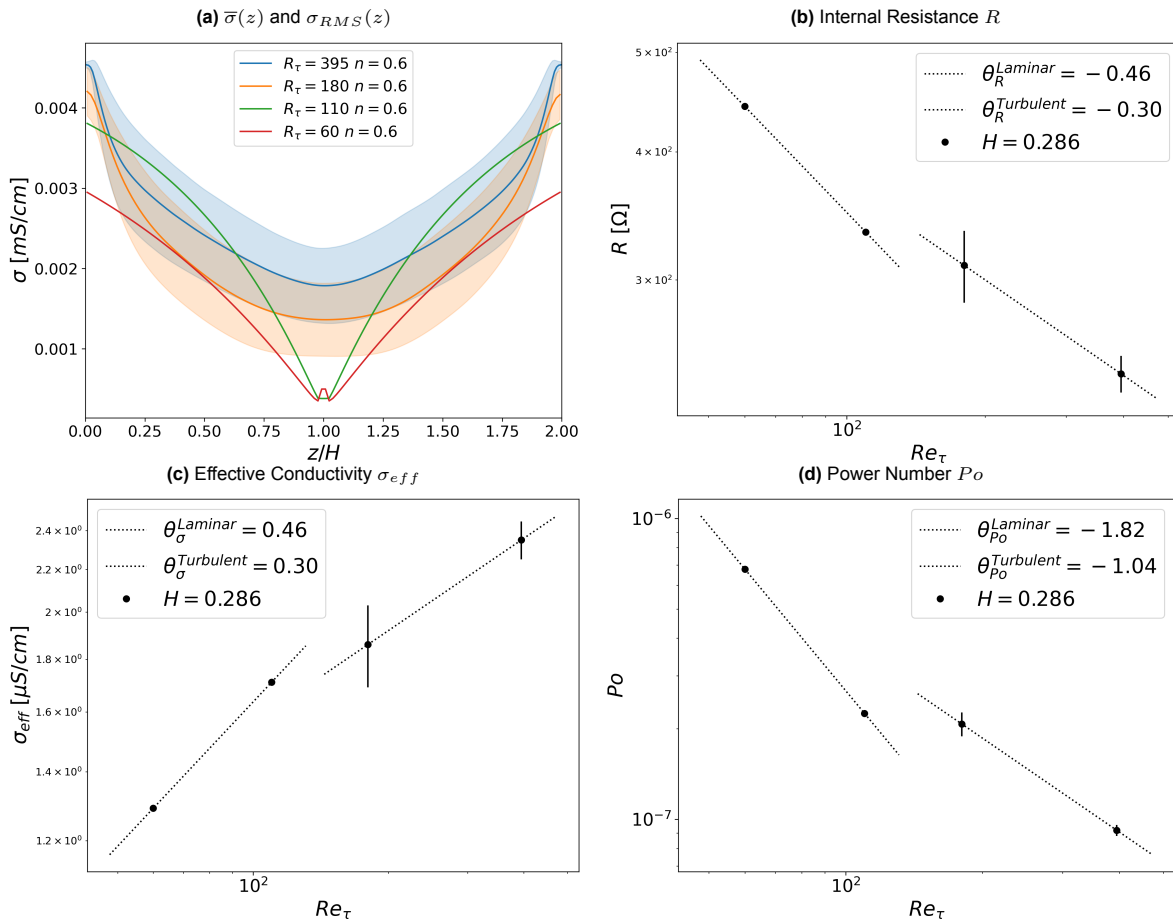


Figure 6.6: Figure 6.6a shows the mean and fluctuating conductivity curves $\bar{\sigma}$ for the shear thinning turbulent simulations ($n = 0.6$) given the channel height $H_{phy} = 0.286$. The rest of the figures represent the Re_{τ}^G dependence of the non-dimensional power number P_o , CB resistance R and effective conductivity σ_{eff} . The scaling parameters θ from equations (6.5), (6.6) and (6.7) are fitted to the turbulent and laminar data represented by $Re_{\tau} \in [60, 110]$ and $Re_{\tau} \in [180, 395]$ respectively.

6.4.4. Non-Newtonian Laminar vs Turbulence Resistance and Effective Conductivity Results

This section will further study the laminar and turbulent conductivity and effective conductivity characteristics in the transition region. The aim of this section is to answer the following two questions.

- How do the laminar and turbulent conductivity and effective conductivity compare when they occupy the same region in the conductivity curve, i.e., they have equal $\dot{\gamma}_w$?
- How does this difference change when different parts of the conductivity are considered, i.e., for different channel heights H_{phy} ?

The questions originate from a closer inspection of the shape of the laminar and turbulent shear rate profiles. The nondimensional average shear rate profiles of turbulent flows are lower, but do not show the dip in the middle of the channel compared to the corresponding laminar flow profiles (as can be seen in Figure 5.11a). Therefore, the question remains whether the characteristic shape of the turbulent flow profile is preferable compared to a laminar flow profile, when considering the total electric resistance of a CB suspension. This comparison is most relevant in the transition region where for equal pumping power and channel height, either a turbulent or laminar flow profile can be obtained.

A side-by-side study will be conducted to gain insights into the conductivity and resistance characteristics of shear-thinning laminar and turbulent flow profiles with viscosity exponent $n = 0.6$, represented by $Re_\tau^G = 110$ and $Re_\tau^G = 180$ respectively. This side by side comparison will represent the transition region for which the laminar flow profile will start exhibiting turbulent characteristics. To find out which flow profile in this transition region is favorable, different channel half heights H_{phy} will be considered. The chosen H_{phy} will result in varying shear rate ranges representing drastically different regions of the experimental conductivity curve found by Youssry [86].

To create a equal comparison with the same $\dot{\gamma}_w$ and H_{phy} , a single $Re_\tau^{G,Transition}$ is chosen to represent both the flow profiles. It is therefore assumed that there is such a $Re_\tau^{G,Transition}$ for which an infinitesimal increase in Re_τ^G results in the switch from the laminar flow profile to the flow profile represented by $Re_\tau^G = 180$. Due to the limitations of the current fluid dynamics model, the exact value for $Re_\tau^{G,Transition}$, given a power-law fluid with $n = 0.6$, could not be determined. Therefore, as an approximation $Re_\tau^{G,Transition} = 145$, exactly in between the laminar $Re_\tau = 110$ and transitional turbulent $Re_\tau = 180$ simulation.

Table 6.4: Physical units for Laminar vs Turbulence conversions

H_{phy} [m]	$\dot{\gamma}_w^{Transition}$ [s^{-1}]
0.131	1000
0.292	313
0.654	100
1.46	31.6
3.28	10

Using equation (6.8) and the transitional wall shear rate $\dot{\gamma}_w^{(110)} = \dot{\gamma}_w^{(180)} = \dot{\gamma}_w^{Transition}$, chosen to represent different regions on the conductivity curve, the varying H_{phy} are found. Using these physical parameters, represented in table 6.4, the conductivity curves and effective conductivities are calculated.

The average and root mean square fluctuating conductivity fields are shown in figure 6.7a for $H_{phy} = [0.131, 0.654, 3.28]$. It can be seen that on average the laminar simulation has a higher conductivity but shows a dip in the center line region, for $H > 3.28$ [m]. The range of relative increase in average conductivity between the laminar simulation and the turbulent simulation varies from 22% to 50%, with the disparity increasing as the value of H_{phy} increases or $\dot{\gamma}_w^{Transition}$ decreases.

The effect the turbulent and laminar flow fields have on the effective conductivity is shown in figure 6.7b. Here it can be seen that over the full range of H_{phy} and corresponding $\dot{\gamma}_w^{Transition}$ considered, the laminar effective conductivity outperforms its turbulent counterpart. Just like the average conductivity the difference in σ_{eff} diminishes for decreasing H_{phy} and subsequent increasing $\dot{\gamma}_w^{Transition}$. Specifically the relationship between σ_{eff} and H_{phy} is characterized by a negative power index ψ_H from equation (6.6) with $\psi_H^{Laminar} = -0.44 > \psi_H^{Turbulent} = -0.54$.

6.4.5. Non-Newtonian Conductivity and Resistance Results Summary

To sum up the non-Newtonian conductivity results, the following observations are considered.

- When considering the non-Newtonian rheology, a decrease in resistance is found, when compared to the Newtonian results. However, the rate at which the resistance decreases for increasing Re_τ^G seems less pronounced.
- There is clearly a different non-dimensional scaling involved, when for the laminar and turbulent regimes, i.e. different θ and ψ .
- When comparing the laminar and turbulent conductivity fields with the same $\dot{\gamma}_w^{\text{Transition}}$ over varying H_{phy} , the laminar effective conductivity is lower in all the cases considered.

How the above-mentioned observations can be interpreted and what they mean for SSFB design will be discussed in the next and final section of this chapter.

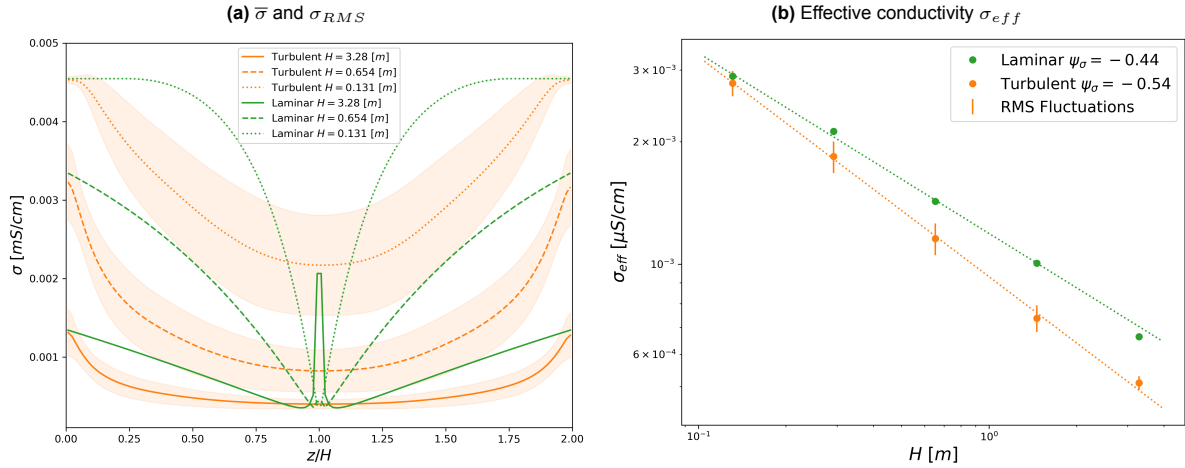


Figure 6.7: Figure 6.7a shows the average and RMS fluctuating conductivity field, obtained from the laminar ($Re_\tau^G = 110$, $n = 0.6$) and turbulent ($Re_\tau^G = 180$, $n = 0.6$) non-Newtonian simulations. The simulations are dimensionalised for the different channel heights found in table 6.4. For the conversion to physical units the Reynolds number is taken to be equal, resulting in equal $\dot{\gamma}_w$ for both the laminar and turbulent simulation. Figure 6.7b shows the effective conductivity for the same conversions, obtained from the FV potential calculation. There are clearly two different scaling laws ψ for the laminar and turbulent simulation, where the Laminar conductivity is higher throughout.

6.5. Discussion

In this section, the reliability and generality of the findings regarding the turbulent effects on CB resistance and conductivity are presented. Subsequently, this final section will be concluded by assessing the implications of the current findings on SSFB design.

6.5.1. Reliability and Generality of Results

There are some notes to be made on the reliability and generality of the results on the effect of turbulence on the conductivity and resistance of a CB suspension.

The first discussion point concerns the resolution of the laminar flow simulation. For the laminar simulation at ($Re_\tau^G = 60$, $n = 1$) and ($Re_\tau^G = 110$, $n = 0.6$), the actual $\dot{\gamma}_{min}$ should be zero in the middle of the channel. However, as stated in Section 5.5, due to the resolution of the simulation in the middle of the channel, the shear rates never really go to zero. This overestimation of the shear rate in the center of the channel results in an over- or under-representation of the local conductivity dependent on the height of $\dot{\gamma}_w$. However, due to the small region this concern and the larger influence of other assumptions, this effect will have a marginal effect on the final conclusions.

The next discussion points are related to the choice of the CB conductivity curve and how this choice affects the generalizability of the current results. There are two statements to be made to this end. First, within nonaqueous CB suspensions the shear rate conductivity curve changes with the concentration and type of CB used, as stated in section 2.1.3. The conductivity of all CB concentrations shown in figure 2.2 do, however, increase from a certain point onward. In these increasing regions, the same effect will be found as represented in the current results. Second, in addition to the differences within nonaqueous CB suspensions, there are also aqueous CB suspensions that show an order of magnitude higher conductivity at rest [48][85][57]. However, for these aqueous CB suspensions, there

are no conductivity shear rate relations found in the literature. If this data becomes available and the conductivity characteristics turn out to differ significantly with respect to the non-aqueous results used here, the current simulation setup could be used to determine the effect of turbulence on aqueous CB conductivity.

The last discussion point concerning the applicability of the current results has to do with the over-estimation of the electrical resistance. The determination of R_{tot} assumes that the electron travels the entire vertical length of the channel. Due to the CB conductivity σ being orders of magnitude lower than the ionic conductivity κ , reactions will predominately take place near the current collector [64]. Therefore, the path of the electron will be much shorter, reducing the electrical resistance. Because reactions will most likely take place near the wall, the conductivity at the wall becomes increasingly important. This is favorable for the laminar conductivity profile, which shows significantly higher conductivity near the wall. However, to quantify this exact effect, the full electrochemical performance, as described in section 2.1.4, needs to be modeled.

6.5.2. Effects of turbulence on SSFB Design

The main observations from the current research and the consequences for SSFB design will be discussed here.

Impact of Turbulent Flow on CB Suspension Conductivity in a SSFB: Key Observations

Three observations resulting from the presented research significantly impact our understanding of the influence of a turbulent flow field on the internal conductivity of a CB suspension within a SSFB. These two observations are:

- The extreme shear thinning rheology of a CB suspension acts as a damper on the development of turbulence in a channel, increasing the $Re_{\tau}^{G, \text{Transitional}}$ for which the transition from laminar to turbulence occurs. This means that significant pumping power and drastically increased fluid velocity or a larger channel height are needed to obtain turbulent flow. Not only the studied shear-thinning trend of the viscosity (represented by n) but also the absolute height of the currently CB viscosity (represented by K) acts as an amplification to this consequence.
- The characteristic shear rate shape of the turbulent flow with respect to laminar flow does not create an advantage in the characteristic conductivity field of the respective CB flow fields. Specifically, on average the turbulent shear rate is lower, where this decrease is most pronounced near the wall. Since the experimental conductivity curve increases for increasing shear rate [86] a higher local shear rate generates a higher local conductivity. This already results in an overall worse effective conductivity when considering the Ohmic losses over the full channel. When the reactions are taken to take place near the current collector, as expected, the Ohmic losses of the turbulent flow profile will be even worse as compared to its laminar counterpart.
- When a larger fixed height is chosen, pumping harder and consequently reaching a turbulent state, results in a better conductivity simply because the conductivity improves for increased shear rate. However, the next section will dive into the reasons why this larger channel height is unfavorable in SSFB design.

Therefore, two things can be concluded. First, given an SSFB design, pumping harder improves the effective conductivity, but when a turbulent state is reached, the rate at which the conductivity improves decreases. This is due to the unfavorable characteristic shear rate profile associated with turbulent flow. Second, it will not be likely for turbulence to occur in an SSFB due to fluid rheology, resulting in a damping effect on turbulence. This will be explained next.

The Impact of the Shear-Thinning Rheology on Turbulence Occurrence in a SSFB

That a SSFB design is unlikely to opt for the increase in pumping power or the increase in channel height needed for turbulence to occur, can be explained by the negative effect both decisions would have on battery efficiency. This has two main reasons:

- **Channel Height** Typically large electrode dimensions are not found in SSFB designs [48][22]. This is due to the discussed relatively low conductivity of CB restricting the reactions to the region

near the current collector. The channel being larger therefore results in the pumping of anolyte and catholyte fluids that will never react. This can have a negative impact on the overall efficiency of the battery.

- **Pumping Power** The electrical efficiency of the battery is reduced when pumping the catholytic fluids through the channel, as a greater portion of the available energy is consumed for pumping instead of being stored. Apart from this obvious negative effect, it also increases the average fluid velocity. Because of the limited current in common SSFB, this high fluid velocity results in a limited amount of pumped reactant gaining the chance to react before leaving the electrochemical stack. This can also have a negative impact on the efficiency of the battery.

The limitations mentioned above for an efficient SSFB design will make it unlikely that turbulence will occur in a flow battery with the channel dimensions used in this research. Given that turbulence also does not have a positive effect on the conductivity of the CB, this can be seen as a positive thing. However, pinpointing the exact pumping power or $Re_{\tau}^{G, \text{Transitional}}$ for which the transition to turbulence occurs and how this changes for different types of channels and rheologies is still interesting to study. Also the positive effects turbulence can have on the mass transfer of active particles are definitely interesting to study, as will be discussed in the recommendations.

7

Conclusion and Recommendation

Due to the intermittent electricity production of solar and wind power plants, the transition to renewable energy relies heavily on energy storage. As a safer, more scalable, and longer-lasting alternative to conventional battery packs, Flow Batteries are being built. To improve on this concept Semi-Solid electrolytes are being studied requiring a switch from Carbon Felt to a Carbon Black suspension as conducting media. The conductivity and rheology of such a Carbon Black suspension is found to be strongly dependent on shear rate. This leads to the question of what effect a turbulent flow profile has on the electrical resistance and pumping power of an SSFB. The goal of this thesis was to determine the effect of turbulence on the internal conductivity and total electrical resistance of a carbon black suspension inside a SSFB. To this end, a fluid dynamics model was developed as well as a model to describe the electric potential inside a variable conductor. This chapter will discuss the conclusions that follow from this work and will follow up with some recommendations for further work.

7.1. Conclusion

The Filter Matrix Lattice Boltzmann Method (FM-LBM) was implemented to run on a GPU to simulate non-Newtonian turbulent fluid flow within a reasonable time frame. The FM-LBM was chosen for its stability for low viscosity, which was benchmarked by simulating flows in the laminar non-Newtonian and Newtonian turbulent regimes. The discrepancies of the laminar simulations results, compared to analytical data, were well within the error margin, where the turbulent simulations showed small deviations in the first-order turbulent statistics compared to statistics reported in the literature [54][39]. These small deviations could, however, be explained due to an insufficient spatial resolution, and the marginal effect it had on further research was considered. The GPU implementation shows a three-fold improvement over recent CPU implementations, but the low efficiency compared to memory bandwidth leaves room for improvement [88][21].

Using the FM-LBM, non-Newtonian channel flow characteristics resembling CB suspension rheology were simulated in the transitional turbulence $Re_\tau = 110$, low turbulence $Re_\tau = 180$ and high turbulence $Re_\tau = 395$ regimes. The turbulent characteristics of the CB suspension were investigated by approximating the CB rheology using the power-law viscosity model. The investigation focused on the impact of decreasing the power index, denoted as n , which indicates an increase in shear-thinning viscosity characteristics associated with the CB rheology. These non-Newtonian turbulent channel flow results demonstrated a similar turbulence characteristics with decreasing n as found by comparable research done on pipe flows [70][30]. Compared to Newtonian turbulence, shear-thinning turbulent flows exhibited a damped turbulent effect increasing the general Reynolds number for which the flow transitioned from a turbulent to a laminar regime ($Re_\tau^{G,Transition}$). This increase in $Re_\tau^{G,Transition}$ was also the most important influence found on the characteristics of the shear rate required for the CB conductivity results.

To determine the effect of turbulence on the conductivity and electrical resistance of a CB suspension, the shear rate profiles were converted to conductivity profiles using the experimental data found by Youssry *et al.* [86]. The finite volume method was used to describe the potential field, generated by an applied voltage, inside the full SSFB channel, to determine the total CB resistance. The scaling

of this resistance as well as the effective conductivity with respect to Re_{τ}^G and the channel half height H_{phy} were studied.

For a large constant H_{phy} , an increase in Re_{τ}^G and subsequent dimensional shear rate presented improved conductivity profiles and subsequent CB resistance when considering the Newtonian limit. However, the increase in pumping power significantly outweighed the slight positive effect the higher Re_{τ}^G turbulence had on the conductivity. Both the decrease in resistance as the increase in pumping power became less pronounced when considering shear-thinning rheology. In the transition region from laminar to turbulence, the laminar conductivity profile even resulted in better conductivity characteristics for the wide range of channel heights considered.

Turbulence therefore has an overall negative effect on the pumping and Ohmic losses inside an SSFB when considering the electron resistance of the non-aqueous CB suspension studied in this research. Due to the relatively high viscosity of the CB suspension considered, and the damped turbulent effect due to its shear-thinning characteristics, turbulence is not something readily encountered in SSFB design. However, the exact $Re_{\tau}^{G,Transition}$ and pumping power scaling for varying CB suspensions needs to be established for different channel geometries to determine the SSFB designs for which turbulence modeling can be excluded.

7.2. Recommendations

The further recommendations for this research can be subdivided into three categories. First the further research in optimizing the electrochemical model is discussed. Then further research on the modeling of turbulent non-Newtonian flow characteristics is proposed. And finally some recommendations for further numerical method improvements are discussed.

Recommendations for further study's into the Electrochemical Performance of a SSFB

In order to gain a comprehensive understanding of the impact of turbulence on the electrochemical performance of a semi-solid flow battery (SSFB), it is necessary to develop a coupled electrochemical-transport model. As described in section 2.1.4, this model requires the simultaneous solving of the mass transfer, potential and momentum equations, and a model for the active surface area of CB in the electrolyte. With this electrochemical performance model the following effects of turbulence on the performance of a SSFB can be studied:

- **Ohmic Losses** The model will have to describe the location of the reactions making it possible to improve the description of the effects of turbulence on the Ohmic losses. Given the characteristic conductivity profiles of laminar and turbulent flows, and the fact that the reactions will most likely take place near the current collector, it is expected that turbulence will have an even more detrimental effect when reaction location is considered.
- **Mass Transport Limitations** With the proposed model, the depletion of active material near the current collector can be described. This will enable the study of the turbulent effects of mass transfer limitations in a SSFB. Given that turbulent flow generates mass convection in the direction of the current collector, turbulence is expected to improve the mass transport limitations of a SSFB.
- **Channel Geometry** The flow profile and subsequent electrochemical performance of a SSFB will depend greatly on the channel geometries. Studying the effect of turbulence on SSFB performance metrics considering different channel geometries and porous electrodes is therefore an interesting research direction.

Recommendations for further non-Newtonian turbulence research

In order to further improve the understanding of the turbulent characteristics of the CB suspension, the following research directions are proposed.

- **Time Dependant Rheology** To improve the characterisation of the CB suspension flow profile, further research is advised to incorporate rheological models that better represent the CB rheology. Specifically, given the strong shear history dependence of the CB rheology, incorporating this into the fluid model might drastically change the characteristics of the (turbulent) flow profile.

- **Transitional Turbulence** With this improved model research into an appropriate scaling for $Re_{\tau}^{\text{Transition}}$ and the pumping power needed for operation is advised. This will help determine for what SSFB designs turbulence can be excluded.

Recommendations for further FM-LBM GPU implementation optimisation

To improve the current numerical setup the following recommendations can be made.

- **Grid Refinement** Due to the higher resolution requirement near the wall, local grid refinement in this region will improve the overall results, while reducing the memory requirements. This will enable the increase in computational domain needed to determine $Re_{\tau}^{\text{Transition}}$.
- **Shared Memory** Using shared memory will drastically improve the computational efficiency and speed of the GPU implementation of the FM-LBM. This will shorten the simulation time and increase research output.

Miscellaneous

This master thesis represents the culmination of my two-year master's program in Applied Physics at the Technical University of Delft. I had the privilege of conducting this research within the group of Transport Phenomena in Nuclear Applications, located inside the TU Delft Reactor Institute (RID). I am grateful to Dr.Ir. Martin Rohde, the supervisor and group leader of this academic group, for providing me with guidance and support throughout this endeavor.

The unique nature of the group of Transport Phenomena in Nuclear Applications allowed me to explore and combine the academic fields of physical transport phenomena and energy physics. This perfectly aligned with my academic focus, as I have dedicated my studies to these two fields of physics. Consequently, this master thesis represents the final work for my chosen track, Physics of Energy.

I would again like to express my sincere gratitude to Dr.Ir. Martin Rohde for his exceptional supervision. His expertise, dedication, and continuous support have been instrumental in shaping the direction and quality of my research. Furthermore, I would like to extend my appreciation to Dr.Ir. Danny Lathouwers for his help with the implementation of the finite volume method. Additionally, I would like to thank Dr. Erik Kelder and Dr. Willem Haverkort for their guidance in the field of electrochemical modeling, and Dr. Matthias Moller for his support in parallel programming and GPU implementation. Their contributions have significantly enriched the depth and breadth of my thesis.

I would also like to acknowledge the previous work done by Willemijn Peters, which provided a solid foundation for my research. Her insights and efforts were invaluable in getting me up to speed and facilitating the progress of my work. Finally, I would like to give a shout-out to Mees Wortelboer, with whom I collaborated on parts of the numerical setup and talked over all the aspects of the roller coaster that is the master thesis end project.

For any inquiries or further discussion about my research, I can be reached at danielvanbemmen@outlook.com. I am more than happy to provide additional insights and support to those interested.

References

- [1] Delft High Performance Computing Centre (DHPC). *DelftBlue Supercomputer (Phase 1)*. <https://www.tudelft.nl/dhpc/ark:/44463/DelftBluePhase1>. 2022.
- [2] Piergiorgio Alotto et al. “Redox Flow Batteries for large scale energy storage”. In: *2012 IEEE International Energy Conference and Exhibition (ENERGYCON)*. IEEE. 2012, pp. 293–298.
- [3] G. Amati, S. Succi, and R. Piva. “Preliminary analysis of the scaling exponents in channel flow turbulence”. en. In: *Fluid Dynamics Research* 24.4 (Apr. 1999), pp. 201–209.
- [4] Allen J. Bard, Larry R. Faulkner, and Henry S. White. *Electrochemical Methods: Fundamentals and Applications*. Google-Books-ID: eZ6HDAEACAAJ. John Wiley & Sons, May 31, 2022. 1112 pp.
- [5] G. K. Batchelor. *An Introduction to Fluid Dynamics*. Cambridge Mathematical Library. Cambridge University Press, 2000.
- [6] Nathan Bell, Luke N. Olson, and Jacob Schroder. “PyAMG: Algebraic Multigrid Solvers in Python”. In: *Journal of Open Source Software* 7.72 (2022), p. 4142.
- [7] Jh Bertrand. “Sur l’homogénéité dans les formules de physique”. In: *Cahiers de recherche de l’Academie de Sciences* 86 (1878), pp. 916–920.
- [8] P. L. Bhatnagar, E. P. Gross, and M. Krook. “A Model for Collision Processes in Gases. I. Small Amplitude Processes in Charged and Neutral One-Component Systems”. In: *Physical Review* 94.3 (May 1954). Publisher: American Physical Society, pp. 511–525.
- [9] R. Byron Bird, Warren E. Stewart, and Edwin N. Lightfoot. *Transport Phenomena, Revised 2nd Edition*. English. 2nd edition. New York: John Wiley & Sons, Inc., Dec. 2006.
- [10] Gustavo Boroni, Nicolás Silin, and Alejandro Clause. “A Python implementation in graphic processing unit of a lattice Boltzmann model for unstable three-dimensional flows in immersed permeable media”. In: *Physics of Fluids* 32.12 (Dec. 2020). Publisher: American Institute of Physics, p. 127107.
- [11] E. Buckingham. “On Physically Similar Systems; Illustrations of the Use of Dimensional Equations”. In: *Physical Review* 4.4 (Oct. 1, 1914). Publisher: American Physical Society, pp. 345–376.
- [12] Ismail B Celik. *Introductory turbulence modeling*. 1999.
- [13] Rohit Chandra et al. *Parallel programming in OpenMP*. Morgan kaufmann, 2001.
- [14] Sydney Chapman and T. G. Cowling. *The Mathematical Theory of Non-uniform Gases: An Account of the Kinetic Theory of Viscosity, Thermal Conduction and Diffusion in Gases*. en. Google-Books-ID: Cbp5JP2OTrwC. Cambridge University Press, 1952.
- [15] Yongguang Cheng and Hui Zhang. “A viscosity counteracting approach in the lattice Boltzmann BGK model for low viscosity flow: Preliminary verification”. en. In: *Computers & Mathematics with Applications*. Mesoscopic Methods for Engineering and Science — Proceedings of ICMMES-09 61.12 (June 2011), pp. 3690–3702.
- [16] Rajendra P. Chhabra. *Rheology of Complex Fluids*. en. Ed. by J. Murali Krishnan, Abhijit P. Deshpande, and P. B. Sunil Kumar. New York, NY: Springer, 2010.
- [17] C. Chin et al. “The influence of pipe length on turbulence statistics computed from direct numerical simulation data”. In: *Physics of Fluids* 22.11 (Nov. 2010). Publisher: American Institute of Physics, p. 115107.
- [18] RM Clapp. “Turbulent heat transfer in pseudoplastic non-Newtonian fluids”. In: *International Development in Heat transfer. ASME, Part III, Sec. A., pg* (1961), pp. 652–661.

- [19] Shane Cook. *CUDA Programming: A Developer's Guide to Parallel Computing with GPUs*. 1st edition. Amsterdam ; Boston: Morgan Kaufmann, Nov. 27, 2012. 592 pp.
- [20] R. B. Dean. "Reynolds Number Dependence of Skin Friction and Other Bulk Flow Variables in Two-Dimensional Rectangular Duct Flow". In: *Journal of Fluids Engineering* 100.2 (June 1, 1978), pp. 215–223.
- [21] N. Delbosc et al. "Optimized implementation of the Lattice Boltzmann Method on a graphics processing unit towards real-time fluid simulation". In: *Computers & Mathematics with Applications*. Mesoscopic Methods for Engineering and Science (Proceedings of ICMES-2012, Taipei, Taiwan, 23–27 July 2012) 67.2 (Feb. 1, 2014), pp. 462–475.
- [22] Mihai Duduta et al. "Semi-Solid Lithium Rechargeable Flow Battery". In: *Advanced Energy Materials* 1.4 (2011). _eprint: <https://onlinelibrary.wiley.com/doi/pdf/10.1002/aenm.201100152>, pp. 511–516.
- [23] J. G. M. Eggels and J. A. Somers. "Numerical simulation of free convective flow using the lattice-Boltzmann scheme". en. In: *International Journal of Heat and Fluid Flow* 16.5 (Oct. 1995), pp. 357–364.
- [24] Victor Eijkhout. *Introduction to High Performance Scientific Computing*. [Raleigh, N.C.] : Lulu, 2015. 510 pp.
- [25] *Electricity consumption – Electricity Information: Overview – Analysis*. IEA. URL: <https://www.iea.org/reports/electricity-information-overview/electricity-consumption> (visited on 05/22/2023).
- [26] *Electricity production – Electricity Information: Overview – Analysis*. IEA. URL: <https://www.iea.org/reports/electricity-information-overview/electricity-production> (visited on 05/22/2023).
- [27] Robert Eymard, Thierry Gallouët, and Raphaële Herbin. "Finite volume methods". In: *Handbook of numerical analysis* 7 (2000), pp. 713–1018.
- [28] T.O.M. Forslund et al. "A dual-lattice hydrodynamic-thermal MRT-LBM model implemented on GPU for DNS calculations of turbulent thermal flows". In: *International Journal of Numerical Methods for Heat & Fluid Flow* 33.5 (Jan. 1, 2022). Publisher: Emerald Publishing Limited, pp. 1703–1725.
- [29] U. Frisch et al. "Lattice-gas hydrodynamics in two and three dimensions". In: *Complex Systems* 1 (1987), pp. 649–707.
- [30] A. A. Gavrilov and V. Ya. Rudyak. "Direct numerical simulation of the turbulent flows of power-law fluids in a circular pipe". en. In: *Thermophysics and Aeromechanics* 23.4 (July 2016), pp. 473–486.
- [31] Michael Godfrey. "First Draft Report on the EDVAC by John von Neumann". In: *IEEE Annals of the History of Computing* 15 (Jan. 1, 1993), pp. 27–43.
- [32] David J Griffiths. "INTRODUCTION TO ELECTRODYNAMICS Fourth Edition". In: (2021).
- [33] Sylvain Guillou and Rachid Makhloufi. "Effect of a shear-thickening rheological behaviour on the friction coefficient in a plane channel flow: A study by Direct Numerical Simulation". In: *Journal of Non-Newtonian Fluid Mechanics* 144.2 (July 20, 2007), pp. 73–86.
- [34] K. Hanjalic et al. *Analysis and modelling of physical transport phenomena*. Delft Academic Press, 2008.
- [35] Jacques Hardamard. "Sur les problèmes aux dérivées partielles et leur signification physique". In: *Princeton University Bulletin* 13 (Apr. 1902), pp. 49–52.
- [36] Dogukan T. Karahan, Devesh Ranjan, and Cyrus K. Aidun. "Turbulent channel flow of generalized Newtonian fluids at $Re=180$ ". In: *Journal of Non-Newtonian Fluid Mechanics* 314 (Apr. 1, 2023), p. 105015.
- [37] E Karimi-Sibaki et al. "Contribution of an electro-vortex flow to primary, secondary, and tertiary electric current distribution in an electrolyte". In: *Journal of The Electrochemical Society* 165.11 (2018), E604.

- [38] M. Amirul Islam Khan et al. "Real-time flow simulation of indoor environments using lattice Boltzmann method". en. In: *Building Simulation* 8.4 (Aug. 2015), pp. 405–414.
- [39] John Kim, Parviz Moin, and Robert Moser. "Turbulence statistics in fully developed channel flow at low Reynolds number". en. In: *Journal of Fluid Mechanics* 177 (Apr. 1987). Publisher: Cambridge University Press, pp. 133–166.
- [40] A. N. Kolmogorov. "Equations of turbulent motion in an incompressible fluid". In: *Proceedings of the USSR Academy of Sciences* (1941).
- [41] A. G. Kravchenko and P. Moin. "On the Effect of Numerical Errors in Large Eddy Simulations of Turbulent Flows". en. In: *Journal of Computational Physics* 131.2 (Mar. 1997), pp. 310–322.
- [42] Timm Kruger et al. *The Lattice Boltzmann Method Principles and Practice*. Springer, 2017.
- [43] Pijush K Kundu, Ira M Cohen, and David R Dowling. *Fluid mechanics*. Academic press, 2015.
- [44] Rémy Lacroix et al. "Modelling the rheology and electrochemical performance of Li₄Ti₅O₁₂ and LiNi_{1/3}Co_{1/3}Mn_{1/3}O₂ based suspensions for semi-solid flow batteries". In: *Electrochimica Acta* 304 (May 1, 2019). Publisher: Pergamon, pp. 146–157.
- [45] Siu Kwan Lam, Antoine Pitrou, and Stanley Seibert. "Numba: A LLVM-based Python JIT Compiler". In: (). ISBN: 9781450340052.
- [46] Bin Li and Jun Liu. "Progress and directions in low-cost redox-flow batteries for large-scale energy storage". In: *National Science Review* 4.1 (2017), pp. 91–105.
- [47] Zheng Li et al. "Aqueous semi-solid flow cell: demonstration and analysis". In: *Physical Chemistry Chemical Physics* 15.38 (2013), pp. 15833–15839.
- [48] Zheng Li et al. "Aqueous semi-solid flow cell: demonstration and analysis". In: *Physical Chemistry Chemical Physics* 15.38 (Sept. 11, 2013). Publisher: The Royal Society of Chemistry, pp. 15833–15839.
- [49] Kyle Lourenssen et al. "Vanadium redox flow batteries: A comprehensive review". In: *Journal of Energy Storage* 25 (2019), p. 100844.
- [50] Klaus Madlener, Benjamin Frey, and HK Ciezki. "Generalized reynolds number for non-newtonian fluids". In: *Progress in propulsion physics* 1 (2009), pp. 237–250.
- [51] Franz Mandl. *Statistical physics*. Vol. 14. John Wiley & Sons, 1991.
- [52] Message Passing Interface Forum. *MPI: A Message-Passing Interface Standard Version 4.0*. June 2021.
- [53] Mahdi Moghaddam et al. "Thermodynamics, Charge Transfer and Practical Considerations of Solid Boosters in Redox Flow Batteries". In: *Molecules* 26.8 (Apr. 7, 2021), p. 2111.
- [54] Robert D. Moser, John Kim, and Nagi N. Mansour. "Direct numerical simulation of turbulent channel flow up to $Re_{\tau}=590$ ". In: *Physics of Fluids* 11.4 (Apr. 1999). Publisher: American Institute of Physics, pp. 943–945.
- [55] COMSOL Multiphysics. "Introduction to COMSOL multiphysics®". In: *COMSOL Multiphysics, Burlington, MA, accessed Feb 9* (1998), p. 2018.
- [56] Aditya Narayanan, Frieder Mugele, and Michael H. G. Duits. "Mechanical History Dependence in Carbon Black Suspensions for Flow Batteries: A Rheo-Impedance Study". In: *Langmuir* 33.7 (Feb. 21, 2017). Publisher: American Chemical Society, pp. 1629–1638.
- [57] Thaneer Malai Narayanan et al. "Low-cost manganese dioxide semi-solid electrode for flow batteries". In: *Joule* 5.11 (Nov. 17, 2021), pp. 2934–2954.
- [58] John Newman and Nitash P Balsara. *Electrochemical systems*. John Wiley & Sons, 2021.
- [59] Frans T.M. Nieuwstadt, Bendiks J. Boersma, and Jerry Westerweel. *Turbulence: Introduction to Theory and Applications of Turbulent Flows*. Publication Title: Turbulence: Introduction to Theory and Applications of Turbulent Flows. Springer, July 2016.
- [60] *NVIDIA TESLA V100 GPU ARCHITECTURE*. Aug. 2017.

- [61] Christian Obrecht et al. "Multi-GPU implementation of the lattice Boltzmann method". In: *Computers & Mathematics with Applications*. Special Issue on Mesoscopic Methods in Engineering and Science (ICMMES-2010, Edmonton, Canada) 65.2 (Jan. 1, 2013), pp. 252–261.
- [62] Lena Oden. "Lessons learned from comparing C-CUDA and Python-Numba for GPU-Computing". In: (Mar. 1, 2020). Pages: 223.
- [63] H. Parant et al. "Flowing suspensions of carbon black with high electronic conductivity for flow applications: Comparison between carbons black and exhibition of specific aggregation of carbon particles". en. In: *Carbon* 119 (Aug. 2017), pp. 10–20.
- [64] W S J M Peters. "Modelling the Rheology and Internal Resistance of Alginate-based Semi-solid Flow Batteries". PhD thesis. Delft: Technical University Delft, May 2022.
- [65] Andreas Poullikkas. "A comparative overview of large-scale battery systems for electricity storage". In: *Renewable and Sustainable Energy Reviews* 27 (Nov. 1, 2013), pp. 778–788.
- [66] Christoph von Praun. "Race Conditions". In: *Encyclopedia of Parallel Computing*. Ed. by David Padua. Boston, MA: Springer US, 2011, pp. 1691–1697.
- [67] P. R. Rinaldi et al. "A Lattice-Boltzmann solver for 3D fluid simulation on GPU". In: *Simulation Modelling Practice and Theory* 25 (June 1, 2012), pp. 163–171.
- [68] Joeri Rogelj et al. "Mitigation pathways compatible with 1.5°C in the context of sustainable development". In: *Global Warming of 1.5°C. An IPCC Special Report on the impacts of global warming of 1.5°C above pre-industrial levels and related global greenhouse gas emission pathways, in the context of strengthening the global response to the threat of climate change, sustainable development, and efforts to eradicate poverty*. Ed. by V. Masson-Delmotte et al. IPCC/WMO, 2018, pp. 93–174.
- [69] M Rohde et al. "A generic, mass conservative local grid reynement technique for lattice-Boltzmann schemes". In: *International Journal for Numerical Methods in Fluids Int. J. Numer. Meth. Fluids* 51 (2006), pp. 439–468.
- [70] M. Rudman and H. M. Blackburn. "Direct numerical simulation of turbulent non-Newtonian flow using a spectral element method". en. In: *Applied Mathematical Modelling*. Selected papers from the Third International Conference on CFD in the Minerals and Process Industries 30.11 (Nov. 2006), pp. 1229–1248.
- [71] M. Rudman et al. "Turbulent pipe flow of shear-thinning fluids". en. In: *Journal of Non-Newtonian Fluid Mechanics* 118.1 (Mar. 2004), pp. 33–48.
- [72] Alexander Sinitsyn, Victor Vedenyapin, and Eugene Dulov. "Kinetic Boltzmann, Vlasov and related equations". In: (2011).
- [73] M Skyllas-Kazacos, C Menictas, and T Lim. "Redox flow batteries for medium-to large-scale energy storage". In: *Electricity Transmission, Distribution and Storage Systems*. Elsevier, 2013, pp. 398–441.
- [74] *Solar PV – Analysis*. IEA. URL: <https://www.iea.org/reports/solar-pv> (visited on 05/22/2023).
- [75] J. A. Somers. "Direct simulation of fluid flow with cellular automata and the lattice-Boltzmann equation". en. In: *Applied Scientific Research* 51.1 (June 1993), pp. 127–133.
- [76] Geoffrey Ingram Taylor. "Statistical theory of turbulenc". In: *Proceedings of the Royal Society of London. Series A - Mathematical and Physical Sciences* 151.873 (Jan. 1997). Publisher: Royal Society, pp. 421–444.
- [77] Tadeusz Tomczak and Roman Szafran. "Memory layout in GPU implementation of lattice Boltzmann method for sparse 3D geometries". In: *arXiv:1611.02445, sent to Computer Physics Communications* (Nov. 8, 2016).
- [78] H. C. H. Townend and Geoffrey Ingram Taylor. "Statistical measurements of turbulence in the flow of air through a pipe". In: *Proceedings of the Royal Society of London. Series A, Containing Papers of a Mathematical and Physical Character* 145.854 (Jan. 1997). Publisher: Royal Society, pp. 180–211.

- [79] Takahiro Tsukahara et al. "DNS of turbulent channel flow at very low Reynolds numbers". English. In: ISSN: 2642-0554. Begel House Inc., 2014.
- [80] S.H. Unger. "Hazards, critical races, and metastability". In: *IEEE Transactions on Computers* 44.6 (June 1995). Conference Name: IEEE Transactions on Computers, pp. 754–768.
- [81] Uzi Vishkin. "Thinking in Parallel: Some Basic Data-Parallel Algorithms and Techniques". In: (Mar. 2002).
- [82] G. Wellein et al. "On the single processor performance of simple lattice Boltzmann kernels". In: *Computers & Fluids*. Proceedings of the First International Conference for Mesoscopic Methods in Engineering and Science 35.8 (Sept. 1, 2006), pp. 910–919.
- [83] A.C. West. *Electrochemistry and Electrochemical Engineering: An Introduction*. Alan C. West, 2012.
- [84] Chae-Ho Yim et al. "On the Correlation between Free Volume, Phase Diagram and Ionic Conductivity of Aqueous and Non-Aqueous Lithium Battery Electrolyte Solutions over a Wide Concentration Range". In: *Journal of The Electrochemical Society* 164.6 (Mar. 15, 2017). Publisher: IOP Publishing, A1002.
- [85] Mohamed Youssry et al. "Aqueous dispersions of carbon black and its hybrid with carbon nanofibers". In: *RSC Advances* 8.56 (2018). Publisher: Royal Society of Chemistry, pp. 32119–32131.
- [86] Mohamed Youssry et al. "Non-aqueous carbon black suspensions for lithium-based redox flow batteries: rheology and simultaneous rheo-electrical behavior". en. In: *Physical Chemistry Chemical Physics* 15.34 (Aug. 2013). Publisher: The Royal Society of Chemistry, pp. 14476–14486.
- [87] E. Z. Zheng et al. "Direct numerical simulation of turbulent non-Newtonian flow using OpenFOAM". In: *Applied Mathematical Modelling* 72 (Aug. 1, 2019), pp. 50–67.
- [88] Congshan Zhuo and Chengwen Zhong. "LES-based filter-matrix lattice Boltzmann model for simulating fully developed turbulent channel flow". In: *International Journal of Computational Fluid Dynamics* 30.7-10 (Nov. 2016), pp. 543–553.
- [89] Congshan Zhuo, Chengwen Zhong, and Jun Cao. "Filter-matrix lattice Boltzmann model for incompressible thermal flows". In: *Physical Review E* 85.4 (Apr. 2012). Publisher: American Physical Society, p. 046703.